Entangled polarisation correlations of annihilation gamma and their applications to PET Imaging

Ruth Newton

Doctor of Philosophy

University of York

Department of Physics

June 1, 2022

Abstract

Our current understanding and measurements of photon quantum entanglement in the MeV scale are poor compared to the optical regime. However, recent advances in detector technologies and simulation frameworks are finally allowing for detailed studies at high energy scales.

In this thesis we assess the capabilities for two state-of-the-art gamma detector systems to characterise double Compton scattering of positron annihilation photons. The first system comprised two high resolution CZT crystals. The second was composed of two arrays of LYSO crystals with properties representative of current clinical PET scanners.

A new quantum entangled Geant4 version was developed and verified against data from these systems. The inclusion of quantum entanglement was shown to be crucial to describe correlations between the azimuthal planes of scattered annihilation photons. Standard (non-entangled) Geant4 failed to accurately describe photon transport and these new modifications have since become part of future Geant4 releases.

A first ever measurement of entanglement loss in the MeV regime is obtained, through study of the diminished Compton scatter correlations for data in which one photon has undergone Compton scattering prior to detection. Under these conditions the data are broadly consistent with a complete loss of entanglement between annihilation photons.

Finally, the entangled Geant4 was used to obtain the first simulated study of entangled PET imaging. A CZT based PET-scanner was simulated with a standard phantom. Using data from these simulated scans we present a technique to quantify and remove scatter and random backgrounds using only entanglement information in the PET events.

Contents

List of Figures

List of Tables

List of abbreviations

DCS	Double Compton scatter
PET	Positron emission tomography
TOF	time of flight
ICS	Inter-crystal scatter
CZT	Cadmium zinc telluride
LOR	line of response
LYSO	Lutetium-yttrium oxyorthosilicate
PMT	Photomultiplier tube
SiPM	Silicon photomultiplier

Acknowledgements

Firstly I would like to thank my supervisor Dan Watts for such an excellent project and for his limitless optimism, patience and enthusiasm throughout.

I must also thank Jamie Brown and Julien Bordes for their fantastic support and guidance over the last few years. You always made time for a zoom, no matter how daft the questions.

My thanks to John Allison whose expertise in Geant4 made this project go so smoothly and to Alex Cherlin for sharing some of his extensive knowledge of CZT.

I would like to thank the entire nuclear physics group at York for making it such an enjoyable 3 years. In particular to Gustavo and Pierre for helping me retain my sanity over lockdown. Your support, encouragement, tea and zooms really kept me going.

Thank you to all the Red Goat climbing crews over the years, it's been an absolute blast.

To Tim and Beth for your sarcasm, mockery and relentless support. To Mei for being my rock, and to Linus, for feeding me.

UK Research and Innovation

Author's declaration

I declare that this thesis is a presentation of original work and that I am the sole author. This work has not previously been presented for an award at this university or at any other. All sources are acknowledged as references.

The present work led to the publication of one original article:

- Watts, D.P., Bordes, J., Brown, J.R., Cherlin, A., Newton, R., Allison, J., Bashkanov, M., Efthimiou, N. & Zachariou, N.A. Photon quantum entanglement in the MeV regime and its application in PET imaging. Nat Commun **12**, 2646 (2021).

Chapter 1

Introduction

The annihilation of a positron and an electron predominantly creates two photons with identical energies travelling in near back-to-back directions. These characteristics enabled the application of positrons to medical imaging, leading to the advent of positron emission tomography (PET) in the early 1970s [JT17]. This imaging modality utilises the fact that the two annihilation photons travel along a straight line to localise the position of a positron emitting source inside a patient. In contrast to most medical imaging modalities this allows for functional imaging, providing information on factors such as tissue function, changes to blood flow and metabolism [Lam01]. As detector technology evolves producing higher sensitivities, greater energy resolution, finer position resolutions and cheaper crystals the applicability and utility of PET is increasing.

One characteristic of these photons which has yet to be utilised in medical imaging is that they are predicted to be predominantly formed in an entangled polarisation state. The purpose of this thesis is to determine whether currently available detector technologies are capable of detecting this entanglement and explore how quantum information can be extracted from PET data and utilised to improve image quality. The possibility for detailed tests of the predicted entanglement is also realisable.

To understand how photon entanglement of gamma quanta can be investigated and then utilised in PET imaging we must first consider the physical interactions by which these photons are produced and through which they interact. In this first chapter we discuss the methods by which gamma photons interact with matter, how annihilation gamma are produced, and how the entanglement between the two gammas can effect their subsequent behaviour.

1.1 Photon Interactions in Matter

Photons can interact with matter by one of four main mechanisms. These are:

- Photoelectric Effect
- Compton Scattering
- Pair Production
- Rayleigh Scattering

The total photon attenuation is the sum of all four contributions. The dominance of each process varies with photon energy, and the atomic number of the material, as shown in Fig. 1.1.

The **photoelectric effect** occurs when an incoming photon transfers its total energy to a bound electron within the nucleus. This electron is then emitted with an energy dependent on the initial photon energy and the binding energy of the participant electron in the atom.

Photons of higher energies can **Compton scatter**. This is a process by which the photon interacts with an electron (predominantly) in the outer shell of the atom. The two scatter elastically and are both emitted from the atom. If the electron is considered unbound and stationary the energy of the photon after scattering, E'_γ, is given by,

$$E'_\gamma = E_\gamma \frac{1}{1 + \frac{E_\gamma}{m_e c^2}(1 - cos\theta)} \tag{1.1}$$

with, E_γ, the initial photon energy, m_e, the electron mass, c, the speed of light and, θ, the scattering angle.

Pair production is only possible for photons of energies greater than or equal to $2m_e c^2$, the mass of two electrons at rest. In this process the photon interacts with the electric field from the charged nucleus producing an electron positron pair. Fortunately for annihilation gamma, as utilised in PET imaging, the photon energies (511 keV) are well below this threshold meaning pair production is not present in PET systems.

Rayleigh scattering (otherwise known as Coherent scattering) is the scattering of light off particles significantly smaller than the wavelength of the incident light. In this instance the gamma interacts with the electrons in the atom, but does not excite or ionise the atom. Typically, very little energy is transferred to the atom and the scattering angle is very small. The strength of this process is most significant for gamma energies $\leq$50 keV and as such its role in the context of PET imaging is dominantly in the lower energy processes near to the end of the photon track as it stops in a detector.

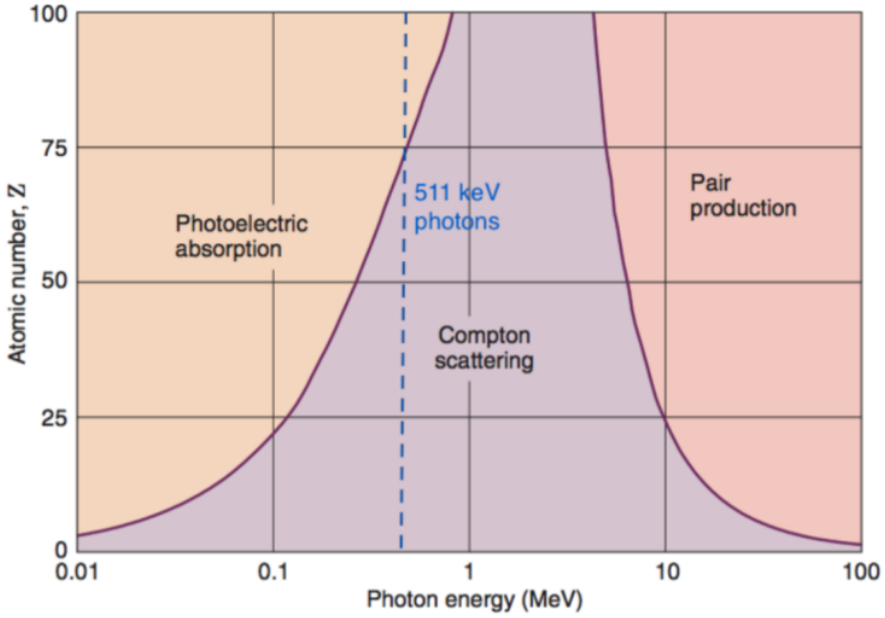

Figure 1.1: The dominance of each interaction process as a function of photon energy and atomic number. Figure reproduced from [CSP12].

1.2 Positron emitting sources

The photons utilised in PET imaging are produced from the annihilation of a positron and an electron. The positron is produced through beta plus decay of a radioactive nucleus. This occurs when a proton inside the radioactive nucleus is converted into a neutron, thus releasing a positron and an electron neutrino.

$$ {}^{X}_{Y}\mathrm{A} \rightarrow {}^{X}_{Y-1}\mathrm{B} + \mathrm{e}^{+} + \nu_e \tag{1.2} $$

A proton is composed of 2 up quarks and one down, and a neutron of 1 up quark and 2 downs. This interaction is mediated by the weak force, with one quark changing flavour from up to down.

The resulting positron rapidly thermalises with its surroundings through collisions with bound electrons in the medium. The probability that this positron annihilates "in-flight" (prior to thermalising) is low, of the order 2% in tissue [Har04]. Once thermalised the positron may either directly annihilate with an electron of opposing spin, resulting in 2 gamma annihilation, or the positron and electron form the metastable state, positronium. Positronium (Ps) is a unique bound state of a positron and an electron which can exist in two spin configurations. These are the singlet state para-positronium, in which the spin of the positron and electron are

antiparallel (total S=0), or the triplet state ortho-positronium, when the two spins are parallel (S=1). Para-positronium decays predominantly into two gamma, each of which have an energy of 511 keV, with a lifetime in vacuum of 125 ps [Rie20]. Theoretically it can decay into any even number of gamma but the branching ratio decreases rapidly with more gamma. In vacuum ortho-positronium annihilates predominantly into 3 gammas with energies $\leq$ 511 keV, with a total energy of 1022 keV. It has a ground state lifetime in vacuum of 142 ns, however the observed lifetime in liquids is significantly shorter than this due to the "pick-off" process, by which a second electron with anti-parallel spin reacts with the positron in ortho-positronium and the two annihilate to produce two gamma [Gar53]. It has been proposed that the lifetime shortening of ortho-positronium is dependent on the physical and chemical environments (in particular the presence of oxygen [KHC90; KS05]).

Few measurements of positronium decay have been performed in tissue, however the probabilities of these mechanisms in water have been predicted to be [Mos19; Jas17; Har04]:

- ~60% of positrons annihilate directly with the electron to form two gamma.
- ~10% first form para-positronium which rapidly decays into two gammas.
- ~30% first form ortho-positronium, before annihilating into two gammas via the "pick-off" process.
- ~0.5% form ortho-positronium which self-decays into three gamma.

Despite the proclivity to form ortho-positronium rather than para-positronium, the effect of "pick-off" interactions means that almost all annihilations in tissue still result in just two gamma.

1.3 Polarisation and Entanglement in Compton Scattering

In this section the concepts of photon polarisation and entanglement relevant to the current study of PET photons is outlined, including how the measurement of polarisation is made using the reaction processes of the photons in the detector.

Photons are quanta of electromagnetic radiation, comprised of coupled oscillations of perpendicular magnetic and electric fields. The polarisation of the photon refers to the orientation of its electric field and is described by the polarisation vector. Photons are linearly polarised

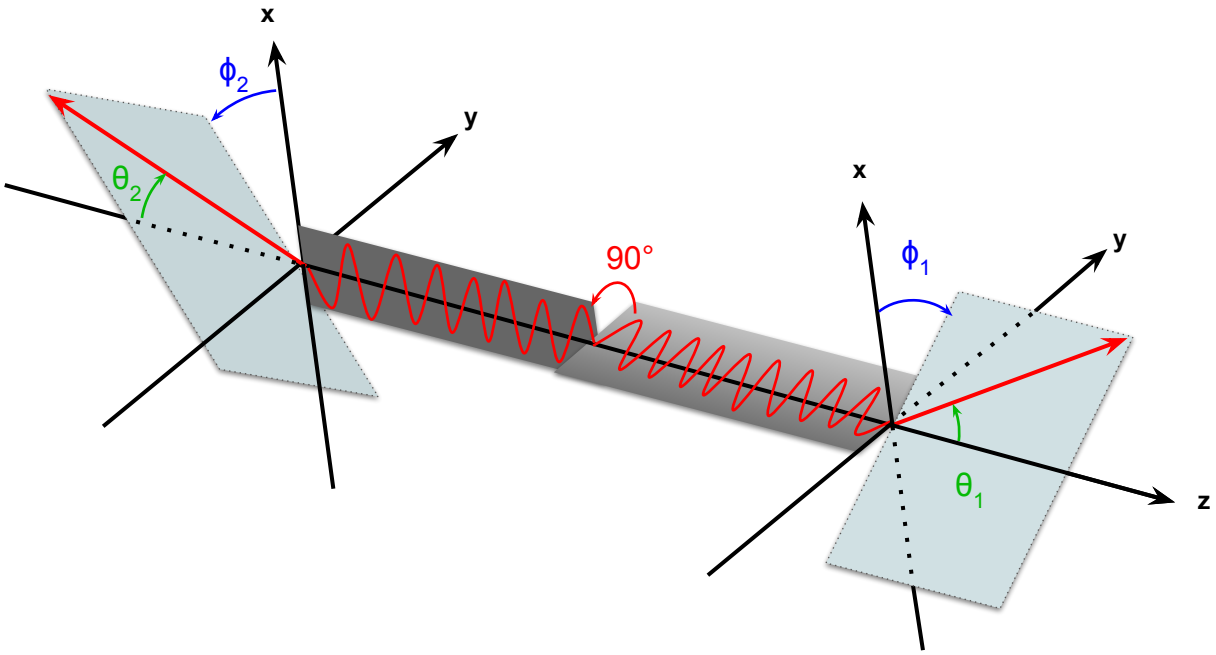

Figure 1.2: A schematic of the Compton scattering coordinate system [Wat21]. Two annihilation photons travel back-to-back with perpendicular polarisation. Each photon Compton scatters through a polar angle θ, and azimuthal angle ϕ. The red arrows represent the scattered trajectory of each photon.

when the polarisation vectors are preferentially oriented relative to a defined axis. They are unpolarised when the polarisation vectors point in random orientations.

Polarisation effects for keV photons become readily observable through Compton scattering, an effect dependent on photon polarisation. The differential cross section describes scattering probability over a solid angle. For Compton scattered, unpolarised photons it is given by the Klein-Nishina formula as follows [KN29]:

$$\frac{\mathrm{d}\sigma}{\mathrm{d}\Omega} = \frac{r_e^2}{2}\frac{E_i^2}{E_f^2}\left(\frac{E_f}{E_i} + \frac{E_i}{E_f} - \sin^2(\theta)\right). \tag{1.3}$$

Here E_i and E_f represent the photons energy before and after scattering. r_e is the classical radius of electrons and θ the scattering angle as defined in Fig.1.2.

The annihilation process occurs preferentially for positrons at rest and therefore has zero net angular momentum. As a result the two annihilation photons must have perpendicular linear polarisation in order to conserve momentum.

In 1954 [Hei54] extended the Klein-Nishina formula to describe polarised photons. The

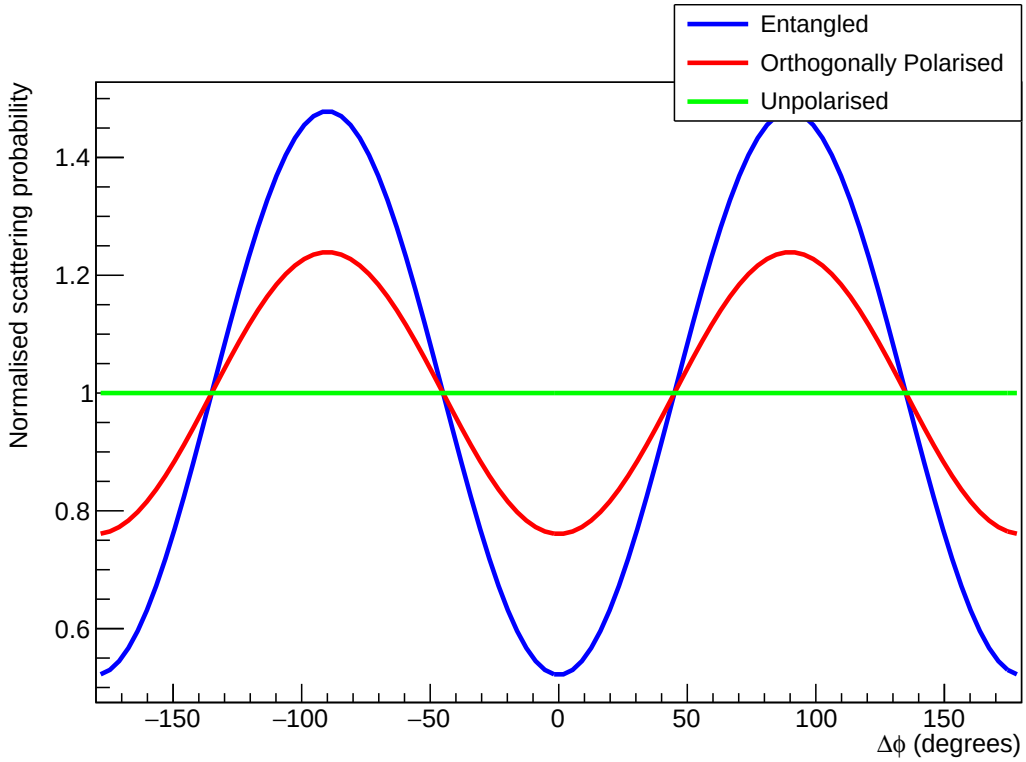

Figure 1.3: Theoretical double Compton scattering distribution as a function of $\Delta\phi$ for $\theta_1 = \theta_2 = 81.7°$. Plotted for entangled (blue), polarised (red) and unpolarised (green) photons.

cross-section now becomes dependent on the azimuthal scattering angle, ϕ and is given as follows,

$$\frac{\mathrm{d}\sigma}{\mathrm{d}\Omega} = \frac{r_e^2}{2}\frac{E_i^2}{E_f^2}\Big(\frac{E_f}{E_i} + \frac{E_i}{E_f} - 2\cos^2(\phi)\sin^2(\theta)\Big). \tag{1.4}$$

All variables have the same definition as equation 1.3, with the addition of the azimuthal scatter angle ϕ, defined in Fig. 1.2.

The scattering probability for polarised photons therefore has a strong dependence on ϕ. With all other terms taken as constants it will follow a $\cos^2\phi$ distribution, peaking at scattering angles of $\phi = \pm 90°$. In the case of two annihilation photons created with a 90° separation in polarisation ($\Delta\phi = 90°$), their scattering distribution as a function of $\Delta\phi$ then takes the form

$$P(\Delta\phi) = 1 - \cos^2(\Delta\phi) \tag{1.5}$$

retaining the $\cos^2\phi$ dependence [Bog03].

When a positron and electron of opposing spin annihilate to form two gamma, conservation of parity forces the annihilation gamma to be in a single entangled wavefunction (or Bell state),

expressed as

$$\frac{1}{\sqrt{2}}(|x\rangle_- |y\rangle_+ - |y\rangle_- |x\rangle_+), \tag{1.6}$$

where $|x\rangle_-$ and $|y\rangle_-$ represent a gamma travelling in the -z direction with polarisation in x and y respectively. $|x\rangle_+$ and $|y\rangle_+$ are equivalently defined in the +z direction [UW49]. This entangled Bell state is the only allowed state following the annihilation of ground state positronium into two photons. Substituting respective wavefunctions for each of the ket vectors yields an equation for the Compton scattering cross section of entangled annihilation photons [PW47]:

$$\frac{d^2\sigma}{d\Omega_1 d\Omega_2} = \frac{r_0^4}{16}(K_a(\theta_1,\theta_2) - K_b(\theta_1,\theta_2)\cdot\cos(2\Delta\phi)) \tag{1.7}$$

where K_a and K_b are kinematic factors defined as follows

$$K_a = \frac{[(1-\cos\theta_1)^3+2]\cdot[(1-\cos\theta_2)^3+2]}{(2-\cos\theta_1)^3\cdot(2-\cos\theta_2)^3}, \tag{1.8}$$

$$K_b = \frac{\sin^2\theta_1\cdot\sin^2\theta_2}{(2-\cos\theta_1)^2\cdot(2-\cos\theta_2)^2)}. \tag{1.9}$$

and $d\Omega_{1,2}$ and $\theta_{1,2}$ are the solid angles and polar scattering angles for each of the two gamma.

This formalism was first presented by Pryce and Ward in 1947 [PW47] and independently derived by Snyder et al. a year later [SPH48]. It is described in Wards PhD thesis how equivalent theoretical results can be obtained when using either time-dependent perturbation theory or a Klein-Nishina approach [UW49]. Since then the same form has been derived using both matrix formalism [Car19] and by employing Kraus Operators [HM19; Wat21].

The effect of this entanglement consideration is to enhance the amplitude of the $\cos(2\Delta\phi)$ dependency. A comparison of the resulting cross sections (for $\theta_1 = \theta_2 = 81.7°$) are shown in Fig. 1.3. To quantify this effect we can define the enhancement, R, as the ratio of photons that scatter at the peak of this distribution, with an azimuthal difference ($\Delta\phi$) of 90°, to those at the trough, with an azimuthal difference of 0°.

$$R(\theta) = \frac{P_\perp(\theta)}{P_\parallel(\theta)} \tag{1.10}$$

In Table 1A of Bohm and Aharonovs publication [BA57] they calculate the perpendicular and parallel scattering probabilities of entangled gamma pairs scattering at $\theta = \theta_1 = \theta_2$. These probabilities are given as follows,

$$P_{\parallel}(\theta) = 2\gamma(\gamma - 2\sin^2\theta) \quad \text{and} \quad P_{\perp}(\theta) = (\gamma - 2\sin^2\theta)^2 + \gamma^2, \tag{1.11}$$

where $\gamma = (k_0/k) + (k/k_0)$ with k_0 and k representing the wave numbers of the incident and scattered gamma respectively. The resulting enhancement factor, obtained from dividing these two functions, is plotted in Fig.1.4 as a function of θ. A maximum enhancement factor of 2.85 is found at $\theta = 81.7°$ (predicted by [PW47; SPH48; Car19]). Similarly in Table 1B of [BA57] probabilities are given for the case of perpendicularly polarised independent gamma,

$$P_{\parallel}(\theta) = (2\gamma^2 - 4\gamma\sin^2\theta + \sin^4\theta) \quad \text{and} \quad P_{\perp}(\theta) = (2\gamma^2 - 4\gamma\sin^2\theta + 3\sin^4\theta), \tag{1.12}$$

with γ defined as above. The predicted enhancement factors for this hypothetical non-entangled case are plotted in red in Fig. 1.4. The distribution is shown to peak similarly at $\theta = 81.7°$ with a maximum enhancement of R=1.63, representing the upper limit for independent (non-entangled) gamma.

1.4 Witnessing entanglement through polarisation correlations

As introduced in the previous section, the double Compton scattering cross section of entangled annihilation photons is modulated by a $\cos(2\Delta\phi)$ dependency. This distribution has a maximum amplitude at $\theta_1 = \theta_2 = 81.7°$ at which the number of photons scattering perpendicular to each other, compared to the number scattering parallel is equal to 2.85, otherwise known as the enhancement ratio, R,

$$R = \frac{P_{\perp}}{P_{\parallel}} = 2.85. \tag{1.13}$$

Classically the maximum achievable enhancement ratio is 1.63 [BA57], consequently any measurement in which a value above 1.63 is obtained constitutes a measurement of entanglement within the system. The first ever measurements of this ratio from an entangled annihilation source were performed in 1948 by Hanna [Han48] and Bleuler [BB48]. These produced values 10-28% lower and 12% higher, respectively, than predicted theoretically. In 1950 the experiment was reproduced by Wu and Shaknov [WS50]. Their experiment consisted of a positron emitting source, with fixed scatterers on either side. Two anthracine crystal scintillator detectors were then placed at fixed azimuthal angles to detect coincidences of the scattered photons. The detectors were positioned such that the mean scattering angle detected was close to 81.7°.

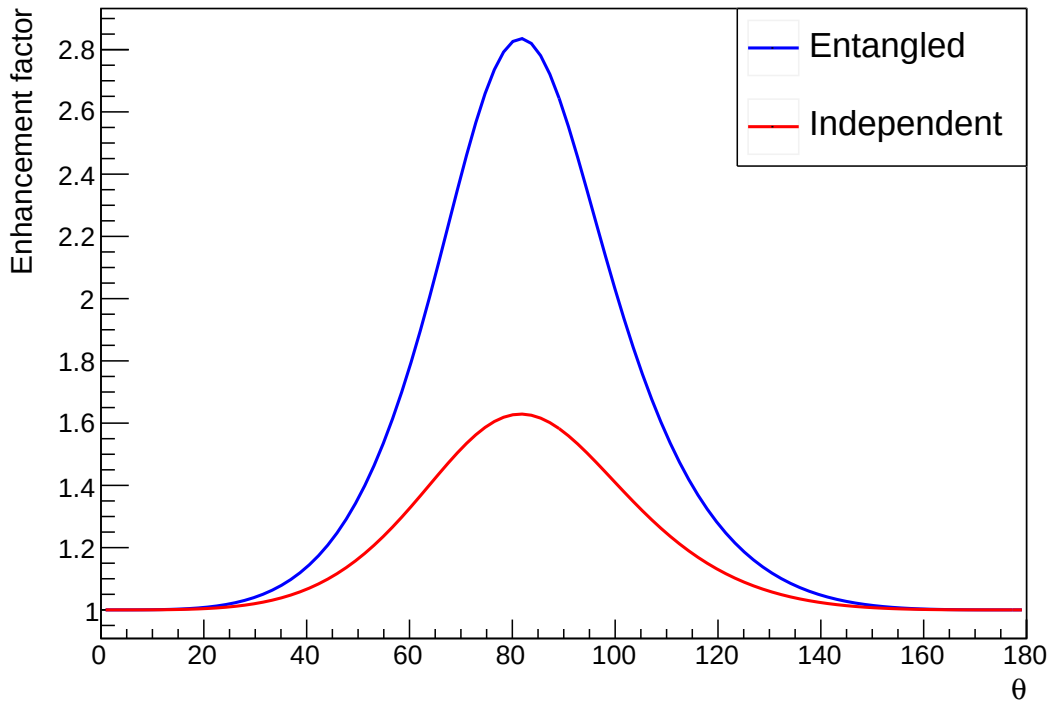

Figure 1.4: The theoretical enhancement factors (R) predicted by Bohm and Aharanov [BA57] for the double Compton scattering of annihilation γ. The enhancement is shown for the case of symmetric double Compton scattering, in which both annihilation γ scatter through the same polar angle ($\theta_1 = \theta_2 = \theta$). The dependence on θ is shown for entangled γ by the red line, and for perpendicularly polarised but independent γ by the blue. Both distributions are found to peak at $\theta = 81.7°$

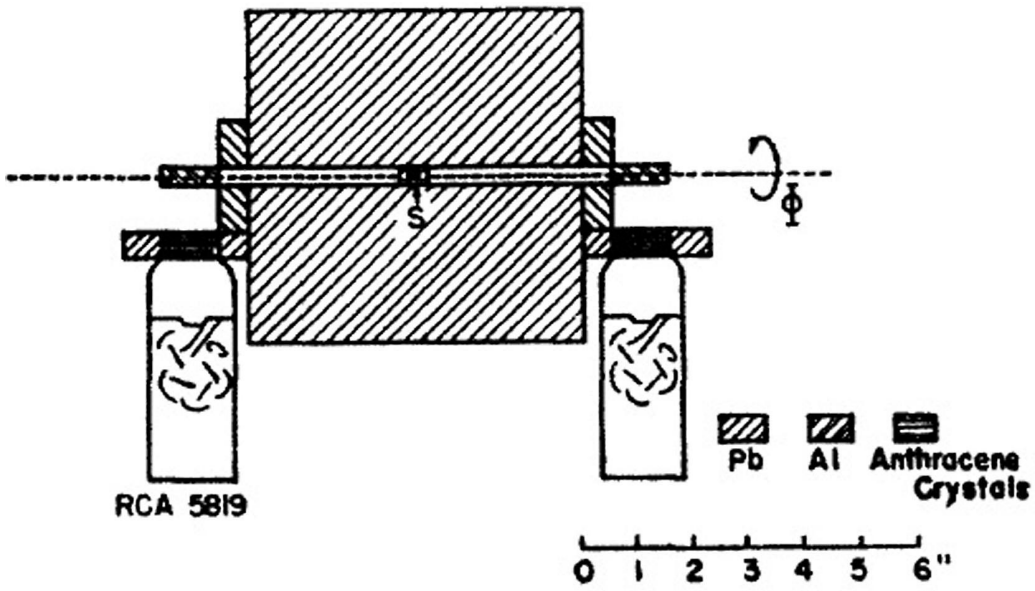

Figure 1.5: A schematic of the experimental setup of Wu and Shaknov, image replicated from [WS50].

One detector was left fixed while the other was rotated through four azimuthal angles, 0, 90, 180 and 270°. A schematic of their experimental setup is shown in Fig .1.5. They measured an enhancement ratio of

$$\frac{P_{\perp}}{P_{\parallel}} = 2.04 \pm 0.08. \tag{1.14}$$

which was in agreement with Pryce and Wards theory when integrated over the θ range covered by the detectors.

These early experiments assumed any contribution from 3 γ annihilation would be negligible, due to the very low yield (just 0.5%) and the application of energy windows. It was also assumed that annihilation from the decay of ortho-positronium through the singlet pick-off process would produce annihilation photons in an entangled state. Since then measurements have been performed of positron annihilation from a range of different materials [BDM77; BDS81; WLB76], all of which produced results consistent with Eq. 1.7, providing verification of this assumption [Wat21]. The work presented in this thesis will employ the same assumptions.

Bohm and Aharonov [BA57] were first to identify that these polarisation correlations represent an example of the entanglement discussed in the famous Einstein, Rosen and Podolsky paradox [EPR35]. This led to experiments such as these becoming popular in the realm of fundamental physics. More recently entanglement measurements have focused more on the optical regime due to the availability of more efficient linear polarisation analysers [CS78]. However, in recent years the introduction of detectors with higher spatial sensitivity has reignited interest in

these experiments at the MeV scale and their applications [Wat21]. Crucial to future progress is the development of simulation tools capable of modelling the effects of entanglement. A suitable framework for this has been developed as part of the current project and is discussed in the next section.

1.5 Implementing Quantum Entanglement into Geant4

The use of Monte-Carlo methods in medical physics has rapidly increased in recent years. The ability to accurately model the interaction and transport of particles within both the patient and detector has opened up a wide range of new possibilities. Monte-Carlo techniques have been employed in the design of new detectors [Jan11], to aid treatment planning by performing dose calculations [Pap12; And18] and in developing radiation protection and shielding.

A prime example of one such toolkit is the Geant4 package which is used to trace the path of particles through their interactions with matter [Ago03]. It has applications in high energy physics, astrophysics, medical physics and radiation protection [All16]. The software is highly adaptable - geometries, materials and physical processes can all be individually designed and modified depending on the simulation requirements. In the initial stages of this PhD project a group at the University of York incorporated the entangled description of the interactions of positron annihilation photons into Geant4. New routines were developed that enabled communication between the individual particle tracking processes which allowed the reproduction of the scattering cross section for entangled γ pairs. The modifications were implemented into Geant4 version 10.5, and this new version will throughout this thesis be referred to as QE-Geant4. These modifications to the simulation framework will also be included in future releases of Geant4.

The standard Geant4 physics routines for modelling Compton scattering of polarised gamma use the polarised Klein-Nishina theory (Eq. 1.4) and are embedded within the "Livermore" physics package. However as discussed previously in this chapter, this description is insufficient to fully model the behaviour of annihilation photons. In the modified QE-Geant4 this modelling is assumed for all photon scattering processes, other than the first two interactions of an annihilation γ pair.

When an annihilation occurs the two annihilation gammas (γ_1, γ_2) are processed sequentially: when γ_1 undergoes its first Compton scatter the kinematics of the interaction are stored and made accessible to other particles in the event. γ_1 is then tracked using the standard Geant4 processes until it is destroyed. For the second gamma, γ_2, the modelling for its first Compton scatter is selected according to the distribution of Eq. 1.7 using the previously stored

kinematics from γ_1. From then on any subsequent Compton scatter interactions (for either γ) revert back to the standard Geant4 models. This is equivalent to the assumption that the first double Compton scattering process completely collapses the entangled state, with all subsequent interactions modelled as independent and separable photons. The validity of this assumption shall be discussed in more detail in Chapter 4. A diagram of this implementation is shown in Fig. 1.6.

To compare this modified simulation against theoretical predictions we first simulated a "perfect" detector, i.e. one having an effectively infinite detecting medium compared to the path length of the photons. This simulation comprised an e^+ source placed at the centre of a 10 x 10 x 10 m^3 cube of cadmium zinc telluride (a semiconductor detector discussed at length in Chapter 4). A given e^+ annihilated with an electron, and the trajectories of the resulting γ were tracked. In the instance when both the annihilation γ underwent one Compton scatter event, the difference in azimuthal scattering angle, $\Delta\phi$, was extracted from the exact momentum vectors. The obtained $\Delta\phi$ distribution is shown by the blue data points in Fig. 1.7. This shows excellent agreement with the theoretical prediction (based on Eq. 1.7) shown by the smooth blue curve, giving confidence in its implementation within Geant4. For comparison the results using standard Geant4 annihilation classes are shown by the red data points in Fig. 1.7 along with the analytic prediction for double Compton scattering of non-entangled states presented by Bohm and Aharonov [BA57].

The results highlight how current Geant4 and all previous PET simulations do not account for the predicted entanglement of the PET photons. Regardless of whether the entanglement information is utilised, as presented in this thesis, the photon transport in previous PET simulations following Compton scatter processes will be inaccurate. The new QE-Geant4 simulation will form the basis of future studies in PET.

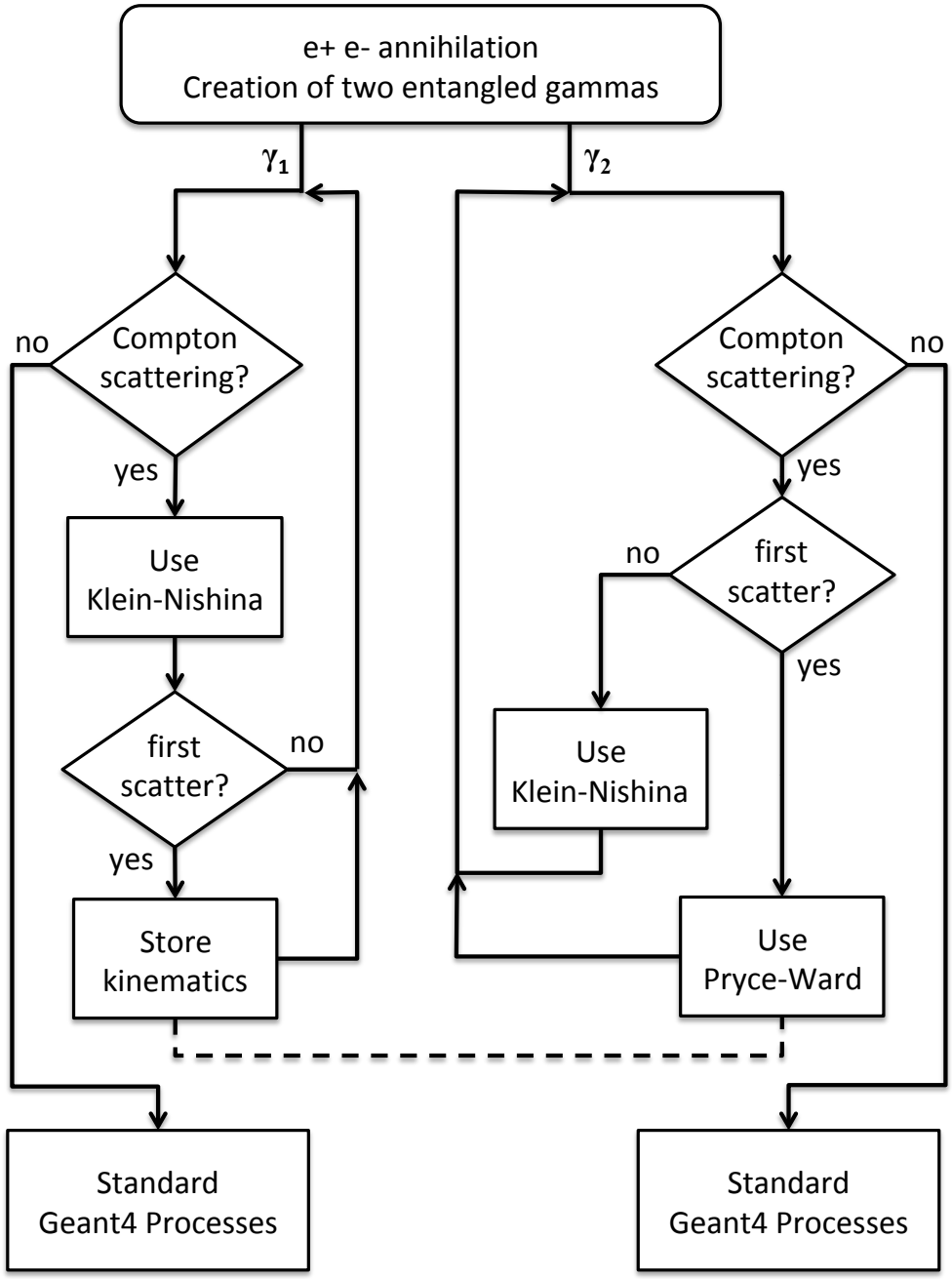

Figure 1.6: A flowchart describing the implementation of entanglement in the QE-Geant4 simulation. Each γ is processed sequentially. Firstly γ_1 is tracked, if it undergoes a Compton scatter the kinematics of the scatter are stored and then used to calculate the first Compton scatter of γ_2. This is performed in the "Use Pryce-Ward" action, which employs Eq. 1.7 using the stored kinematics from γ_1. If γ_1 does not Compton scatter then the kinematics for γ_2 are calculated using standard polarised Klein-Nishina.

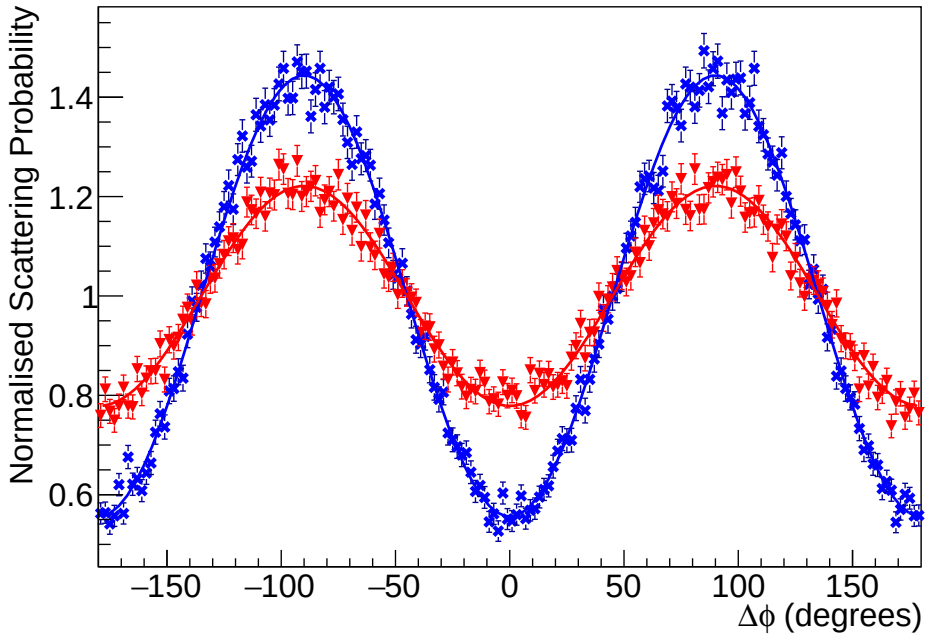

Figure 1.7: Data points and curves show the normalised scattering probability as a function of the relative scattering angle, $\Delta\phi$. The theoretical predictions from Eq.1.11 and Eq.1.12 are shown in blue for entangled and red for non-entangled orthogonally polarised photons. The data points represent simulation results from QE-Geant4 (blue) and standard Geant4 (red). All results have been integrated over a range of polar scattering angles $67° \leq \theta \leq 97°$.

Chapter 2

The Gamma Detector Systems

Radiation detector systems rely on incoming radiation transferring energy to the detector medium and causing either excitation or ionisation processes. Excitation occurs when the interaction of the incoming radiation leaves the atom in an excited state. Ionisation occurs when the energy deposited is sufficient to remove an orbital electron from the atom/molecule.

PET imaging involves the fast detection of 511 keV gamma. The main requirements of a good PET detector are as follows:

- High spatial resolution
- High energy resolution
- Fast timing
- Cost Effectiveness
- High detection efficiency

The relative importance of each of these properties shall be discussed further in Chapter 3. To improve on these quantities and utilise the latest technological developments, new detector types are now under consideration for PET. Many of these new detector designs originated in high energy physics and nuclear experiments, and are now being incorporated into PET prototypes. For inorganic scintillation crystals there has been much recent work to improve the scintillation light yield using new materials, enabling improvements in timing and energy resolution. Examples include the development of LuAP for its fast response time of 17 ns [Kun05]. Solid state semiconductor detectors enable much higher multiplicity in charged particle production for a given energy deposit due to the small band gap between the conduction and valence bands (e.g. for Germanium detectors this is around 0.66 eV). This allows vast improvements in

energy resolution over standard scintillators. However the expense of germanium detectors has meant their application in PET is very limited. New technologies such as CZT (section 4.2) allow similar performance at a fraction of the cost, therefore these technologies have started to be implemented in commercially successful medical imaging products.

In the following sections the various detector types will be discussed in more detail.

2.1 Scintillator Detectors

Scintillator detectors were first developed in the 1900's yet still remain the most common detector type for PET today. They rely on the excitation and subsequent de-excitation of electrons in the scintillator crystal which releases multiple scintillation photons of lower energy visible light. The scintillator is coupled to a photomultiplier tube (PMT) or silicon photomultiplier (SiPM) which absorbs these photons and converts them into a detectable electric current. Scintillator detectors can be split into two categories, organic and inorganic scintillators.

2.1.1 Inorganic scintillators

Inorganic scintillators scintillate due to the discrete energy bands imposed by their crystalline structure. As such, an individual atom or molecule of the substance will not scintillate. In such a crystal electrons can occupy the lower valence band, in which they are tied to a lattice site, or the higher conduction band in which they have sufficient energy to move freely through the crystal. Between these two bands exists the forbidden band, where electrons in a pure crystal cannot be found [Web02]. An energy deposit can excite these valence electrons up into the conduction band, at which point they decay back into the valence band releasing a scintillation photon in the process. However for pure crystals this decay is very inefficient, releasing few photons of large energies. Most crystals are modified by inserting "impurity" atoms of other elements. These create sites in the lattice with a modified band gap structure, creating excited energy states within the forbidden band. Since the energy gap from the conduction band to the impurity states is now smaller the emitted photons have lower energy and a longer wavelength, giving rise to visible or UV photons. Specifically, when an incoming high energy gamma interacts within the crystal via the photoelectric effect, it imparts energy to a photoelectron. This photoelectron then moves through the crystal creating electron hole pairs. Due to their lower ionisation energy, the holes will quickly be drawn to impurity sites and ionise them, exciting an electron into the conduction band. The excited electrons then travel through the crystal until they find an ionised impurity site, at which point they will de-excite, releasing

scintillation photons of a visible wavelength. Some commonly used inorganic scintillators are NaI(TI), BGO, LSO(Ce). In each case the element in brackets represents the "impurity" element.

2.1.2 Organic scintillators

Unlike inorganic scintillators, organic scintillators scintillate as an inherent property of the molecule itself, and as such it is independent of the molecule's physical state (solid, liquid or gaseous form). Scintillation results from transitions of valence electrons into higher molecular orbits. The ground state, S_0, is a singlet state, above which lies the excited state, S_1. Each of these electron energy levels has a fine structure associated with it corresponding to molecular vibrational modes. The energy spacing between these modes is ∼0.15 eV compared to the spacing between electron levels ∼3-4 eV [Leo94]. Incoming particles excite ground state electrons, which then rapidly decay to the first excited state, through processes such as internal conversion. The transition between this first excited state and a higher vibrational mode of the ground state releases a scintillation photon. Since this energy is slightly less than the gap between the excited and ground state the organic scintillator can be transparent to its own florescence.

2.1.3 Photomultiplier Tubes (PMTs)

The most widely used devices for detection of these scintillation photons are electronic light detectors called photomultiplier tubes (PMTs). Once stimulated by low energy scintillaton photons PMTs produce an electric current.

The entrance window of a photomultiplier tube is coated with a photo-emissive substance that ejects electrons when visible light is incident upon it. This surface is referred to as the photocathode, and the efficiency of conversion between the incoming visible photons and the emitted photoelectrons is referred to as the quantum efficiency. Common quantum efficiencies are around 20-30%, although there is a strong dependence on the wavelength of the incoming light and as such PMTs must be well matched with the wavelength range of the scintillator emission spectrum. For a typical incident scintillation flux of a few thousand photons, only a few 100 photoelectrons are produced, as such the current is too small to serve as a useful electrical signal. A focusing grid directs these photoelectrons towards a series of metal plates called dynodes. Each dynode is set at a positive voltage relative to the photocathode causing the photoelectrons to accelerate towards it, gaining energy. The dynodes are coated in a material with high secondary emission characteristics (negative electron affinity materials), so

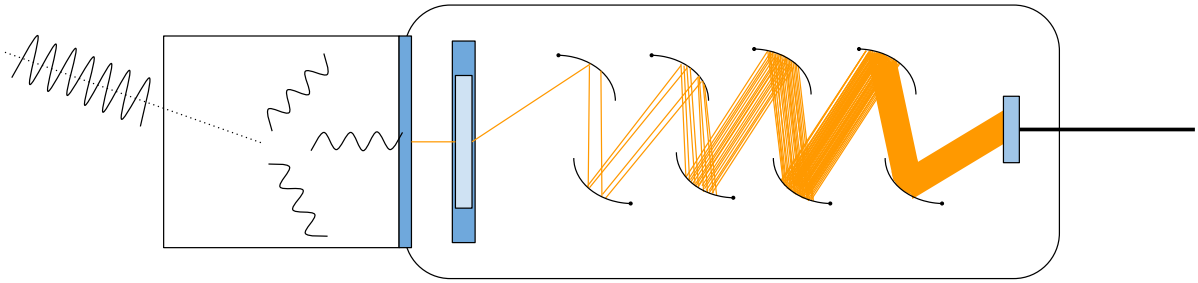

Figure 2.1: Schematic of a photomultiplier tube (PMT).

that when high energy photoelectrons strike the surface multiple secondary electrons are ejected. The secondary electrons are then attracted to another dynode maintained at a higher voltage and the multiplication process is repeated until the electron shower is eventually detected at the anode. PMTs typically contain 9-12 dynodes with multiplication factors between x3-6 at each dynode, resulting in an overall multiplication of the order 10^7 [CSP12]. As such, even low energy scintillation photons can produce a large current. The original PET machines all relied upon PMTs to convert scintillation photons to electronic signals. However the development of integrated PET and magnetic resonance systems (see Chapter 3) led to the development of new techniques, most noticeably avalanche photo-detectors (APDs) and silicon photomultipliers (SiPMs). Unlike photomultiplier tubes, both of these devices are not susceptible to the magnetic fields produced during an MR scan, allowing the two modalities to be performed in unison.

2.1.4 Silicon Photomultiplier (SiPM)

Silicon photomultipliers are light sensitive semiconductor detectors, composed of arrays of hundreds to thousands of single-photon avalanche diodes (SPADs). Incoming scintillation photons create electron hole pairs which are then separated by an applied field, inducing a current. When the voltage applied is low this current is proportional to the intensity of the incoming light, representing a gain of just $\times 1$ (compared to $\times 10^7$ for a PMT). If the applied voltage is increased the device behaves as an avalanche photodiode. Each electron produced gains sufficient kinetic energy that its collisions in the medium cause further ionisation, resulting in more electron hole pairs. In this case gains of $10^2 - 10^3$ are seen [GH20]. If the applied voltage is increased even more (above the breakdown voltage) holes also gain sufficient kinetic energy to create secondary electron hole pairs, referred to as Geiger-mode [Ren06]. A large avalanche of

charge carriers is initiated resulting in a high gain $\sim 10^7$. These avalanches can be triggered from just one ionisation, allowing for the use of SiPMs in single photon counting detectors. The speed at which this avalanche is produced also gives rise to an excellent timing resolution. SiPMs are advantageous over PMTs for multiple reasons. They can deliver a similar gain with a much lower voltage. They can be manufactured very small in area and are robust devices. They typically have slightly higher quantum efficiencies than PMTs (60-80%) [CSP12].

2.1.5 Common scintillator materials for PET imaging

A good scintillator detector must have a high detection efficiency (be capable of detecting as many incoming photons as possible), with a well defined position and energy resolution. Consequently, good scintillator crystals require the following properties [Kno10]:

- **A high stopping power**. This defines how far a photon will travel through the material before its energy has been entirely absorbed. The higher the stopping power the more likely a given photon interacts with the crystal and is subsequently detected. It is dependent on the density of the material and its effective atomic number (Z_{eff}) [Sah10]. As such, inorganic crystals formed from heavy atoms are typically employed (e.g NaI, LYSO).

- **High photon yield**. An incident photon should create a large number of scintillation photons, the more scintillation photons reaching the PMT/ SiPM per energy deposit the higher the energy resolution of the detector.

- **Low self-absorption of scintillator photons**. This maximises the number of photons reaching the PMT.

- **Short decay time**. This is the time between excitation and subsequent decay and is specific for each material, usually of the order of a few ns. The shorter the decay time the higher the timing resolution of the detector.

- **Refractive index close to that of glass**. This improves coupling with the PMT.

Table 2.1 shows these properties for some commonly used scintillators in medical physics. A final consideration, of particular importance in this thesis, is the probability of Compton scatter. In an ideal detector all photons would immediately interact via the photoelectric effect. This way the entire energy is deposited in one crystal and it is easy to identify a single event. However, in practice in most scintillator crystals the probability of a 511keV photon interacting via the

photoelectric effect on the first interaction is less than 50% (e.g. NaI(Tl) is 18%, BGO is 43% and LSO is 34%) [Lew08]. The scattering of gamma between pixels reduces the overall achievable position resolution of the detector.

Table 2.1: Properties of common scintillator materials used in medical physics [CSP12].

Property	NaI(Tl)	BGO	LSO	GSO	CsI(Tl)	$LaBr_3$(Ce)	LYSO	Plastic
Density (g/cm3)	3.67	7.13	7.40	6.71	4.51	5.3	7.10	1.03
Effective Atomic Number	50	73	66	59	54	46	63	12
Index of refraction	1.85	2.15	1.82	1.85	1.80	1.9	1.81	1.58
Decay Time (ns)	230	300	40	60	1000	35	20	2
Peak emission wavelength (nm)	415	480	420	430	540	358	438	Various
Photon yield (per keV)	38	8	20-30	12-15	52	61	32	10

Early PET machines utilised thallium-doped sodium iodide [NaI(Tl)] due to its high light output. However this was quickly replaced as the material of choice by bismuth germanate (BGO), a scintillator crystal with a high density and large effective atomic number leading to a significantly higher stopping power. Its light output however is relatively low resulting in a poor energy resolution. It also has a slow decay time, 300ns, which limits its use in applications with high count rates. This led to the introduction of LSO (lutetium oxyorthosilicate) and LYSO (lutetium yttrium oxyorthosilicate). These have fast decay times, ∼40 ns, and better energy resolution, ∼8% FWHM at 662 keV [WCP12]. The higher light output (∼30 photons/keV) means more crystals can be attached per photo-multiplier tube resulting in bigger arrays of smaller crystals. Overall this leads to a better position resolution [Mel]. The main drawback however is the cost of growing these crystals, which is significantly more than that of BGO. It should also be noted that naturally occurring Lutetium contains about 2.6% ^{176}Lu, which is itself radioactive. This increases the background noise, and can become a serious issue in low count-rate applications. LYSO and LSO are the two most widely used materials for new PET detectors to date.

There have been recent explorations in the use of plastic scintillator detectors [Kap14]. These have a good timing resolution and the key advantage of being very cheap to construct, which could potentially allow PET scanners to become much more widely available [Ruc18]. Their disadvantages are a significantly lower stopping power, lower photoelectric cross-section and lower photon yield. However many of these issues can be compensated for by its affordability, much larger detectors could be built, increasing the field of view and as such compensating for the loss in sensitivity.

The fundamental limitation of all scintillator detectors is their energy resolution. The energy

required to produce one optical photon is relatively large, of the order of 100 eV. Consequently for every incident photon only a few thousand optical photons are produced. This means there is large statistical fluctuation. This motivated a move towards semiconductor detectors, which require significantly less energy to release each "information carrier", 1-2 eV [Kno10].

2.2 Semiconductor detectors

In a crystalline material the periodic lattice defines allowed energy bands in which the electrons can exist. Electrons can occupy the lower energy valence band, in which they are tied to a specific lattice site, or be excited into the upper level conduction band where they have sufficient energy to migrate through the crystal. These two energy bands are separated by the band gap, a region in which no electron energy states exist. The size of this band gap determines whether the material is an insulator, a conductor or a semiconductor.

In a conductor either the conduction band is partially filled, or the valence band and conduction band overlap. This allows electrons to move easily between the valence and conduction bands with just a small input of energy. In an insulator the band gap is very large ∼5 eV, so even with a large energy input valence band electrons cannot be excited into the conduction band. Semiconducting materials have a much smaller band gap, of the order ∼1 eV. As such at room temperature and above it is possible for some valence electrons to be excited into the conduction band, thus leaving a hole behind in the valence band, referred to as an electron hole pair. In a semiconductor detector incoming photons interact within the detector generating electron hole pairs, with the number of pairs produced proportional to the incoming photon energy as follows:

$$N_{pair} = \frac{E_\gamma}{E_{pair}}, \tag{2.1}$$

where N_{pair} is the number of electron holes pairs created for an energy deposition of magnitude E_γ and E_{pair} is the energy required to liberate an electron into the conduction band. An electric field is then applied across the semiconductor, which draws electrons to the anode and holes to the cathode resulting in a current. This signal can be calculated using the Shockley-Ramo theorem. The change in charge induced on an electrode, L, by the movement of charge, q, from position, x_i, to x_f is given by,

$$\Delta Q_L = \int_{x_i}^{x_f} qE_0 \cdot dx = -q[\phi_0(x_f) - \phi_(x_i)]. \tag{2.2}$$

Here E_0 is the weighting field and ϕ_0 the weighting potential. These are defined given that the

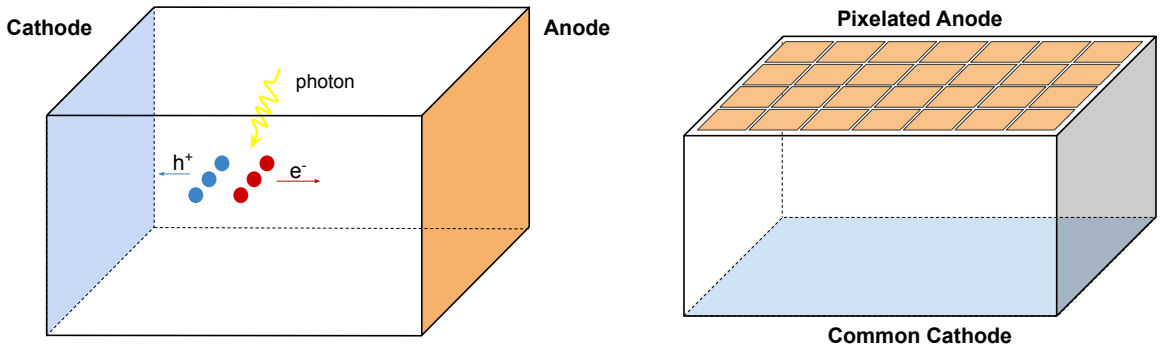

Figure 2.2: Left: A diagrammatic representation of a semiconductor detector. An incoming photon produces electron hole pairs which are then drawn to the anode and cathode respectively. Right: A pixelated anode.

electrode under consideration is at unit potential, all other electrodes are grounded and any other spatial charges have been removed.

The small amount of energy required to produce each electron hole pair makes this mechanism much more efficient than scintillator crystals, leading to higher energy resolution detectors, better than 3% FWHM for 511keV [Lev08]. This allows for the separation of incident photon energies differing by only a few keV, as apposed to scintillator detectors which require a much larger separation, e.g NaI(Tl) 20-80 keV. Another advantage of semiconductor detectors is the improved position resolution. They can achieve this as the segmentation is determined by the pixelation of the anode rather than the ability to arrange arrays of crystal elements [Gu11; Jo16]. It is also possible to use the timing of the anode and cathode signals to estimate the photon interaction coordinates in 3D - leading to the possibility of depth information [Lev08]. This would aid the removal of inter-crystal scatter (ICS).

Semiconductor detectors are limited by cost and difficulty in creating detectors with sufficient stopping power for x-ray and gamma ray photons. They are also vulnerable to degradation from radiation-induced damage.

Cadmium zinc telluride (CZT) is a frequent candidate for a solid state PET detector. It has been used by a group in Stanford in their design for a small animal PET detector [Gu11] and the 2011 Hitachi brain PET scanner with 152,024 CdTe detectors [Ini14].

CZT possesses a high atomic number and high density (5.78 g/cm^3) resulting in a good overall stopping power. Its wide bandgap, 1.6 eV, enables its use at room temperature as there is less contribution from thermally generated leakage current. Its uses are hindered however

by the low charge mobility and hole trapping. The trapping of holes leads to a low energy tail extending to the left of the photopeak. These events correspond to those in which the full γ energy was not detected at the electrodes. This reduces the overall energy resolution and charge collection efficiency. It also limits the maximum depth of detectors, which in turn limits the available stopping power. The main limitation of CZT however, is its timing resolution which is low compared to that of scintillator detectors, of the order of $\sim$10 ns compared to 100 ps for LYSO. Its uses are largely limited to small animal PET detectors and drug development trials. In these cases the small detector diameter means TOF-PET (see Chapter 3) cannot be applied and timing resolution is less critical [JCD19].

Chapter 3

Introduction to Positron Emission Tomography

Positron emission tomography (PET) is an imaging technique used to visualise metabolic processes inside the body. With the first scanner built in 1973, it is not a new concept, but with rapidly advancing detector technology PET imaging is of growing importance in the medical industry. It offers a non-invasive method of imaging the interior of the body and consequently has uses in a variety of areas including oncology, neurology and cardiology [VK15]. It is most commonly used as a diagnostic tool to detect and guide the treatment of cancers. However it is also an emerging methodology in diagnosing Alzheimer's disease. Its main advantage over other imaging modalities (e.g. computed tomography (CT) scans) is that it can provide quantitative analysis, allowing doctors to follow relative changes over time [Lev08]. Because PET highlights abnormal metabolic uptake of cells it can also distinguish between benign and malignant tumours, unlike CT scans which rely purely on tumour appearance. Another common use is to monitor blood flow and oxygen consumption in the brain, furthering our understanding and diagnosis of dementia, Alzheimer and strokes.

This chapter describes the basic principles of PET imaging, common challenges and limitations of the modality and the current state of PET research.

3.1 Basic Principles of Positron Emission Tomography

Prior to performing a PET scan the patient is injected with a radiotracer. This is a biologically active molecule in which one or more of the atoms has been replaced with an unstable radioisotope. The radiotracer circulates through the blood stream and is absorbed by cells, following the same pathway as its stable molecular analogue. Different radiotracers are used to follow

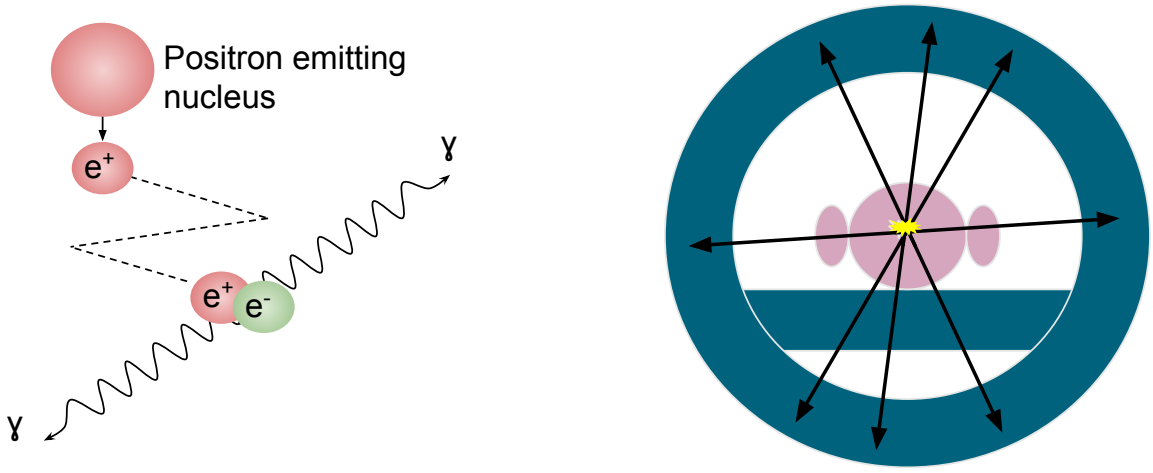

Figure 3.1: Left: A schematic showing radiotracer decay followed by positron electron annihilation. Right: Multiple lines of response (LORs) are collected and combined to from an image of the radiotracter distribution.

different biological pathways, depending on the purpose of the scan. Common radioisotopes include ^{18}F, ^{11}C and ^{15}O [Hua18]. The excess of protons to neutrons in the tracer nucleus causes the radionuclide to eventually decay, emitting a positron and a neutrino.

$$p \rightarrow n + e^{+} + \nu_{e^{-}} \tag{3.1}$$

The positron travels a short distance (∼mm) before interacting with an electron in the body and annihilating to produce two (near) back-to-back photons.

$$e^{+} + e^{-} \rightarrow 2\gamma \tag{3.2}$$

The two photons are detected by a ring of detectors surrounding the patient. Two detection events are determined to be in coincidence, and hence originating from the same annihilation, if they arrive within the same 'acceptance window', usually a few nanoseconds long [Lew08]. The location of this decay is then determined by drawing a line of response (LOR) between the two coincident detection events. It can then be assumed that the decay occurred somewhere along this line of response. Because we can constrain the photon path with two position coordinates, this method gives much better position sensitivity than conventional single-photon nuclear imaging [Fah02] and its resolution does not degrade with depth. It should be noted that even with the most precise detectors, this technique locates the position of the annihilation rather than the actual decay event. This adds an intrinsic limit to the spatial resolution

of all PET machines, resulting from the motion of the positron before annihilation. The distance the positron travels is dependent on the energy released during the nuclear decay (the Q value) which is unique to each radionuclide. Correct choice of radionuclide is therefore vitally important to optimise the achievable position resolution.

Once sufficient LORs have been acquired they are combined together to form a sinogram, which then undergoes some form of tomographic reconstruction to transform the data into an image. Common techniques for this are the filtered back-projection algorithm (FBP) and maximum likelihood estimator method (MLEM). These reconstruction processes shall be discussed in greater detail later in this chapter.

3.2 PET Systems in Practice

3.2.1 Types of Detection

PET detection events can be split into three categories, true coincidences, scattered coincidences and random coincidences. Each of these are illustrated in Fig. 3.2.

True coincidences are the ideal events. Neither photon interacts until it reaches the detector. A line of response drawn between the two detection events will therefore pass directly through the point of annihilation.

Scattered coincidences occur when one or both of the photons are scattered in the patient/air/bed/shielding before being recorded in the detector. The resulting line of response is displaced from the source. Since these photons will have lost energy whilst undergoing scattering, it is possible to somewhat reduce this effect by removing detected events that fall outside of an energy window. However, due to the limited energy resolution of the detectors they cannot be removed entirely. This drives the need for more expensive PET photon detection systems with higher energy resolution. The ratio of scattered events to true events can range from as low as 0.2 in brain scans up to 2 in 3D abdominal imaging [CSP12].

Random coincidences occur when two separate positrons annihilate and one photon from each annihilation is detected. When these annihilations occur in the same time window they are registered as a coincident event, and assumed to be from the same decay. The random coincidence count rate, R_{ab}, varies with the coincidence time window applied, τ, and the source strength. It can be calculated from the singles rate in each detector $N_{a/b}$ as follows [TZG03],

$$R_{ab} = \tau N_a N_b. \tag{3.3}$$

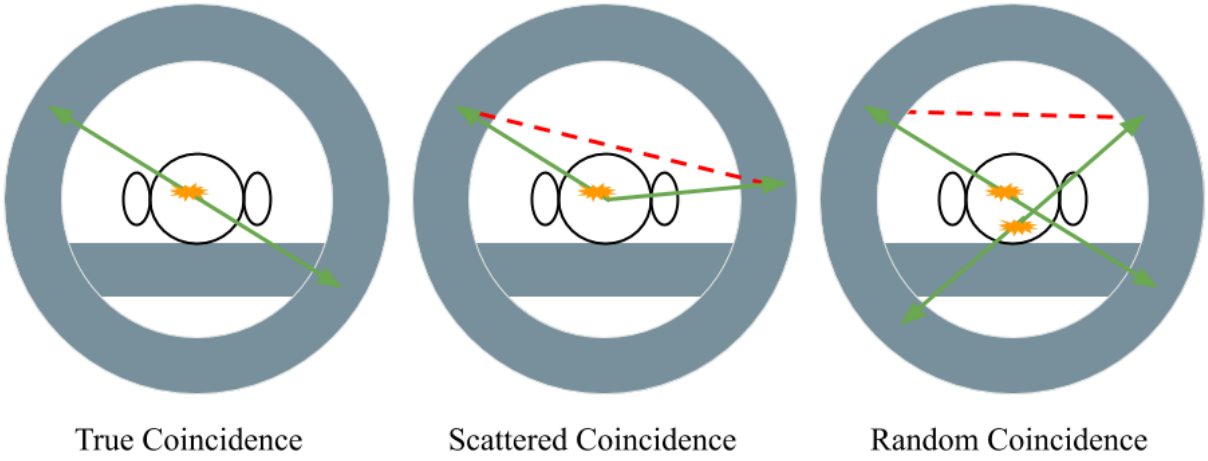

Figure 3.2: Three main event types in PET imaging. Both γ detected in the same coincidence window - a true coincidence. One or both γ scatter prior to detection - a scattered coincidence. Two γ from separate annihilations are detected in the same coincidence window - random coincidence.

Randoms events are usually corrected for by using a second "delayed" time window, which results in a data set containing only random events. This gives an estimate of the number of random coincidences in the "prompt" window [Bra05]. Alternatively this can be estimated from the singles count rates between two detector elements using Eq 3.3.

These random coincidences are slightly easier to correct for than scattered coincidences since they are distributed uniformly over time. They act to raise the background noise of the image. The ratio of random to true events ranges from 0.1 in brain scans to more than 1 [CSP12][VK15].

Of these event types only true coincidences give a LOR along which the annihilation occurred, the others simply manifest as noise in the reconstructed image. The relative contribution of each event type varies dramatically with the scan type, detector geometry, tracer activity and coincidence window. In a whole-body clinical PET scan operating in 3D mode roughly 50% of detected events are random coincidences, with 25% each of scatter and trues.

3.2.2 Inter Crystal Scattering

Scattering can occur not only within the field of view but also within the detectors themselves. There are many types of photon detector, all of which rely on photons interacting with the atoms forming the detector crystal, thereby transferring their energy to electrons. For PET photon energies, the dominant initial interaction in the detector is Compton scattering, with smaller contributions from photoelectric absorption. The (lower energy) scattered Compton photons can then lose the remaining energy through further Compton or ultimately photoelectric absorption processes.

When the interaction length in the detector medium is sufficiently small that both Compton scattering and the subsequent photoelectric absorption occur in the same element (or pixel) then the signal in the single pixel gives the total photon energy. If however the Compton scattered photon crosses a pixel boundary it will be detected as two separate events, known as inter crystal scatter (ICS). Depending on the detector material and segmentation this can make up 10-20% of events, and the push for next generation machines to have smaller pixel size to improve position resolution will lead to higher fractions. The ICS events can still be used to give position information if it is possible to determine which interaction occurred first. If not, either the energy weighted average of their coordinates are used, or these events are simply removed from the data set altogether [GBL04] [Wag14]. The proportion of ICS is dependent on the detector material and crystal size (resolution). For Lutetium-yttrium oxyorthosilicate (LYSO), a common scintillator crystal, ICS starts to dominate at a resolution of 1–2 mm, which corresponds to the attenuation length of Compton scattered 511 keV photons in LYSO.

In this work, rather than removing these events we hope to utilise the information they contain, exploiting the influence of quantum entanglement on the characteristics of ICS events to improve image quality.

3.3 Image Reconstruction

Detected lines of response are reconstructed into a clinically useful image by first combining them into a two-dimensional histogram called a sinogram, upon which a reconstruction algorithm is performed to reconstruct a 3D image. In general reconstruction algorithms can be split into two categories, analytical methods and iterative approaches. Analytical methods assume there is one unique solution to the reconstruction problem, however noise from low count rates means that this is rarely the case. Iterative reconstruction methods attempt to find the most likely solution. In recent years there has been huge interest in the improvement of these

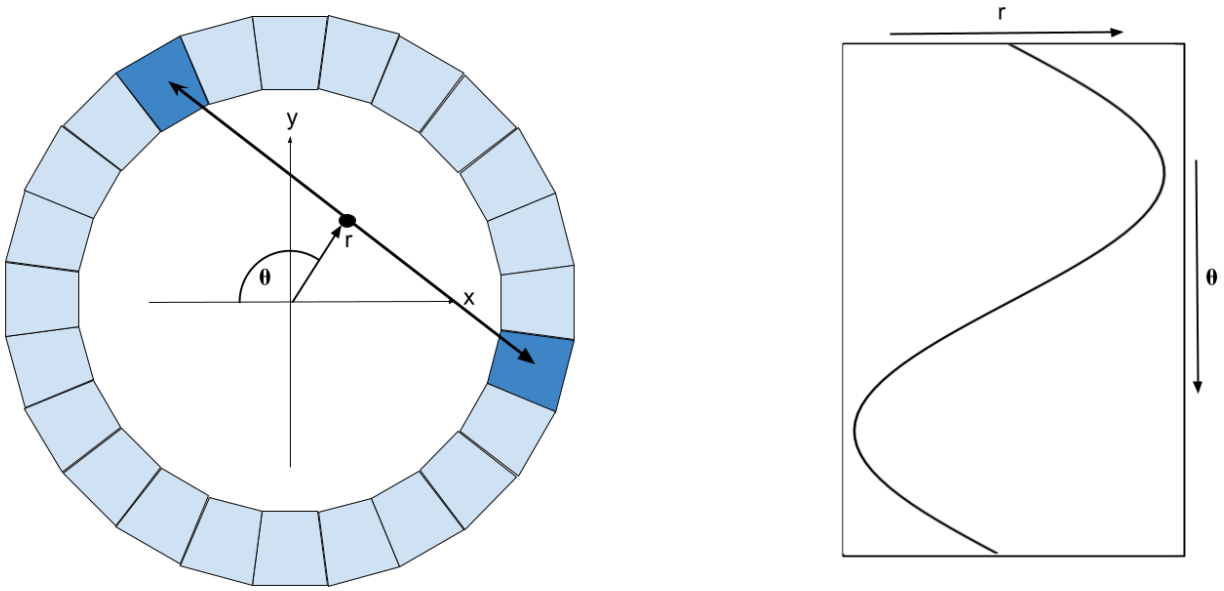

Figure 3.3: A schematic showing the parameters of importance in sinogram binning. A positron point source offset from the central axis annihilates creating two back-to-back photons. A LOR is drawn between the interaction coordinates of each photon. The radial displacement of the LOR from the origin, r, is shown, as well as the angle between the LOR and the x-axis, θ. Each LOR can be defined by these two parameters.

algorithms, with a trend towards the inclusion of machine learning techniques in iterative approaches. The most commonly used analytical, Filtered backprojection (FBP), and iterative, Maximum Likelihood Estimator Method (MLEM), reconstruction methods shall be discussed below.

3.3.1 Sinograms

Raw PET data is stored in a 2D array called a sinogram. Each individual bin of the sinogram represents a line-of-response (LOR) between two detector elements, and the value of that bin represents the number of events recorded along that particular LOR. LORs can be defined by two coordinates, the transaxial angle between the x-axis and the LOR, denoted θ, which is plotted on the y-axis, and the radial distance of the LOR from the centre of the detector ring, denoted r, plotted on the x-axis. Fig. 3.3 illustrates the sinogram of a point source off-set from the centre of the scanner. The resulting sinogram is sinosoidal, hence the origin of its name. A single row along the sinogram represents data from parallel LORs at a fixed radial offset and a projection can be formed by integrating along all LORs for a given θ.

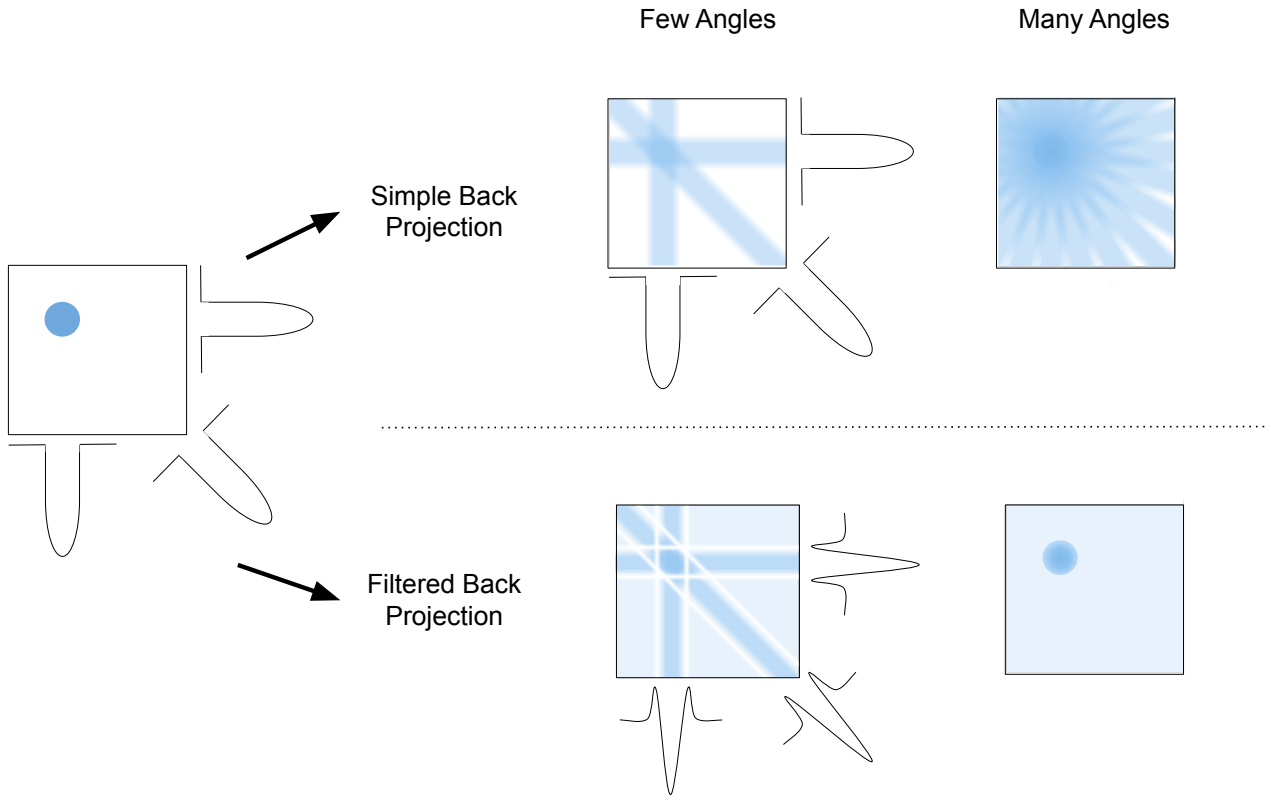

Figure 3.4: Top: A representation of the simple back projection algorithm. Bottom: A representation of the filtered back-projection algorithm.

3.3.2 Filtered Back-projection

The most commonly used analytical technique is the Filtered Back Projection algorithm, which was first developed in the 1960s for Computed Tomography [KDC04]. It is based on the simple-backprojection algorithm, a diagram of which is shown in Fig. 3.3. Multiple projections of the source distribution are taken by analysing rows along the sinogram. Each projection is then back-projected by spreading the detected counts along the path in the image matrix from which they originated. Counts are assigned to each pixel in proportion to the area of that pixel covered by the LOR.

Mathematically speaking a projection profile $p(r, \theta_i)$ is acquired for each angle, θ_i. This image is then reconstructed onto an image matrix with coordinate system (x, y). The back-projection of N profiles is given by,

$$f'(x, y) = \frac{1}{N} \sum_{i=1}^{N} p(x\cos\theta_i + y\sin\theta_i, \theta_i) \tag{3.4}$$

where $f'(x, y)$ represents the obtained approximation of the true source distribution and θ_i is the i^{th} projection. As can be seen from Fig. 3.4 this simple form of reconstruction, though effective, produces a blurred version of the original image, a feature that is intrinsic to the reconstruction algorithm. Mathematically the obtained source distribution is the convolution of the "true" source distribution $f(x, y)$ with a $1/r$ function. For a point source distribution, r represents the distance from the centre of the point source,

$$f'(x, y) = f(x, y) * (1/r). \tag{3.5}$$

These blurring effects can be removed by instead applying the filtered back-projection algorithm. In this instance each profile is transformed into frequency space, at which point a filter (most commonly a "ramp" filter, see Fig. 3.5) is applied, which selectively amplifies high-frequency components in the image, such as edges. The inverse Fourier transform is then applied to each projection to create modified (or filtered) profiles which are then passed through the standard back-projection algorithm,

$$f(x, y) = \frac{1}{N} \sum_{i=1}^{N} p'(x\cos\theta_i + y\sin\theta_i, \theta_i). \tag{3.6}$$

In this case the filtered profiles, $p'(r, \theta_i)$ are projected and the resulting distribution ought to match the "true" source distribution, $f(x, y)$ [CSP12]. The downside of this technique is that it also leads to the amplification of high-frequency noise, originating from low photon count rates. Consequently, images reconstructed with the FBP algorithm appear much noisier than those created with the simple back-projeciton algorithm.

The other limitation is that of "streak artefacts" which occur when two few projection angles are used, or projections are not distributed evenly over the full 180° range. These appear as dark ridges radiating out from sharp edges within the image and can interfere with image diagnostics. The algorithm is also limited by its inability to model factors such as inter-crystal scatter and positron range.

3.3.3 Maximum Likelihood Estimator Method

Iterative methods try to overcome these limitations by taking into account the noise structure of the measured projections and using prior knowledge of the imaging system. These methods are computationally much more expensive than simple analytical methods, and as such have been slow to be adopted into the clinical setting. However, improvements in computational speed and faster algorithms means they are now the standard reconstruction technique in most

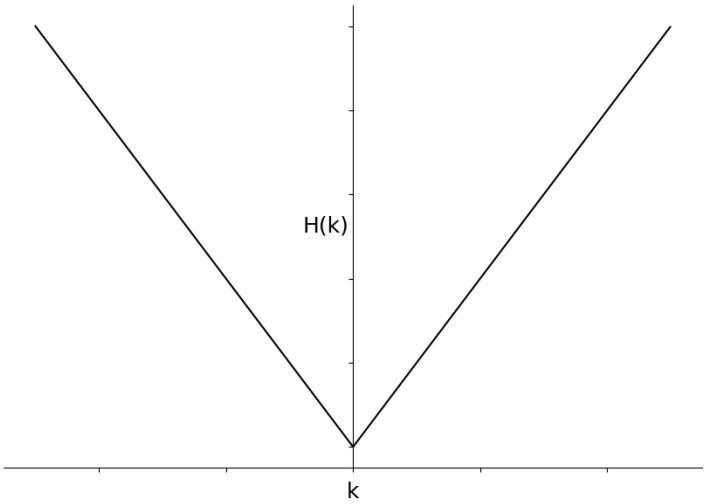

Figure 3.5: A ramp filter presented in the spatial-frequency domain. This filter removes the $1/r$ blurring from the simple back-projection by amplifying high frequency components.

modern PET machines [LM03].

Iterative methods model the imaging system using a "system matrix". This matrix describes the relationship between image space and sinogram space. Each element of the array defines the probability that an annihilation photon emitted from image location j will be detected in sinogram bin i for all pairs (i, j). The matrix can account for physical properties that effect the probability of detection in a particular bin such as the crystal block design, or uneven spacing between detectors due to the curved detector geometry [TAK10].

The general format of the algorithm is as follows. An initial estimated image of the radioactivity distribution is input into the algorithm. This could be a blank image, uniform or a simple filtered backprojection of the data. This estimated image is then forward projected to create an estimated projection. Forward projection is the inverse of the backprojection, the intensities along each ray path are summed up for all projections through the image. This estimated projection is compared to the actual recorded projection by taking the ratio of the two. This ratio is then backprojected into the image plane and used to provide a correction term for the current image estimate. Lastly the current image is multiplied by the correction to create a new estimate and the process is repeated. A schematic illustration of these steps is shown in Fig. 3.6. Each iteration should produce an image which more closely reflects the true activity distribution.

One downside to this technique is that the limited accuracy of the system matrix means fully converged images are likely to be very noisy. As such, these algorithms are generally

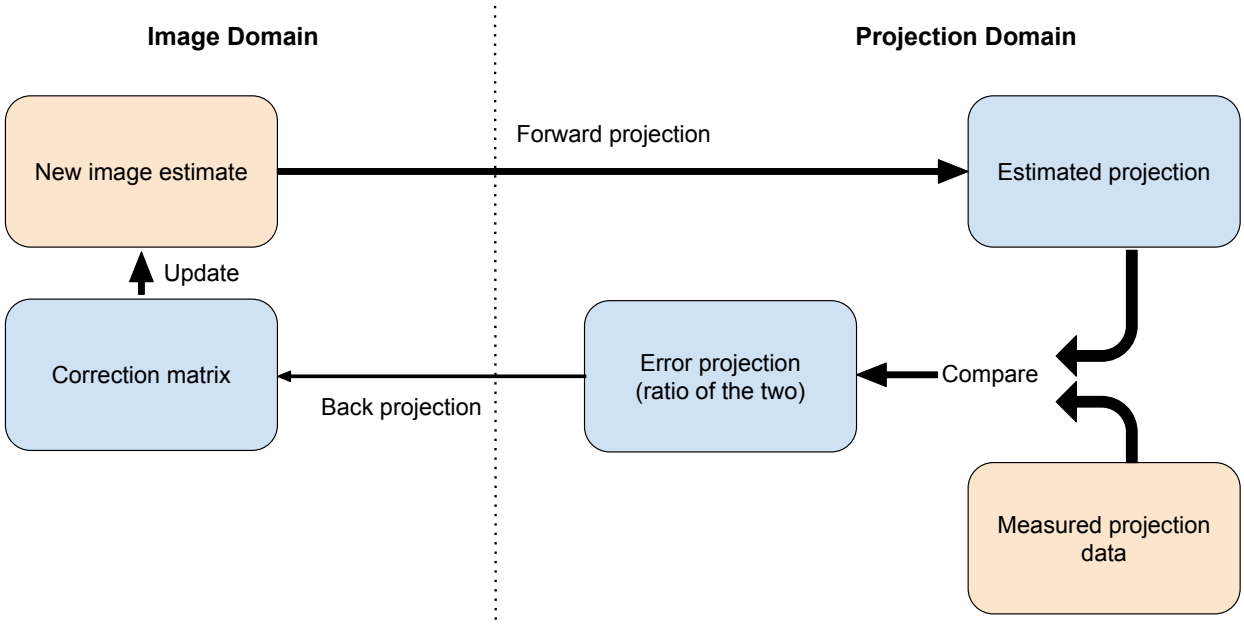

Figure 3.6: A schematic of the MLEM algorithm. The algorithm is initiated with a estimated image of the radioactivity distribution.

stopped after a specific number of iterations as a trade off between accuracy and noise. The second drawback is speed of convergence. For every iteration of the algorithm a forward and backprojection must be calculated. Typically 30-100 iterations are performed in an MLEM algorithm, compared to the FBP algorithm in which the backprojection is performed just once [RZ07].

3.3.4 Quantifying Image Quality

In PET, image quality defines how well the reconstructed image represents the true source distribution. Noise can play a huge part in degrading image quality creating artefacts that may hinder clinical diagnosis. As such it is vitally important to be able to quantify the quality of a given image. Image noise contributions can be both random or structured. Random noise arises from statistical variations in the counting rate whereas structured noise arises from non-random variations, for instance artefacts generated during image reconstruction or non-uniformities in the detector system.

A frequently used measure of image quality is the signal-to-noise ratio (SNR), the ratio between the average signal from the region of interest, μ_{ROI}, to the standard deviation, σ_{ROI},

$$SNR = \frac{\mu_{ROI}}{\sigma_{ROI}}, \tag{3.7}$$

it reflects the ability to determine a region of signal above the noise.

Another quantifier is the contrast-to-noise ratio (CNR). Contrast is the difference in signal between an object of interest and the image background. The CNR defines the visibility between different regions of interest and is calculated as follows,

$$CNR = \frac{|\mu_{ROI} - \mu_b|}{\sigma_b}, \tag{3.8}$$

where μ_{ROI} and μ_b represent the signal intensity in the active region and the background respectively and σ_b is the standard deviation of the background signal [Le 11]. The CNR becomes more important when an image has significant bias in it, if the average image intensity is high the SNR may by high, but the CNR could still be low.

3.4 Current Systems

With recent advances in detector technology the development of next generation PET systems is rapidly becoming an area of great interest. In this section some of the key developments shall be discussed, along with previous research into the use of photon polarisation in PET.

3.4.1 2D versus 3D mode

Old fashioned scanners e.g. (BGO) have limited energy resolution and hence struggle to reject scattered events solely through the application of energy windows. Instead they incorporate interplane septa, which act as collimators to reduce the number of scattered photons reaching the detectors. These septa stop incoming photons incident at large angles. However they also significantly reduce the sensitivity of the detectors, removing septa increases sensitivity x5-7 [Lod06]. Images acquired with the septa in the FOV are referred to as 2D mode and when the septa are removed it is referred to as 3D mode. Scatter fractions in 2D mode are of the order 10-20% but increase to 40-50% when the septa are removed.

3.4.2 Time-of-flight PET

The introduction of time-of-flight (TOF) PET is likely the biggest advancement in PET over the last decade. The technique was first suggested in early 1980s, however at that time the fastest available scintillator crystals lacked the spatial resolution and stopping power of the

conventional BGO PET scanners [FK06]. The idea resurfaced in the early 2000's when it was made possible by several new technological advancements, mainly fast photomultipliers, high density scintillators, fast electronics and better computing power for image reconstruction [Van16].

Standard PET relies purely on identifying LOR's but retains no information about where on each LOR the annihilation may have taken place. TOF on the other hand, employs detectors with excellent timing resolution (500-600 ps). This gain in timing allows measurement of the difference in arrival times between coincident photons. This information can then be used to constrain the annihilation to a certain location along the LOR (see Fig 3.7). During reconstruction TOF-PET LORs are back-projected through much smaller distances, leading to noise reduction and sensitivity gain. This technique shows particular promise for larger patients, since the gain is related to the ratio of object size to the spatial extent of the time-of-flight kernel. This is particularly significant since PET image quality degrades rapidly with increasing object size, due to higher scatter and increased attenuation. The first commercially available LYSO TOF-PET scanners were created in 2006 with a timing resolution of 585 ps [Sur06]. These days a move towards $LaBr_3$ and SiPMs can result in timing resolutions as low as 300 ps.

3.4.3 Combined Systems

In the 1990's there was great interest in combining functional PET scans with other anatomical scans to provide a more complete picture [Bey00]. Anatomical imaging techniques such as CT and MRI scans intrinsically have a much higher position resolution then a PET scan. Combining the two modalities can allow for better localisation of PET features within the body. Anatomical scans can also be used to create a patient specific map of attenuation sites within the body, which can then be used to correct for photon attenuation and scatter [ZE07]. This was a successful technique, however the devices were separate and generally required moving the patient from one scanner to another. This meant the main challenge lay in developing algorithms to successfully fuse the two images together accounting for movement of the patient between scans. The first hardware PET fusion was suggested in 1991 by Townsend and Nutt, who developed a combined PET/CT design [Tow08]. The two hardwares were combined and the scans taken sequentially, meaning the patient never had to leave the bed, resulting in minimal movement. This eventually led to the creation of the combined PET-CT scanner. Since 2001 such combined scanners have become commonplace and in recent years PET only scanners are no longer commercially available from many major vendors [JT17]. Early interest was also shown in combining PET with MRI, due to the better soft tissue contrast and no

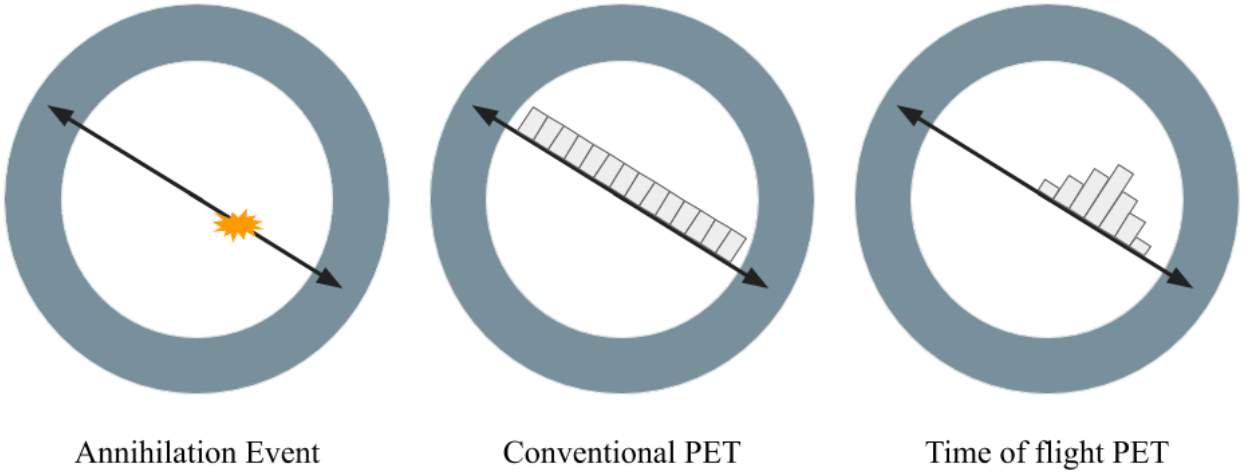

Figure 3.7: Representation of time-of-flight PET vs conventional PET. For a given annihilation event conventional PET weights every point along the LOR equally. In TOF-PET the difference in arrival times between the two γ allows localisation of the source.

radiation dose. However photo-multiplier based detectors cannot function under the strong magnetic fields required by MRI. The development of silicon photomultipliers (SiPMs) in 2010 finally made these possible, allowing the simultaneous incorporation of PET and MRI [Ehm17].

3.4.4 Whole Body PET scanner

The most recent addition to the PET market is the whole body PET scanner. Until now, whole body images could be retrieved by moving the patient slowly through the detector rings and taking successive images. This is the equivalent of several different scans added together. The first whole body scanner ever built is the UC Davis EXPLORER system in the United States [Rea19]. It is a combined PET/CT device utilising LYSO crystals attached to SiPMs. The scanner has an axial length of 195 cm, sufficient to cover an entire human body. Conventional PET scanners usually have an axial length of just 20 cm. The extended length gives the EXPLORER 40 times more sensitivity than conventional PET scanners. This opens the door for many new possibilities. Clinical scans could be performed in a fraction of the time (they claim less than a minute). Scans could be performed with extremely low radiation doses, making

it possible for PET scans to become a much more commonplace procedure. With this sensitivity a rudimentary scan can be produced in as little as a second, which opens up the possibility for live imaging, allowing the tracking of injected radiotracers through the body. This has applications in the study of drug absorption and distribution [Che17]. The cost of measuring a much wider field of view is the larger fraction of photons travelling through the body at oblique angles, with a correspondingly increased scatter probability compared to conventional PET systems.

3.4.5 Whole Gamma Imaging

A recent exciting new development is the concept of Whole Gamma Imaging (WGI) [Yos20]. In this technique an additional detector ring (used as a scatterer) is inserted inside the detector FOV, such that single gamma events can be identified through Compton kinematics. From the position coordinates and energy deposits of the first two interactions of any photon, it is possible to back project a cone of possible source positions, the same mechanism employed in Compton cameras. In the case of non-pure positron emitters, where an additional gamma is emitted near simultaneously, it offers the possibility of event localisation along the LOR by identifying the intersection of the LOR (from positron annihilation) with the Compton cone. It could also open up the potential for simultaneous imaging of PET and SPECT tracers, or multiple SPECT tracers with different energy isotopes. Lastly it offers the potential to increase the sensitivity of PET imaging by extracting useful information from PET events where only one annihilation photon was detected. A system such as this, designed with the detection of scattered events in mind, is an obvious candidate in which the techniques discussed in this thesis could be applied in the future.

3.5 Applications of photon polarisation to PET imaging

Measurement of gamma ray polarisation by observance of the Compton scattering distribution is only just beginning to find place in modern technologies, for example applications can be found in astrophysics [LDH97][Tak10]. In recent years there has been growing discussion around the use of photon polarisation to provide additional information in PET scans. Back in 1992 it was first suggested that the incorporation of photon polarisation in Monte-Carlo simulations of PET scans would improve scatter estimates [Bic92].

The use of photon polarisation correlations in PET to perform event discrimination was first proposed in 2011 [Kun11]. In their later 2014 paper they demonstrated, using a hypothetical

detector system capable of determining photon polarisation, that better event discrimination between true and scattered events can be achieved compared to employing current energy window techniques [McN14]. In their 2016 paper they extend this simulation to consider an idealised dual-head Compton camera detector system and simulate the behaviour of independent polarised photons [Tog16]. They propose a scheme by which to classify events as true or false coincidences depending on their scattering angle. Using this classification scheme they managed to show improvement in the signal to background ratio of reconstructed images. The quantum theory by which they derive their scheme is correct, however the simulation from which they collect their results does not include quantum entanglement effects (discussed in Chapter 1). The inclusion of these effects ought to result in an even greater improvement.

There have also been investigations by the JPET collaboration, who have designed a PET scanner built entirely of plastic scintillator strip detectors. It is composed of 4 axial rings with increasing radii allowing for the re-detection of photons scattering within the first ring, effectively acting as a Compton camera. In their 2018 feasibility study [Mos18] they simulate independent, polarised γ within the JPET detector to determine the ability of the system to detect these angular correlations. They demonstrate the loss of sensitivity imposed by the necessary selection criteria to extract this enhancement.

Most recently Makek et al [Mak20] successfully achieved a measurement of the polarisation correlations between annihilation gamma using single-layer Compton detectors. Their system comprised 2 modules each encompassing a 4x4 matrix of Lutetium Fine Silicate scintillators attached to an SiPM array. They demonstrate the $\cos(2\Delta\phi)$ modulation, measuring a maximum amplitude which exceeded that predicted by standard Geant4.

Chapter 4

Measuring $\Delta\phi$ correlations in Cadmium Zinc Telluride

The first aim of this project was to validate the new modified Geant4 simulation, which incorporates the scattering correlations of annihilation photons (see Chapter 1). To do this a PET demonstrator apparatus was created. Built from CZT crystals it has a significantly higher energy and position resolution than standard clinical PET scanners, which allows for easy tracking of the photon trajectory inside the crystals. This in turn enables high resolution measurements of ϕ scattering angles. Two CZT detectors were bought using a collaborative Innovate UK grant with Kromek Ltd. They were setup at York in January 2019 and I have made important contributions in setting up, obtaining the data and developing the Geant4 simulations for this new system.

In this section we present feasibility studies performed to test the capability of these detectors to measure $\Delta\phi$ correlations. The experimental setup and the Geant4 simulation of the system are described, along with the charge sharing compensation applied. The obtained $\Delta\phi$ distributions for both experimental and simulated data are presented, validating the QE-Geant4 modelling. Lastly an experiment is performed to test the magnitude of any residual $\Delta\phi$ correlations remaining after a previous scatter.

4.1 Overview and simulation study of DCS characterisation in segmented detector arrays

In order to measure $\Delta\phi$ a setup was required in which the two positron annihilation γ undergo a Compton scattering interaction followed by a subsequent re-detection. From the coordinates

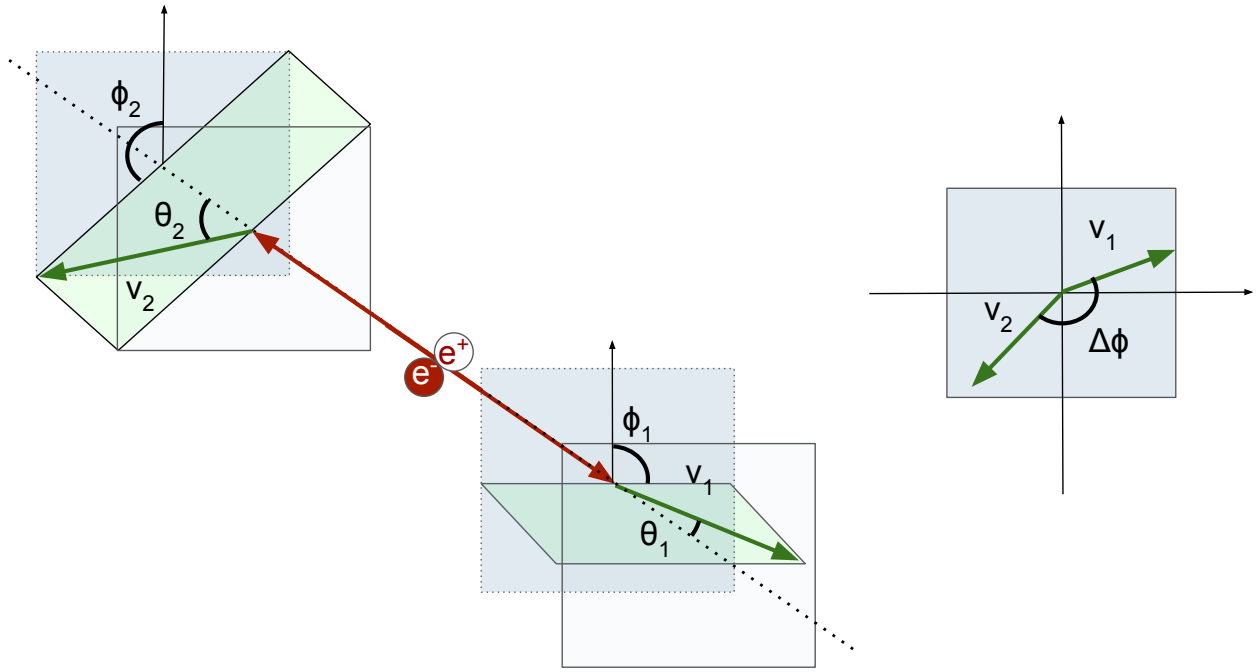

Figure 4.1: Schematic of the ideal double Compton scattering event. The two annihilation γ, represented by the red arrows, each hit the detector and interact via a Compton scatter. The scattered γ, green arrow, is then re-detected elsewhere within the same detector head. From the coordinates of their interactions $\Delta\phi$ can be calculated for the γ pair.

of each of these interactions the polar scattering angle, θ, and azimuthal angle, ϕ, could be extracted, enabling the calculation of $\Delta\phi$. In the experiment the CZT detectors were employed both as the scatterer and the absorber (much like a Compton camera). The incoming γ would Compton scatter in one pixel, transferring energy to a recoil electron, and then be re-detected elsewhere within the same detector head, either through undergoing a second Compton scatter or via photoelectric absorption. A schematic showing the ideal interaction and angles of interest is shown in Fig. 4.1.

Prior to any measurements, feasibility studies were run using the new QE-Geant4 simulation. Since the interaction we are looking for is very specific and very rare, it was necessary to ensure the equipment in question was capable of detecting it. Both annihilation γ needed to be detected within a CZT crystal without any prior interactions. Both 511 keV γ must undergo a Compton scatter as their first interaction inside the crystal, with sufficient energy transferred to be detected above the noise threshold. Both scattered γ must then be re-detected in the same detector head, either through the photoelectric effect or by a second Compton scatter. This second detection must be a sufficient distance away from the first such that they can be

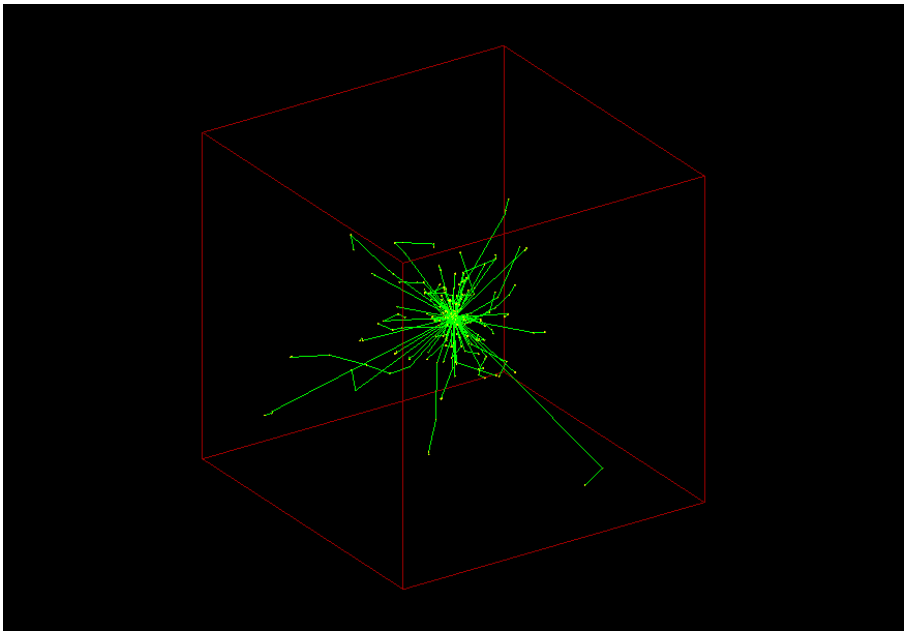

Figure 4.2: Geant4 rendering of 50 positron-electron annihilations inside a 100 x 100 x 100mm cube of CZT. The photon trajectories are shown by the green lines, with interaction points represented by yellow dots.

easily identified as separate interactions, rather than the result of charge sharing. A greater separation also increases the angular resolution.

First we simulated a positron inside a CZT detector of dimensions 100 x 100 x 100 mm. This is sufficiently large that it essentially acts as an infinite detector, simulations show that only ∼1% of 511 keV γ do not deposit their entire energy within the crystal. A Geant4 rendering of the setup is shown in Fig. 4.2. The probabilities of each possible interaction of the annihilation γ in this CZT configuration are shown in Table 4.1. The high cross section for Compton scatter is immediately evident, with ∼80% of the first interactions being through a Compton scatter.

Table 4.1: Interaction probabilities for a 511 keV annihilation photon in a 100 mm^3 block of CZT.

Interaction Type	Probability (%)
First interaction Compton scatter	81.7
First interaction photoelectric absorption	17.5
Photon lost	0.8
Compton-Compton	46.7
Compton-photoelectric	30.98

We then limited our data set to only consider events in which both γ underwent a Compton

scatter as their first interaction and were subsequently re-detected. The coordinates and energy depositions of each interaction were recorded. Fig. 4.3(a) shows the distribution of energies deposited by the photons in their first and second interaction, shown by the red and blue lines respectively. The energy transferred during the first Compton scatter clearly peaks at 340.7 keV, corresponding to the case of complete backscatter with $\theta = 180°$. The energy deposited by the scattered photon peaks correspondingly at 170.3 keV, when all of the remaining energy is deposited through photoelectric absorption. Both spectra exhibit a large low energy tail, corresponding to events where the total γ energy was not deposited within two interactions, most likely due to the scattered γ going on to interact via yet another Compton scatter.

The polar scattering angle θ was extracted from the momentum vectors of the particles in Geant4, and its distribution is plotted in Fig. 4.3(b), peaking for small angles around 35°. The azimuthal scattering angle ϕ was similarly extracted and is plotted in Fig. 4.3(c). The flat distribution shows scattering is independent of ϕ, and hence scattering at any given ϕ angle is equally likely to be observed.

For each γ pair, the difference between the azimuthal scattering angles $\Delta\phi$ was calculated and the resulting $\cos(2\Delta\phi)$ distribution is shown by the green line in Fig. 4.3(d). The distribution has been normalised such that the trough of the distribution sits at 1 to allow better comparison of the overall amplitude. The cosine distribution resulting from the entire simulated data set peaks at an amplitude of 1.285. The red and blue bands in Fig. 4.3(d) demonstrate the effect of constraining events to be within certain θ bins. For $50° \leq \theta \leq 70°$ the peak of the consine distribution increases to an amplitude of 1.72, and for $70° \leq \theta \leq 90°$ (a θ bin centred approximately around the maximum value $\theta_c = 81.7°$) this amplitude increases to 2.62. It should be noted that this is still smaller than the maximum predicted R ratio of 2.85 (see Chapter 1) due to integration over a larger θ range (a reasonable range of θ was necessary in order to maintain sufficient statistics in the simulation).

The same measurement is then repeated with the dimensions of the CZT cube replaced by those of our in-house CZT detectors, in order to observe any effects of their limited geometry on the γ acceptance. These detectors have a sensitive volume of 8.8 x 8.8 x 10 mm. The two detectors were placed at a separation of 100 mm, with a source of stationary positrons produced equidistant between the two detectors. Table 4.2 shows the probability of each event sequence for a beam of back-to-back entangled photons, incident on the two CZT detectors. The small size of these detectors and low stopping power is highlighted by the high probability ($\sim$85%) that at least one of the two γ will not undergo an interaction inside a detector. The usable yield corresponds to events undergoing first a Compton scatter followed by a second energy deposition. These make up just 1.3% of the total annihilations.

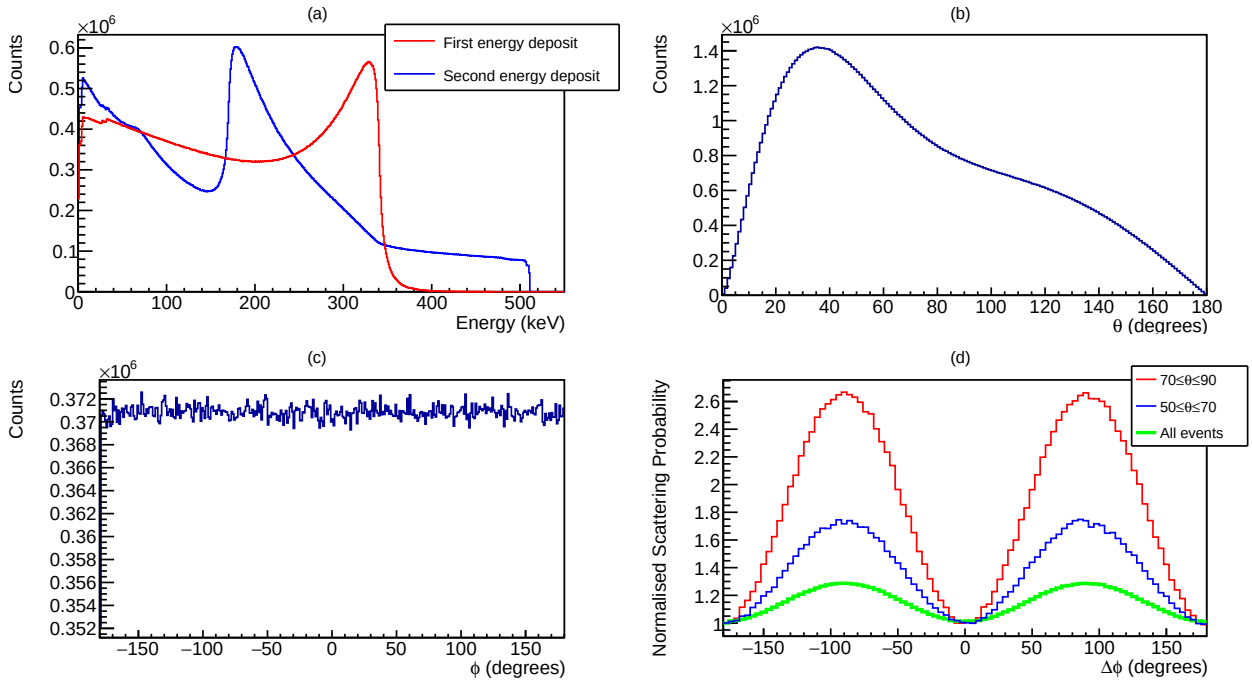

Figure 4.3: Simulation results from a positron source annihilating in an "infinitely" large detector. (a) Energy deposited in the first (red) and second (blue) photon interaction. (b) Distribution of the polar scattering angle θ. (c) Distribution of azimuthal scattering angle ϕ. (d) $\Delta\phi$ distribution for all events (green) and events with $\theta_1 = \theta_2 = \theta$ in specific θ cuts (red and blue). Each $\Delta\phi$ histogram is normalised relative to $\Delta\phi = 0$, allowing clear comparison of the correlation amplitude.

Table 4.2: Interaction probabilities for a beam of back-to-back entangled photons incident on two CZT detectors (8.8 x 8.8 x 10 mm)

Interaction Type	Probability (%)	Inclusion of Rayleigh
Both γ Compton scatter	10.14	9.91
Both γ photoelectric	0.47	0.46
One photoelectric, one Compton scatter	4.36	4.26
At least 1 γ does not interact	85.03	
Both γ Compton, Compton	0.37	0.35
Both γ Compton, photoelectric	0.29	0.27
One Compton-Compton, one Compton photoelectric	0.64	0.60

The energy deposited through the first and second interaction of each γ (for this new detector geometry) is shown in Fig. 4.4(a). Compared to the case of an "infinite" cube, there is a noticeable reduction in the low energy tail. Since low energy events correspond to low θ

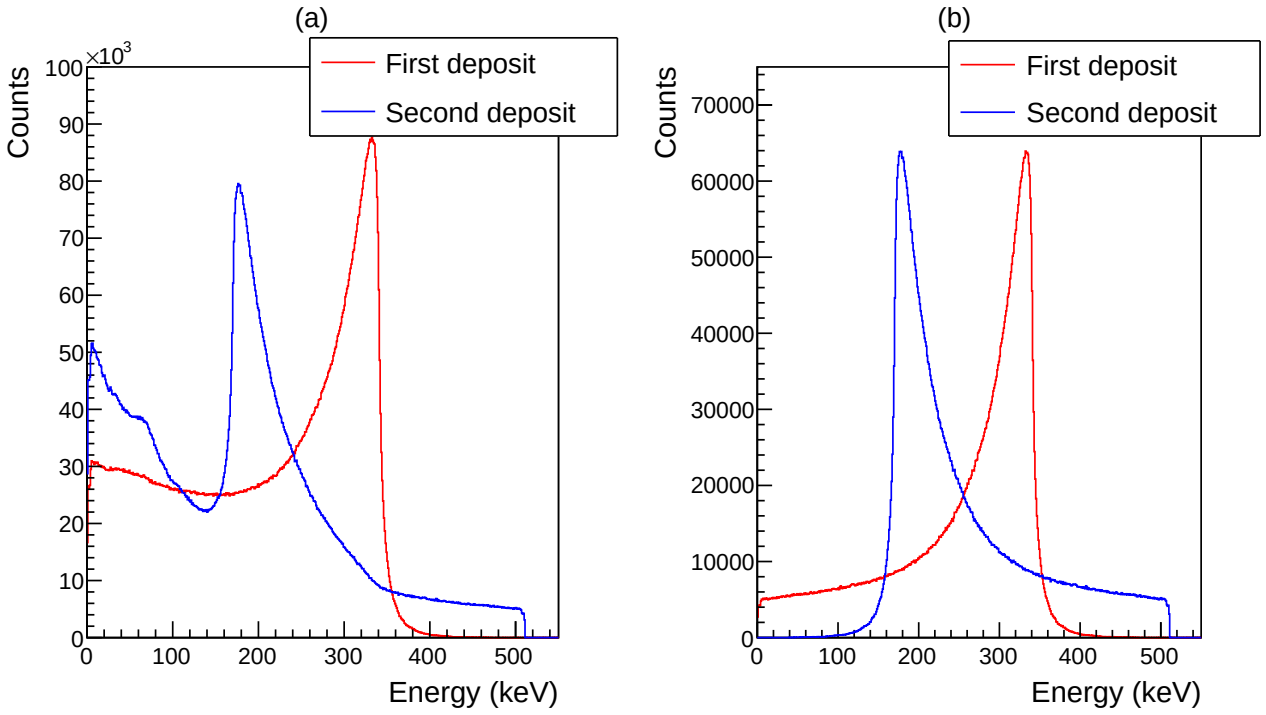

Figure 4.4: Simulated energy deposits from 511 keV γ incident on 8.8 x 8.8 x 10 mm^3 detectors. **Red** - Spectrum of energy deposits for each photon's first interaction. **Blue** - for the second interaction. (a) The energy distribution for all events, (b) only events in which the entire 511 keV is detected.

scattering angles, it follows that these events are less likely to be detected in our limited system as the highly energetic scattered γ exits through the back of the detector. Consequently our data set is biased towards larger scattering angles, as can be seen in Fig. 4.5. This is fortunate as the $\Delta\phi$ correlations we are looking for are most prominent at $\theta \sim 81.7°$.

Events in the low energy tail will be challenging to identify accurately, as both energy depositions will be low and difficult to detect above the noise. We can remove these events by requiring the sum of the first two interactions to equal 511 keV. The resulting distributions are shown in Fig. 4.4(b).

The most noticeable difference lies in the $\Delta\phi$ distribution shown in Fig. 4.6(a). Rather than being a $\cos(2\Delta\phi)$ distribution it is now no longer symmetric about 90°. The probability of detecting an event with $\Delta\phi = 0°$ is significantly lower than the probability of both photons scattering with $\Delta\phi = \pm 180°$. This is a detector acceptance effect purely caused by the limited size of the detector crystals. The explanation for it is as follows. If γ_1 first interacts in the center of detector 1, then the probability of detecting the scatter photon will be approximately independent of the ϕ scattering angle. Since the two photons travel back-to-back, γ_2 will also

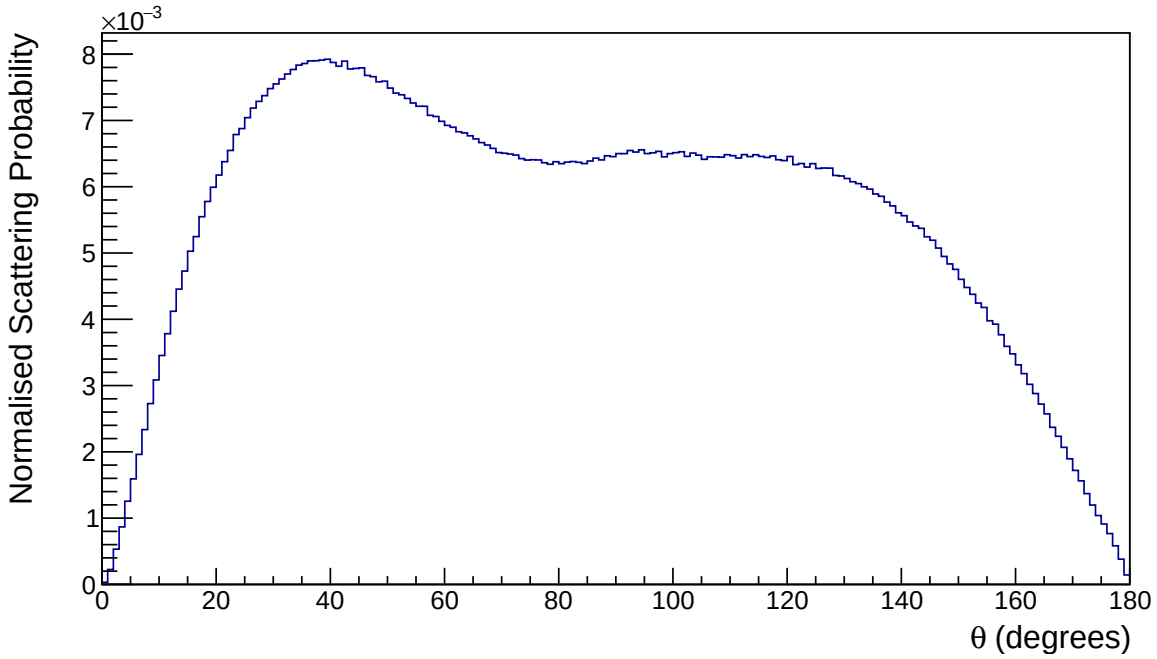

Figure 4.5: Simulated theta distribution of double Compton scattered events inside CZT detectors of dimensions 8.8 x 8.8 x 10 mm.

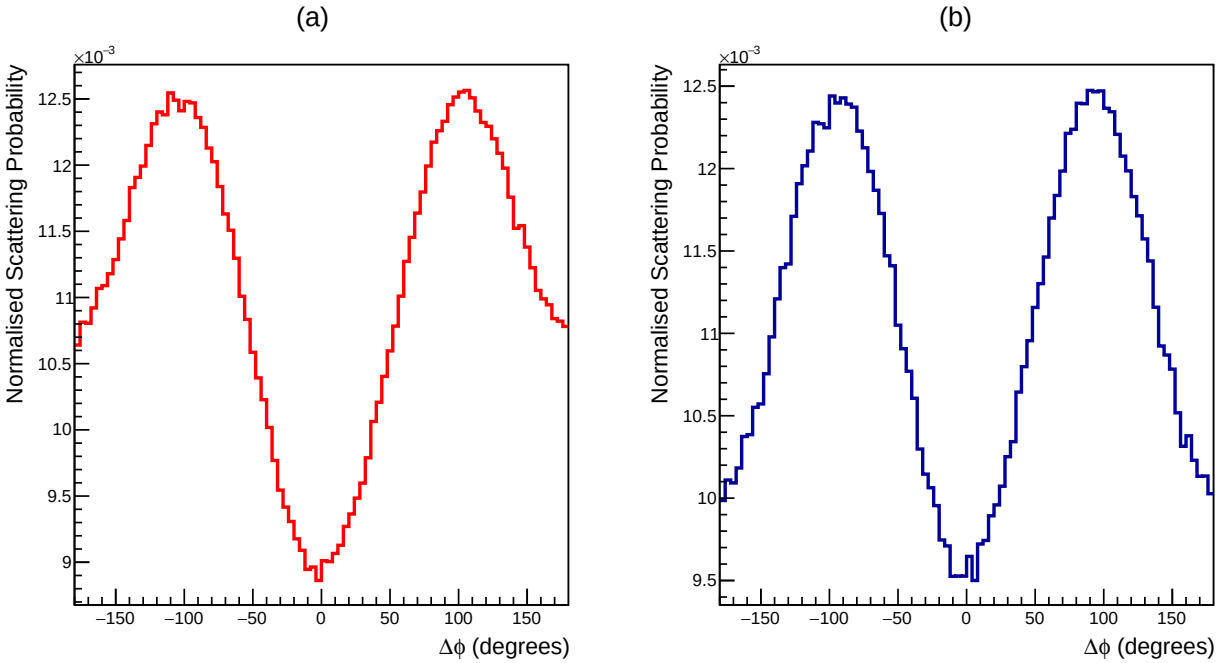

Figure 4.6: $\Delta\phi$ distribution from QE-Geant4 simulation of CZT crystals. (a) $\Delta\phi$ of all events, (b) $\Delta\phi$ of events whose first interaction occured within 3 mm of the crystal center.

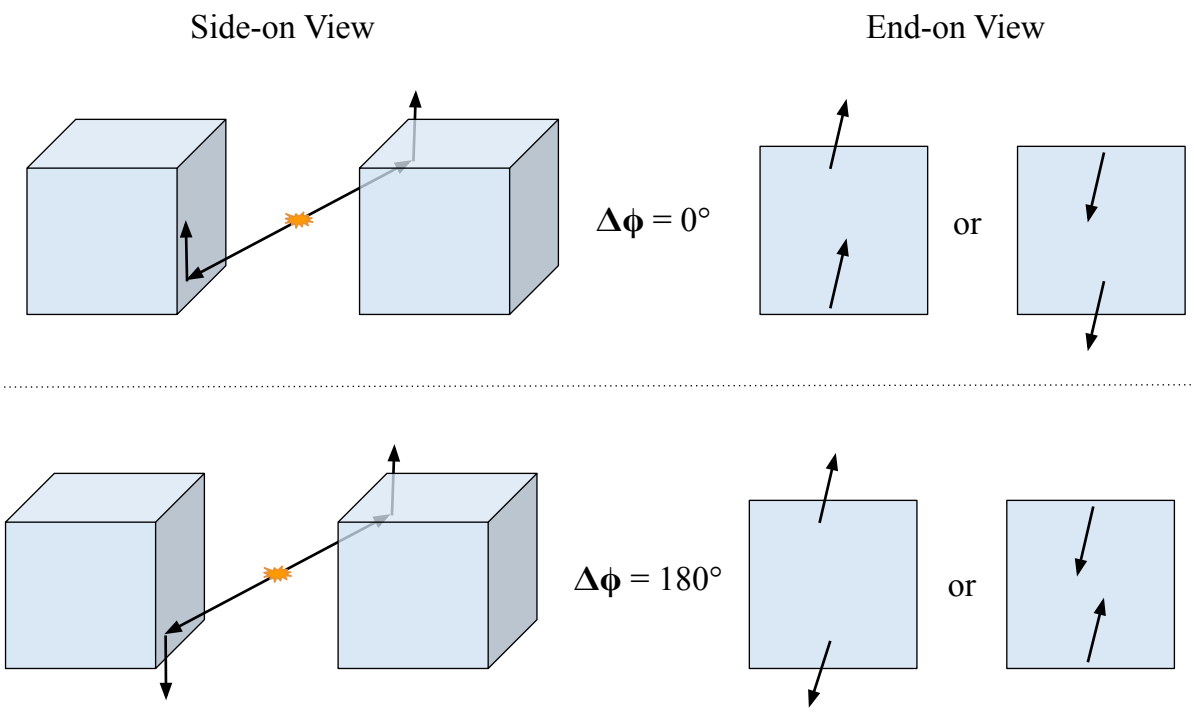

Figure 4.7: The origin of edge effects from finite crystal sizes. If both γ hit the edge of the detector and scatter with $\Delta\phi = 0°$ the event is lost in 100% of cases (top panel). If the γ scatter with $\Delta\phi = \pm 180°$ a complete event is recorded in 50% of cases (bottom panel).

hit the center of detector 2. However if γ_1 were to first scatter at the edge of detector 1, γ_2 would consequently hit the opposite edge of detector 2. If both photons then scatter with the same ϕ ($\Delta\phi = 0$) then one of the photons will escape the detector in almost 100% of cases. However, if the two photons scatter in opposite directions ($\Delta\phi = \pm 180°$) both photons are detected in 50% of cases. A diagram depicting this logic is shown in Fig. 4.7. The effect can thus be removed by requiring that the first photon interaction occurs within the central pixels. The same $\Delta\phi$ distribution is plotted in Fig. 4.6(b) with the added requirement that the first interaction in every event occurs within 3 mm of the center of the detector. This restriction effectively restores the symmetry of the cosine distribution.

4.2 Experimental Setup

Two cadmium zinc telluride (CZT) detectors were aquired to perform this measurement. They were developed by the Kromek Group and are based on the DMatrix detector system [McA17].

The CZT crystals have dimensions 8.8 x 8.8 x 10 mm. A segmented anode divides each

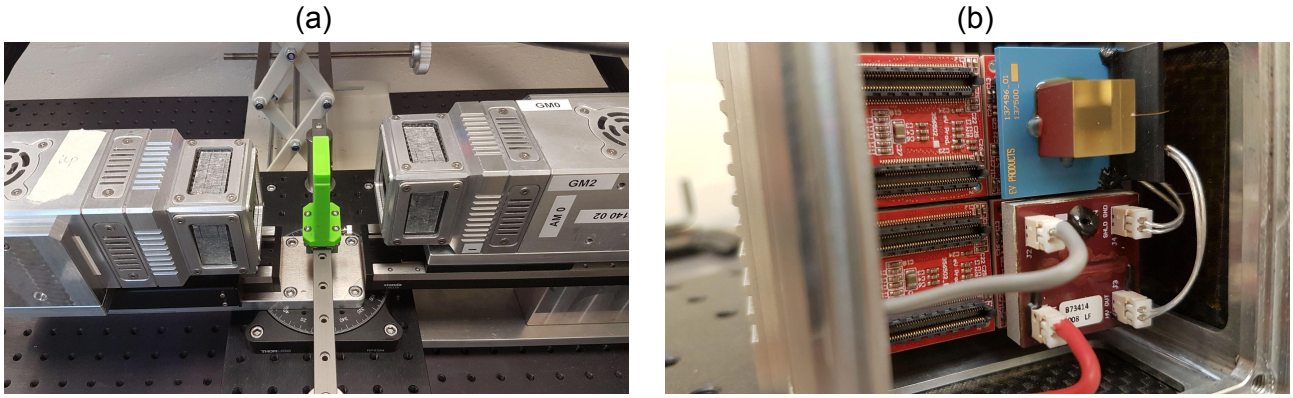

Figure 4.8: Photographs of the laboratory equipment. (a) CZT detectors placed equidistant around a ^{22}Na source. The source itself sits within the green holder. (b) A close up of the detector head with the carbon-fibre window removed. The 8.8 x 8.8 x 10 mm CZT crystal is mounted on the blue board.

crystal into 121 pixels in an 11 x 11 arrangement, with each pixel having dimensions 0.64 mm^2. Fig. 4.8(b) shows a photograph inside one detector head. This is a prototype array for research and development comprising only 2 crystals. The system would be capable of having 2 crystals on each head, and this is envisaged at a future stage in the project. Each detector works independently but the two heads rely on the same clock, allowing for the identification of coincident events. Whenever one pixel in the array is triggered by a signal above 50 keV, a delay time of 2 μs is initiated to allow all other signals in the detector to rise to their peak amplitude. Subsequently, every triggered pixel in the detector (along with all their neighbours) are read out and assigned the same timestamp. When events are detected in each head with the same timestamp, they are deemed to be coincident and originating from the same annihilation.

An image of the experimental setup is shown in Fig. 4.8(a). Each CZT detector head was mounted on a rotation stage to enable precise positioning and orientation. The heads were separated by a distance of 16 cm, with a ^{22}Na source of 350 kBq placed equidistant between the two.

^{22}Na decays via β^+ decay into stable ^{22}Ne. 0.06% of decays lead directly to stable neon. The rest lead to an excited state via electron capture (9.5%) or through positron emission (90.2%). Excited neon then decays into ground state by emitting 1275 keV γ, since the excited state lifetime is only 3.7 ps this is within the coincidence timing of our setup but can be identified from its energy deposit.

4.2.1 Deadtime

In all detectors there is a minimum amount of time that must separate two incoming photons in order for them to be detected as separate events. This is referred to as the deadtime [Kno10]. At low activities, the probability of an event being lost because two decays happened in quick succession is negligible. However, as the count rate increases these effects can become much more problematic. Deadtime can originate from processes inside the detector (e.g. electron drift time in CZT) or it may arise from the readout electronics. The result is a non-linear relationship between incident and measured count rate. The deadtime in our system was determined using the two-source method [Mye56]. In this technique the count rate is acquired for two sources individually and in combination. The deadtime can be calculated providing that the sum of the radiation rates observed from individual sources is greater than that observed for the two sources in combination [Aky21]. The deadtime, τ is calculated as follows,

$$\tau = \frac{X(1-\sqrt{1-Z})}{Y} \tag{4.1}$$

where

$$X = m_1 m_2 - m_b m_{12} \tag{4.2}$$

$$Y = m_1 m_2 (m_{12} + m_b) - m_b m_{12}(m_1 + m_2) \tag{4.3}$$

$$Z = \frac{Y(m_1 + m_2 - m_{12} - m_b)}{X^2} \tag{4.4}$$

where m_1 is the measured count rate of source 1, m_2 the measured count rate of source 2, m_{12} the measured count of the two sources combined and m_b the measured count rate with no sources [McA17].

For this experiment two point sources of Na22 were used with activities of 141 kBq and 2.80 MBq. The resulting deadtime was calculated to be $(18.1 \pm 0.4)\mu s$.

$\mathbf{m_1}$ **(cps)**	$\mathbf{m_2}$ **(cps)**	$\mathbf{m_{12}}$ **(cps)**	$\mathbf{m_b}$ **(cps)**	$\tau(\mu s)$	**Error** (μs)
222	4272	4458	3	18.1	0.4

4.2.2 Geant4 simulation of CZT Setup

The exact experimental setup was reconstructed using our new quantum entangled Geant4 (QE-Geant4). The detectors were modelled as two blocks of CZT crystal. A spherical ^{22}Na source of 1 mm diameter encased in a cylindrical disk of epoxy resin (thickness 3 mm, radius

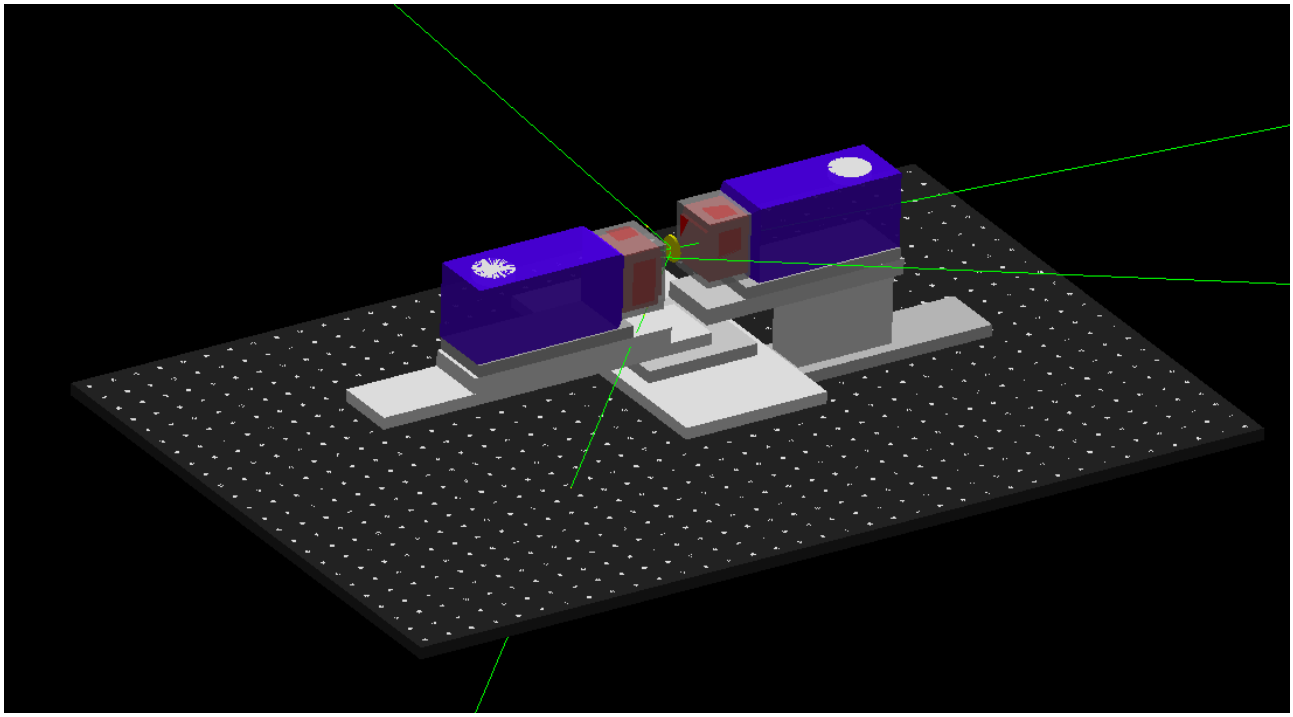

Figure 4.9: A Geant4 rendering of the full CZT detector setup. The source is encased in an epoxy resin disk, shown in yellow. Each CZT crystal sits in the top right hand corner at the front of the detector head.

12.5 mm) was placed equidistant between the two. The implementation of the source in the simulation accounted for all decay possibilities with their appropriate probabilities (including the prompt 1.2 MeV γ from neon decay). Energy deposits in the CZT were smeared to match the experimental energy resolution of each detector head (3.8% and 5.3% FWHM at 662 keV). The position coordinates of the simulated energy deposits were also pixelated to match the discretised position resolution of the laboratory detectors.

A Geant4 rendering of the setup is shown in Fig. 4.9. The aluminium box encasing the detector electronics and the support system were also incorporated into the simulation to account for any contributions to the yield from γ backscattered into the CZT acceptance.

4.2.3 Modelling charge sharing in CZT

A downside of the increasing pixelation of modern semiconductor detectors is the significant increase in charge sharing. This occurs when the energy deposited through one γ interaction is spread between multiple adjacent pixels. Adjacent clusters of triggered pixels can therefore either result from multiple gamma interactions in different pixels, or from a single electron cloud being shared between adjacent pixels. If the cloud is created in the gap between two

Photon Energy (keV)	Inital Charge Cloud Size (μm)	Diffusion Contribution (μm)	Total Charge Cloud Size (μm)
59.5	3	80	80
122	12	80	81
356	80	80	113
662	190	80	206

Table 4.3: Initial charge cloud size in CZT as a function of energy deposit, results taken from [Kim11].

pixels, charge may be collected by more than one. Since each individual pixel has a noise discrimination threshold that must be exceeded to register as an event, this can result in degradation of the energy resolution. Charge can also be lost to the inter-pixel region, as such events with multiple pixels tend to have a lower energy resolution when compared to single pixel events. When energy is deposited within the CZT crystal a number of electron-hole pairs are generated, proportional to the energy deposited. The initial size of this charge cloud can be estimated by tracking the path of all gamma and electron energy deposits, including secondary photons e.g. characteristic x-rays. The Geant4 results of [Kim11] model how the initial charge cloud diameter varies with the energy of the incident γ. Their results are summarised in Tab. 4.3. They found diameters varying from 3 μm for 59.5 keV to 190 μm for 662 keV.

As this charge cloud travels through the crystal it disperses by two main effects, Einstein diffusion and Coulomb repulsion. The random thermal motion of electrons causes the cloud to expand as it drifts and is described by

$$\sigma = \sqrt{\frac{2kTdD}{eV}}, \tag{4.5}$$

where k is boltzmann constant, T is the absolute temperature, d the drift distance, D the detector thickness, e the unit charge and V the detector bias. The negatively charged electrons also disperse through self repulsion [Gat87], where the standard deviation of the spread is given by,

$$\sigma = \left(\frac{3\mu_e N e t_{drift}}{4\pi\epsilon_0\epsilon_R}\right)^{\frac{1}{3}}, \tag{4.6}$$

with μ_e the electron mobility, N the number of charge carriers, ϵ_0 the permittivity of free space and ϵ_r the relative permittivity. The drift time, t_{drift}, is defined as

$$t_{drift} = \frac{dD}{\mu_e V}. \tag{4.7}$$

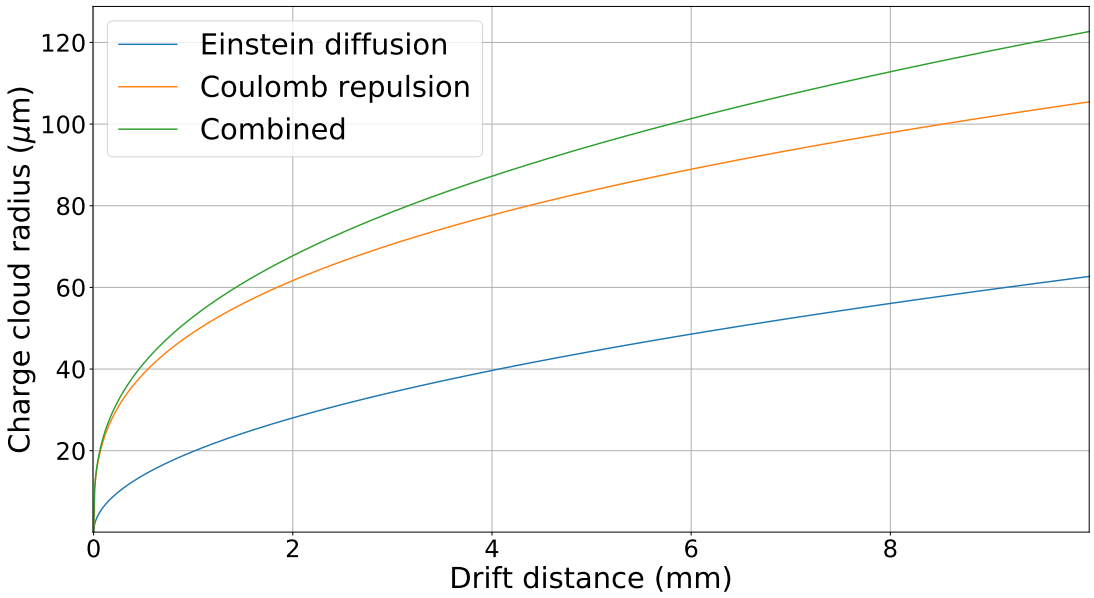

Figure 4.10: Behaviour of diffusion and coulomb repulsion within increasing drift distance for 250 keV energy deposits.

The total charge cloud could then be estimated as the root mean square of the contributions from diffusion and Coulomb repulsion, and the initial cloud radius. The relative contribution of each of the latter effects is shown in Fig. 4.10.

Using the results of [Kim11], the initial charge cloud created by a 250 keV energy deposit (a 511 keV γ scattered through $\sim 82°$) is on average 0.05 mm in radius. In the worst case scenario, in which the cloud drifts the full length of the detector, the combined charge cloud radius increases to 0.13 mm. This results in the total charge cloud diameter reaching 1/3 of the pixel size (0.88mm). Hence charge sharing will have a significant effect on events containing the full 511 keV energy deposit.

In order to model this behaviour all energy deposits from Geant4 were split into 500 points, spatially distributed according to a Guassian distribution with sigma defined by the root mean sum of Eq. 4.5 and 4.6. At each of the 500 locations sampled from the distribution 1/500 th of the recorded energy was deposited.

4.2.4 Charge Sharing Compensation

The effects of charge sharing are immediately apparent from the laboratory CZT energy spectra. Fig. 4.11 shows all the energies recorded by triggered pixels when a ^{22}Na source was placed

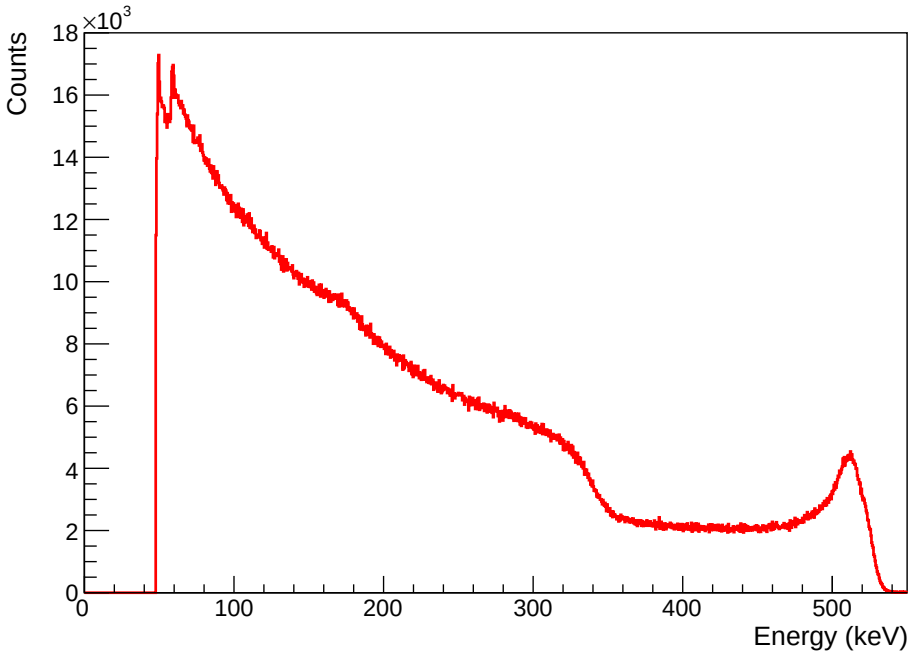

Figure 4.11: Energy spectra of all triggered pixels from CZT laboratory data with a ^{22}Na source.

equidistant between the two detectors. The sharp drop off at 50 keV corresponds to the applied trigger level for a recorded event. The 511 keV photopeak is asymmetric, with a large low energy tail extending towards the Compton edge. These events correspond to charge sharing incidences, where energy has been lost into the neighbouring pixels.

In order to compensate for this effect multiple energy deposits within the same head were grouped into clusters, providing they met certain conditions. Any two adjacent pixels that were both triggered during an event (i.e. recorded an energy greater than or equal to 50 keV) were allocated to the same cluster. Each cluster was defined by the total energy deposited in all its constituent pixels and energy weighted centre of mass. No limit was set on the maximum size of a cluster. Pixels which were only connected along a diagonal were not considered adjacent and hence not amalgamated into a cluster. Fig. 4.12(a) shows the distribution of cluster sizes measured in each detector head. It can be seen that the dominant cluster size in both detector heads contains only 1 pixel, making up 58% and 73% of events in detector heads 0 and 1 respectively. 36% and 23% consisted of 2 pixel events, with the existence of larger clusters decreasing exponentially with size. Significantly more clusters containing just one pixel are detected in detector 1 compared to detector 0. This implies a slower charge carrier drift time for detector 0. The slower the drift time the more the charge cloud disperses before detection at the anode and hence more pixels are triggered. Theoretically the charge distribution should

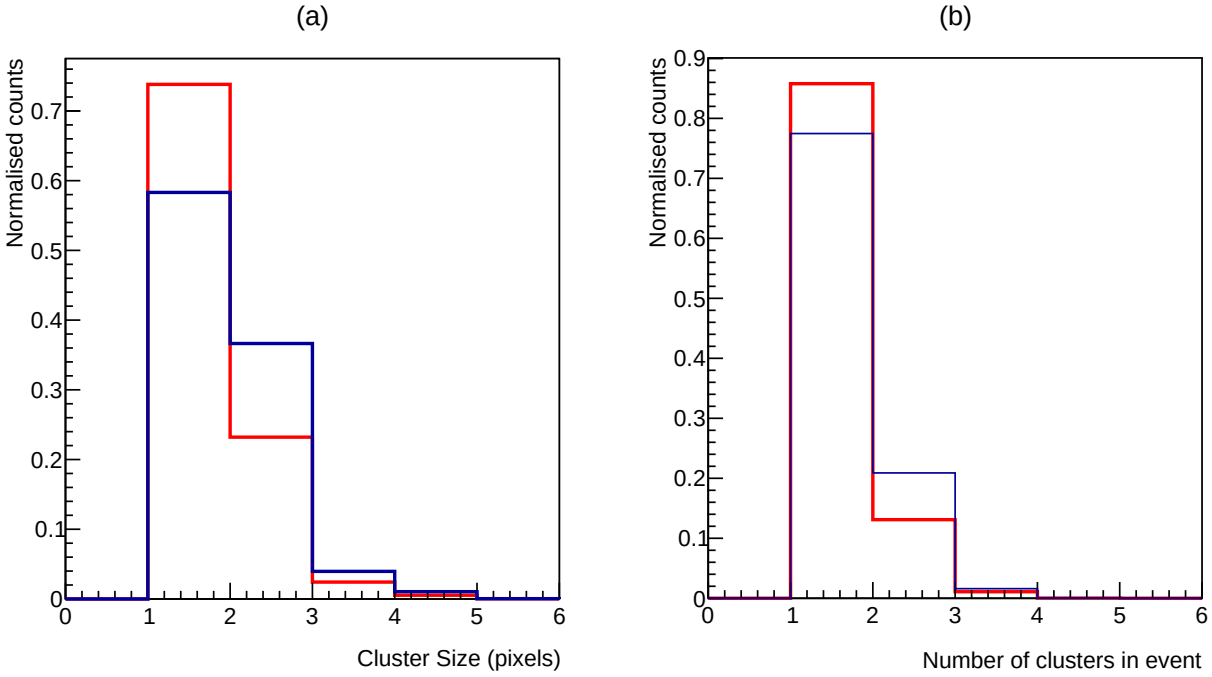

Figure 4.12: (a) Normalised histograms displaying all detected cluster sizes for detector head 0 (blue) and detector head 1 (red). (b) The number of clusters per event for detector head 0 (blue) and detector head 1 (red).

be independent of the mobility of electrons within the crystal. However variability of electrical contacts on CZT detectors can have a significant effect on the electrical field inside the detector itself. Consequently it was necessary to adjust the field strength for each detector head to provide a better match between Geant4 simulation and experimental data.

In order to identify double scattering events, it is necessary to be able to identify with some certainty two separate interactions within the detector. If there were more than two clusters it would be impossible to determine which two were the first and second interactions. A histogram containing the number of clusters detected per head is shown in Fig. 4.12(b). The dominant event type contained just one cluster, making up 77% and 85% of events in detectors 1 and 2 respectively. The useful 2 cluster events made up 13% and 21% of the overall yield.

The detector system employs a trigger threshold, below which energy deposits are not recorded. However, as discussed in the previous section, slow drift times can cause the electron cloud to expand to the point where it is detected over many adjacent pixels. These neighbouring pixels can receive substantial energy deposits, however they may be below the required trigger threshold and not be recorded. This has the effect of degrading the overall energy resolution. To compensate for this, the DMatrix ASIC reads out not only the energy of every triggered

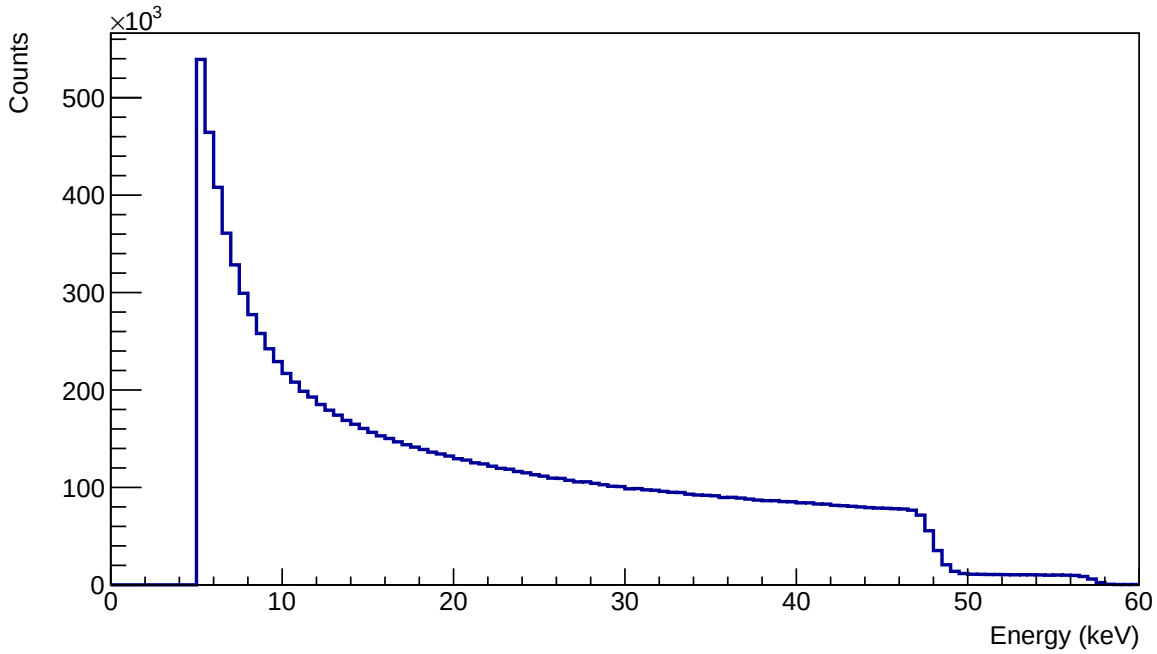

Figure 4.13: Energy distribution of the highest energy deposit in neighbouring untriggered pixels.

pixel, but also the energy deposited in all of its nearest neighbours. The energy distribution of the neighbouring pixel with maximum energy is shown in Fig. 4.13. For each event the single neighbouring pixel whose anode timing most closely matched that of the triggered pixel was incorporated into the cluster. Fig. 4.14(a) shows the energy spectra for all one cluster events. It can be seen that the 511 keV photopeak displays a slight low-energy tail. In Fig. 4.14(b) the same energy spectra has been plotted in red, along with the energy spectra obtained when one compatible untriggered pixel has been incorporated into each cluster. Both spectra are plotted using the same scale. The inclusion of the charge sharing correction results in an increase in the photopeak along with an improvement in the energy resolution at 511 keV from 4.43% to 2.97% FWHM. The analysis was trialled with more than one neighbouring pixel incorporated into each cluster, however this caused the energy resolution to degrade once more.

The importance of this correction becomes even more noticeable when events with two separate clusters are considered. Since each individual cluster can be affected by charge sharing, the total summed energy is impacted twofold. Fig. 4.15 shows the summed energy of two separate clusters with (b) and without (a) a charge sharing correction applied. The inclusion of the charge sharing correction results in the photopeak doubling in height with the energy resolution improving from 11.99% to 4.36% FWHM (at 511 keV).

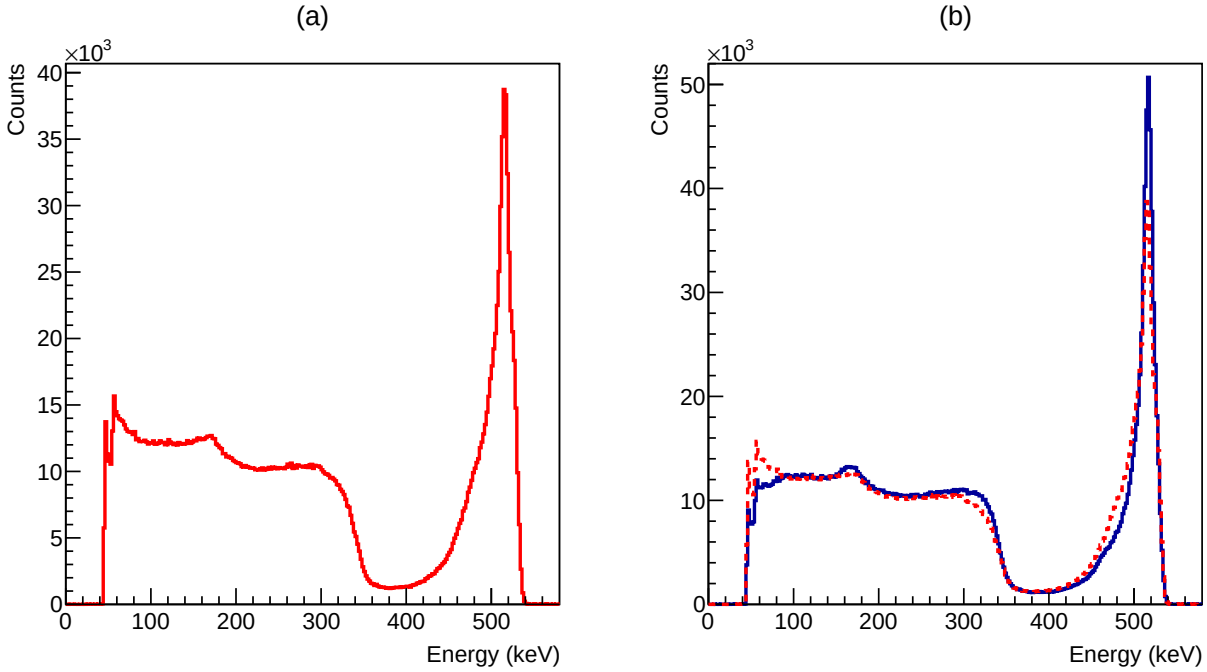

Figure 4.14: Energy spectra of one cluster events. (a) With no charge sharing correction, (b) with charge sharing correction applied in blue and without charge sharing reproduced in red. FWHM improves from 4.43% to 2.97%.

Even with this correction applied, the position of the photopeak shows a dependence on cluster size. The larger the size of the cluster (the more pixels included), the higher the probability of charge loss between pixels. As a consequence the photopeak can be seen to drift to lower energies as more pixels are included in the cluster (a common feature of highly pixelated detectors). It was therefore decided to limit our analysis to clusters containing a maximum of two triggered pixels. A second order correction was then applied to the detector calibration to ensure that the photopeak of one and two pixel clusters were centred at 511 keV.

4.2.5 Data Analysis

Experimental data from ∼780 hrs of measurement was passed through charge sharing correction and clustering algorithms as described above. This data set was compared to simulation data from ∼3 x 10^{12} positron annihilations. Simulation data were passed through precisely the same analysis with the energies and positions smeared to match the detector resolution.

In order to limit data to identifiable double Compton scatterings, events were selected on the basis of having exactly two clusters in both detector heads. To ensure the rejection of charge sharing events, clusters were also required to be separated by a gap of at least one pixel

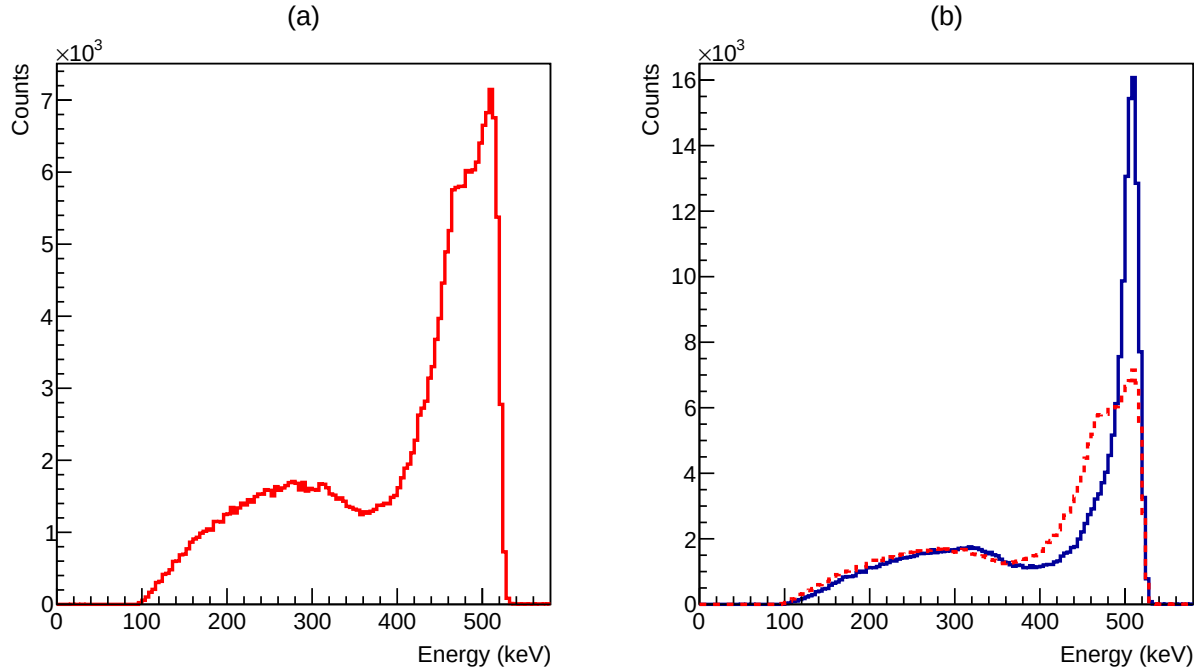

Figure 4.15: Energy spectra of two separate clusters summed together. (a) Without the inclusion of neighbouring untriggered pixels. (b) With charge sharing correction applied in blue and without charge sharing reproduced in red for comparison.

and only clusters consisting of 1 or 2 triggered pixels were considered. Fig. 4.16(a) shows the energy correlations between the first and second pixel clusters. The pronounced diagonal line represents events where the total energy of the two interactions was 511 keV. These are the events of most interest and correspond to DCS events in both heads where both clusters are contained within the CZT. Alongside this yield there are other background contributions evident in the plot. The horizontal and vertical bands at 511 keV correspond to a good event in one of the heads in coincidence with a random event or noise in the other head. The strength below the diagonal line corresponds to events where the 511 keV is not contained in the head (e.g. particles escaping the crystal). In order to reduce any contribution from random or incomplete DCS events, the total deposited energy in each detector head was required to fall between 480-530 keV.

From this subset of the measured data the inter-crystal scattering angles could then be calculated. The polar scattering angle, θ, was determined from the energy deposits using the Compton scattering formula, Eq. 1.1. The largest energy deposit was always assumed to correspond to the first hit. Geant4 simulations suggest that this assumption is accurate 60% of the time. Fortunately any incorrect assignment results in a shift in the calculated scattering

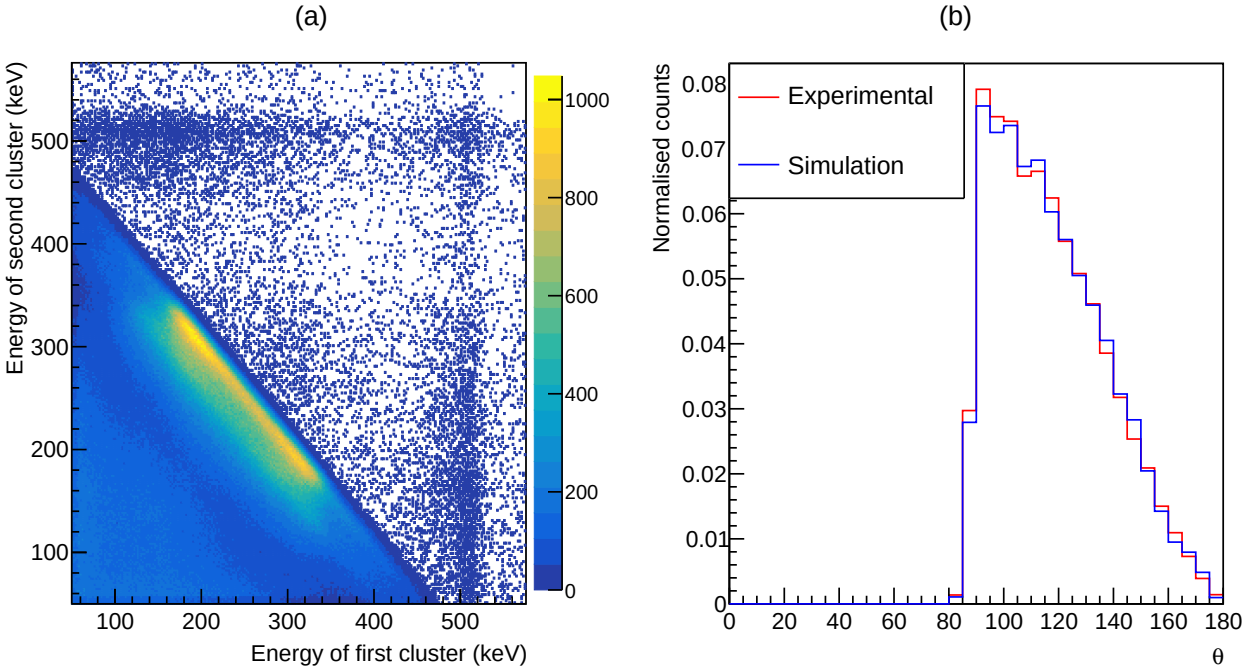

Figure 4.16: (a) Correlation between first and second energy deposits in laboratory data. (b) Comparison of θ values for simulated (blue) and experimental (red) results. Data is cut off at 90° by the assumption that the highest energy was the first interaction.

angle ($\theta_{calc} = 180 - \theta_{real}$), but due to the symmetry around 0° this has no effect on $\Delta\phi$.

The resulting θ distributions from both simulation and laboratory results are shown in Fig. 4.16(b). Due to the Compton scattering kinematics our assumption that the largest energy corresponds to the first interaction forces the theta distribution to contain only events with $\theta = 90°$ and above.

The azimuthal angle, ϕ was calculated from the energy-weighted centre-of-gravity of each cluster. Consequently the angular resolution varied depending on cluster separation,

$$\sigma_\phi = \frac{1}{\sqrt{6}} \mid \frac{a}{d} \mid \tag{4.8}$$

where a is the pixel width and d the separation between cluster centres [Mak20]. The ϕ resolution varied from 2.9° for the most distant clusters, to 20.4° for the closest clusters considered in this analysis.

To enhance the visibility of the entangled correlations, only events with theta in the range $70° \leq \theta \leq 110°$ were analysed. Within this range Eq. 1.7 predicts a larger amplitude for the $\Delta\phi$ correlation. This can be seen from a plot of $\Delta\phi$ against θ, as shown in Fig. 4.17(a). Due to the assumption that the first interaction deposited the higher energy, the θ distribution is

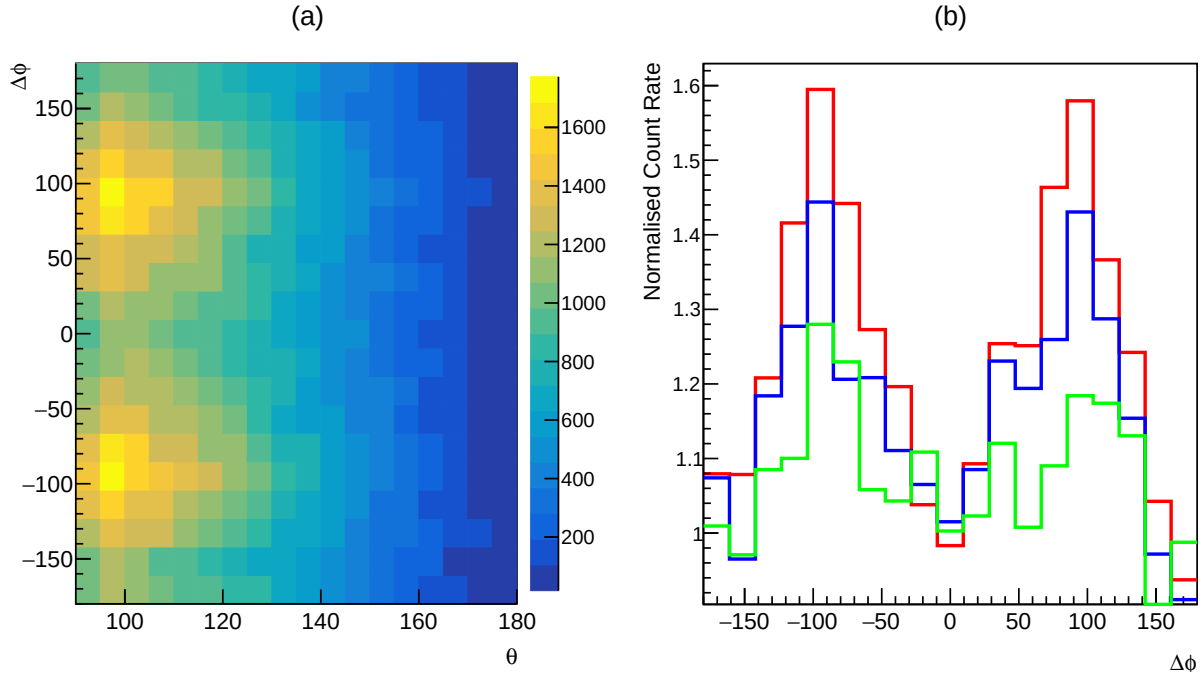

Figure 4.17: (a) Correlation between θ and $\Delta\phi$ scatting angles from experimental data. At angles close to 90° the cosine nature of the $\Delta\phi$ correlations becomes much more apparent. (b) Profiles through (a) for given θ bins. **Red** $95 \leq \theta \leq 100$, **blue** $110 \leq \theta \leq 115$, **green** $125 \leq \theta \leq 130$. Each profile was normalised such that the minima at -180, 0 and 180° lie at 1.

effectively folded about 90°. Consequently the region of maximum enhancement, $\theta = 81.2°$, actually appears at 98.8°. Within this region the amplitude of the $\cos(2\Delta\phi)$ distribution is clearly enhanced. Fig. 4.17(b) shows profiles drawn through the distribution for various θ bins. Each profile is normalised such that the minima of the distribution sits at 1, to allow for better comparison of the overall amplitude.

4.3 CZT Results

The measured normalised coincidence count rate as a function of $\Delta\phi$ for data in the polar angle bin $70° \leq \theta \leq 110°$ is shown by the black data points in Fig. 4.18. The normalisation consists of scaling the minima at $\Delta\phi = 0$ and $\pm 180°$ close to unity. In general, the experimental data shows a clear $\cos(2\Delta\phi)$ distribution. Small deviations from the trend are observed in bins near $\Delta\phi = 0$. There is a slight asymmetry in the yields at $-180°$ and 180° with the latter showing a slightly reduced yield.

The results of the QE-Geant4 simulation have been plotted on the same axis in blue and

show a remarkable agreement with the measured data. The width of the line represents the statistical uncertainty in the simulation. This figure represents the first measurement of its kind showing quantum entanglement in a PET like system, and the strong agreement provides validation of our quantum entangled simulation along with the underlying quantum theory employed.

Additional comparisons were made by running further simulations with non-entangled orthogonally polarised γ (red line). In this case photon trajectories were modelled using the standard Geant4 polarised scattering classes. The underlying $\cos(2\Delta\phi)$ distribution is still clear, but it fails to replicate the full amplitude of the laboratory data. As this represents the maximum enhancement that can be produced from a non-entangled system its inability to describe the data offers a clear entanglement witness.

A further simulation was carried out for unpolarised annihilation γ (green). The generally uniform distribution in delta phi indicates rather modest acceptance effects albeit with an enhancement evident around 20° and a slight asymmetry in yield at $\Delta\phi = 180°$ and 180°. The fact that these effects are also evident in the laboratory data, leads us to believe they are purely a geometrical detector acceptance effect.

A bin-by-bin analysis of the residuals between simulation and experimental data is shown in Fig. 4.19. The non-entangled simulation (red points) show a clear trend, failing to replicate the amplitude of the $\cos(2\Delta\phi)$ distribution, whereas the entangled simulation shows good agreement over all $\Delta\phi$, with residuals evenly distributed around zero. Reduced chi squared values, χ^2_ν, were found to be 42.82 between experimental and Geant4, and 1.87 between experimental and QE-Geant4.

No double Compton scattering measurement has ever directly measured the predicted maximum enhancement ratio (R) of 2.85 [Car19]. All measurements have finite bins of θ and ϕ which act to reduce the maximum observable enhancement. In this geometrical setup a measured enhancement of 1.85 ± 0.04 is achieved. Applying a tighter θ window, $93° \leq \theta_{1,2} \leq 103°$ gave a higher measured enhancement of R=1.95 ± 0.07. Future experiments are planned with longer run times in order to acquire higher statistics. This should allow tighter theta binning to be employed, leading to a greater enhancement, closer to the theoretical upper limit.

The QE-Geant4 simulation is based on the double Compton scattering cross section proposed by Pryce and Ward [PW47]. As such the agreement between the simulation results and experimental data provides direct validation of this theory (and consequently the underlying 2.85 enhancement). The simulation is also the first test of the enhancement ratio to include modelling of effects, such as non-Compton processes, multiple scatterings in the detector simulation and detector acceptance effects, prior works used analytical estimates. The agreement

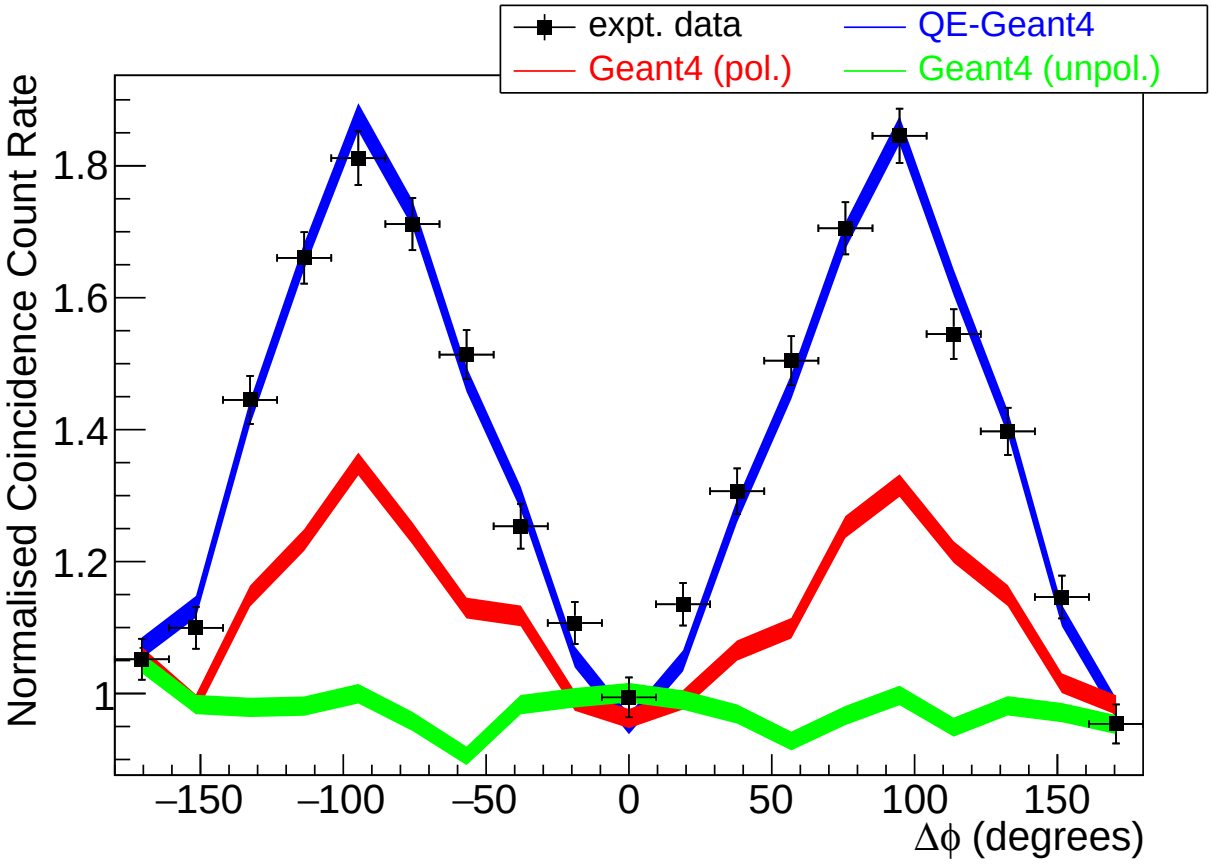

Figure 4.18: The black data points show the experimental coincidence count rate as a function of $\Delta\phi$. The results of the QE-Geant4 simulation are shown as a blue line. The non-entangled orthogonally polarised simulation photons are in red and unpolarised independent photons are in green. All results have been normalised to unity using the data around the minima at $\pm 180°$ and $0°$. The width of the lines represents the statistical uncertainty in the simulation. All events were analysed for the polar scattering range $70° \leq \theta \leq 110°$.

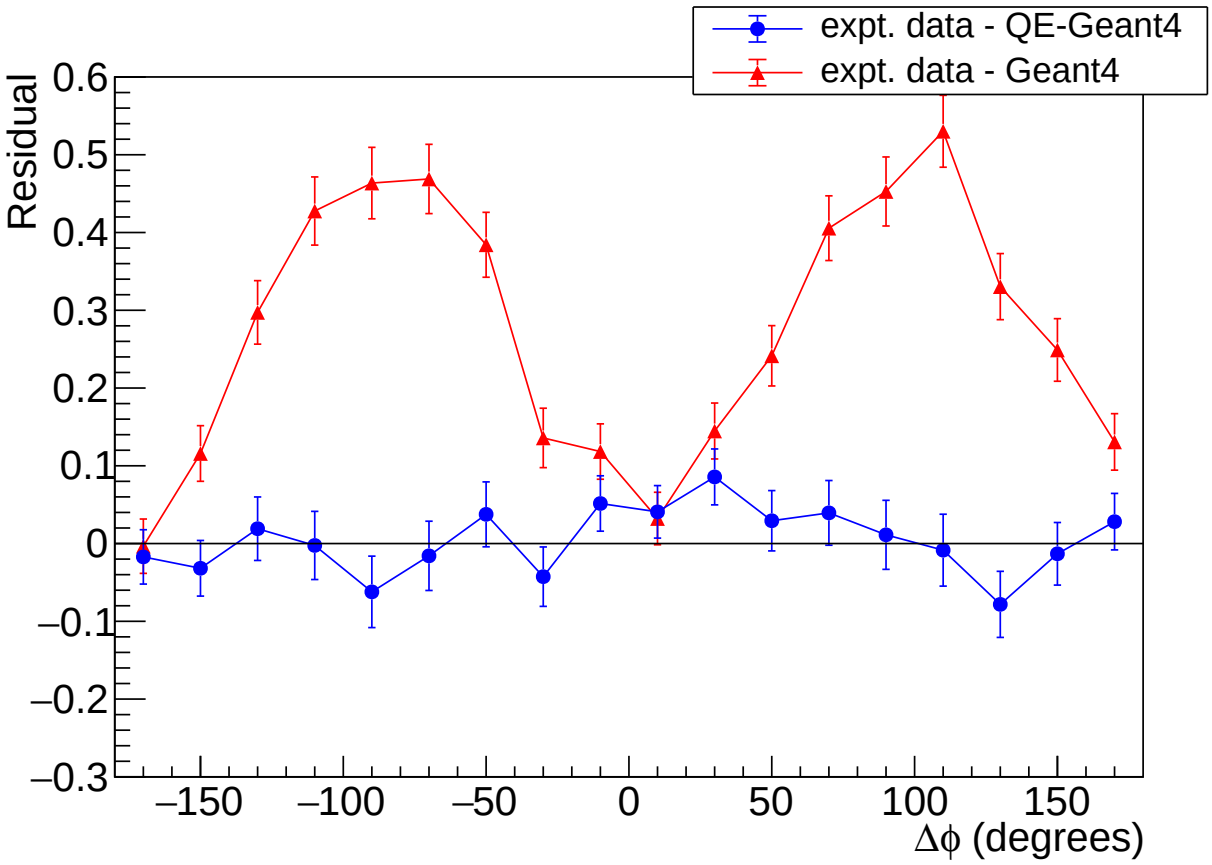

Figure 4.19: Residual plot comparing experimental data with simulation. Bin-by-bin residuals are shown for experimental data with both QE-Geant4 prediction (blue) and orthogonally polarised prediction (red). Error bars represent the RMS of the statistical error of the experimental data and simulation.

therefore provides a significant step forward in accuracy of experimental tests of entanglement theory.

4.4 Entanglement Loss

Thus far we have relied on the assumption that when either γ undergoes a decohering process (such as Compton scatter) the entangled wavefunction collapses fully, with subsequent interactions proceeding as for independent photons. This is reflected in our QE-Geant4 simulation in which the simulation reverts from the quantum entangled double Compton cross section routine back to the standard polarised Klein-Nishina routines once one of the γ undergoes an interaction. This is an assumption as there have been no prior measurements of entanglement loss in the MeV energy regime.

To test this assumption we made the first ever measurement of $\Delta\phi$ correlations between annihilation photons that had previously undergone a decohering process (Compton scatter). The previous setup was modified to create a data set consisting of purely scattered events. The two detector heads were placed 60 mm away from the source, with one head rotated through an angle of 33°. A block of nylon (dimensions 7 x 20 x 20 mm) was then placed directly in front of the source to act as a scattering medium. A rendering of the setup is shown in Fig. 4.20.

Events were recorded when two clusters, each one or two pixels in size, were detected in coincidence in each detector head. In order to isolate events scattered inside the nylon from purely random coincidences a shifted energy window was applied to the photons detected in the rotated detector. Events were retained if the total deposited energy between the two clusters was in the range 370 - 470 keV in the rotated head, and 480 - 540 keV in the direct head. A larger θ window of $60° \leq \theta \leq 140°$ was also applied in order to account for the low statistics. The achievable stopping power of CZT combined with the finite angular range covered by the detectors makes this particular interaction very rare. In addition, to avoid pile-up of events in the CZT heads a relatively weak source was required. Consequently, the data presented in Fig. 4.21 represents over a month of data acquisition.

4.4.1 CZT entanglement loss results

The measured normalised coincidence count rate for this scattered experiment is shown by the black data points in Fig. 4.21. Once more the distribution has been scaled to make the minima at $\Delta\phi = 0$ and $\pm 180°$ close to unity. Within the achievable statistical accuracy there

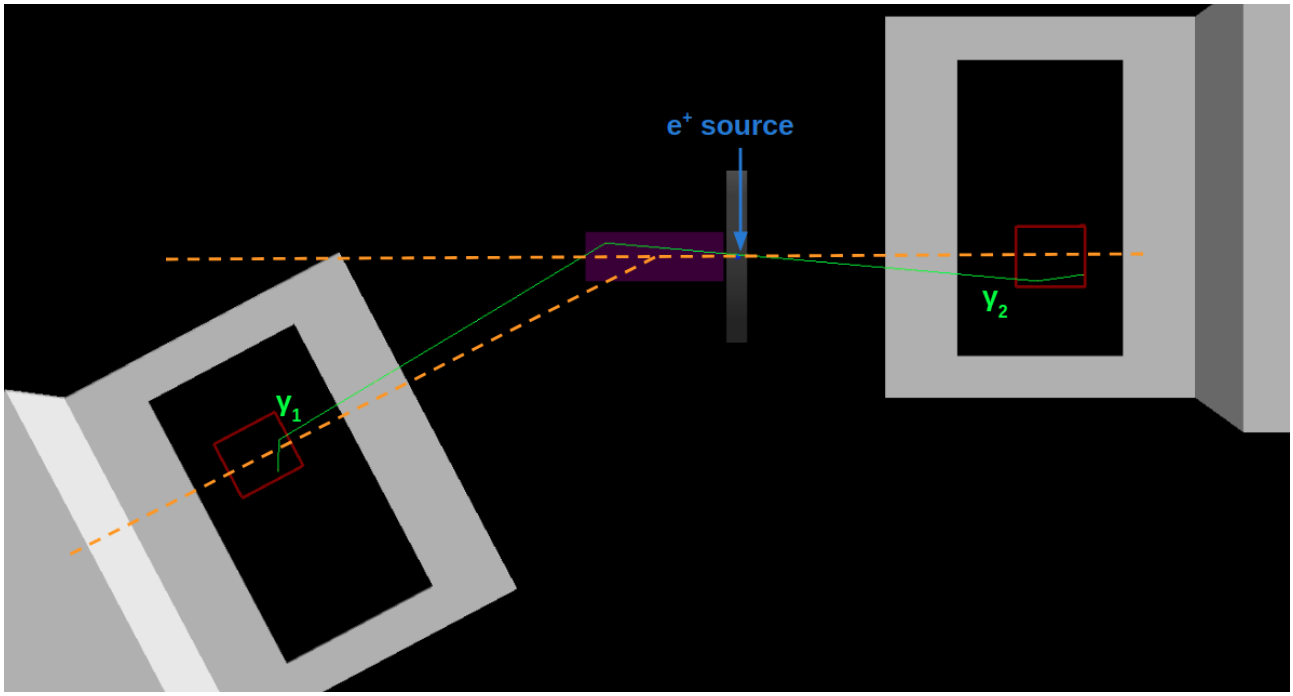

Figure 4.20: A Geant4 rendering of the scatter setup. The two CZT crystals are shown by the red boxes and their supporting structures in grey. The trajectory of the two γ is shown by the green line. They originate at the source and travel in back-to-back directions. One γ scatters in the nylon scatterer (purple) prior to its detection in the CZT crystal. Both γ proceed to Compton scatter inside the CZT crystals, this can be seen from the kinks in the trajectory. $\Delta\phi$ for the event is calculated from the scatters inside the CZT crystals.

is no discernible $\cos(2\Delta\phi)$ correlation remaining in the data. For comparison the results of the QE-Geant4 simulation for the same scattered setup have been plotted on the same axis in blue. They also exhibit a diminished $\Delta\phi$ correlation, in statistical agreement with our experimental data. The width of the line represents the statistical uncertainty in the simulation.

For comparison, the QE-Geant4 results and the experimental results for the case of back-to-back entangled γ have been included (red line and data points). This is the same data as displayed in Fig. 4.18 with the θ windows adjusted to match those of the scattered data ($60° \leq \theta \leq 140°$). It should be noted that the use of a wider theta window reduces the amplitude compared to Fig 4.18.

The measured $\Delta\phi$ correlation of the scattered data is clearly reduced compared to that of the unscattered events. This gives confidence in our simulation approach and allows for the possibility to utilise these differences in correlation in the context of PET imaging, see Chapter 5. There is further discussion of $\Delta\phi$ correlations between previously scattered γ in Chapter 6, where a second measurement is presented using a different detector array.

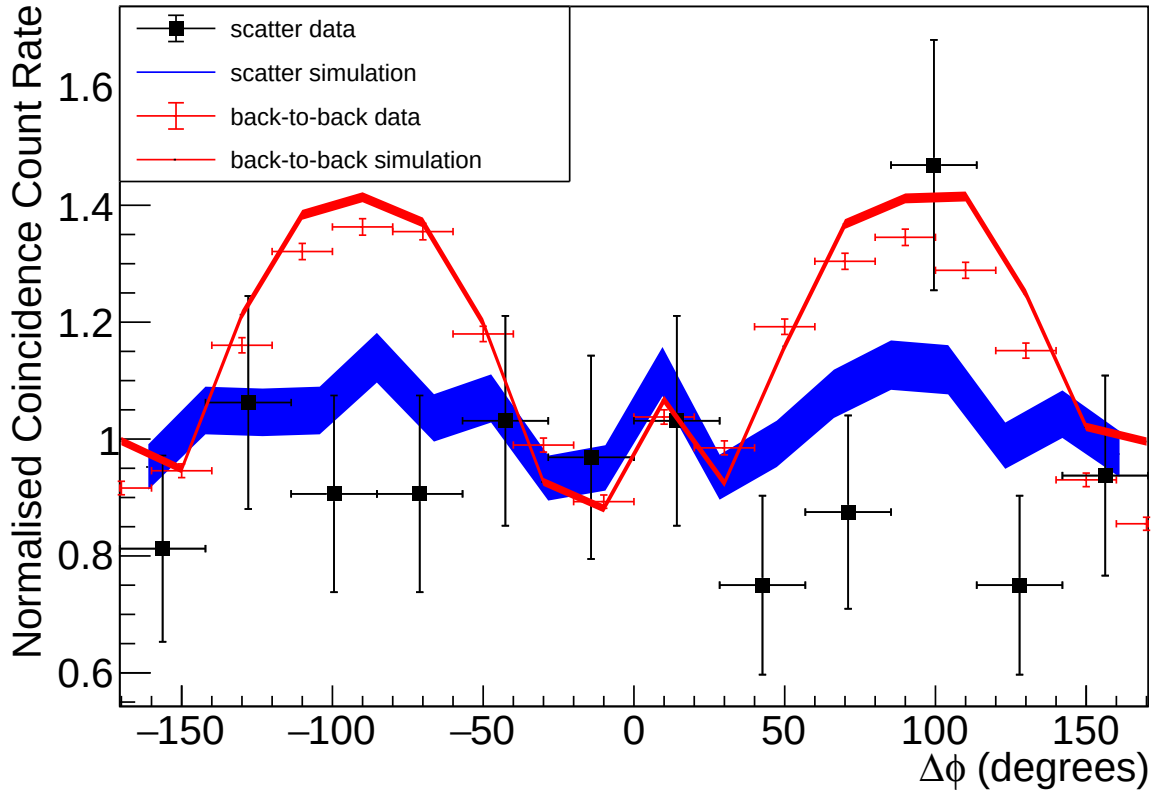

Figure 4.21: The black data points show the experimental normalised coincident count rate as a function of $\Delta\phi$, obtained from the setup shown in Fig. 4.20. One γ in each event had undergone a Compton scatter through $\theta \sim 33°$ prior to detection. The vertical error bars represent the statistical error in the number of counts and the horizontal error bars represent the bin width. QE-Geant4 results from the same experiment have been plotted in blue. The standard deviation is represented by the line width. For comparison, the experimental $\Delta\phi$ distribution measured in a back-to-back configuration (without the scatterer) has been plotted in red. The red band shows QE-Geant4 results for the back-to-back configuration. All experimental results and simulations employ a θ cut of $60° \leq \theta \leq 140°$.

Chapter 5

Image Reconstruction

In Chapter 4 it was demonstrated that CZT detectors have the capability to identify entanglement information through the scattering correlations of annihilation PET γ. The next step in our investigation was to determine whether or not this information could be utilised to improve image quality. Specifically, we aimed to exploit the different $\Delta\phi$ dependencies to distinguish scattered and random events from the underlying true events. The results presented in this Chapter were derived from my work in collaboration with Dr Julien Bordes and Dr Jamie Brown.

Theoretically, the behaviour of true PET events should be well defined by our QE-Geant4 simulation. Upon detection in the scanner both PET γ should still be entangled with one another and their relative scattering angles should exhibit an enhanced $\Delta\phi$ correlation, as demonstrated by the blue curve in Fig. 4.18. If we consider instead the case of a random coincidence, the γ are completely independent and as such the overall $\Delta\phi$ distribution should show no correlation, with all $\Delta\phi$ angles observed with equal frequency. In the final case of scattered events, there may be some residual $\Delta\phi$ correlation, but as demonstrated by the experiments in Chapter 4, this will have a reduced amplitude. Due to the statistical nature of these effects, it is impossible to determine with any certainty which particular event type a γ pair might belong to. However, we can use the $\Delta\phi$ information to assign a γ pair to a particular event with a certain probability.

5.1 Building a simulated CZT PET detector

To explore this idea further, the CZT QE-Geant4 simulation described in Chapter 4 was extended to model a complete PET scanner. The scanner consisted of 4 rings of CZT crystals with dimensions equal to those in our lab (8.8 x 8.8 x 10 mm). This resulted in a scanner

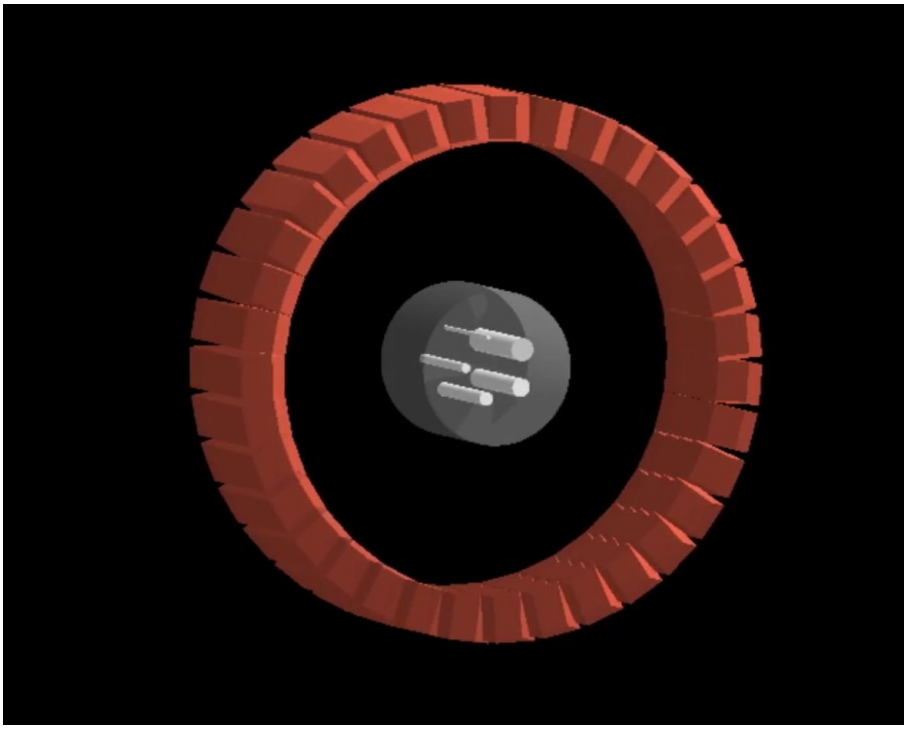

Figure 5.1: Geant4 rendering of CZT scanner geometry with NEMA-NU4 phantom placed along z-axis. **Red** represents CZT crystals. **Grey** tissue equivalent PMMA and **white** cylinders containing a mixture of water and e^+ source.

radius of 49.1 mm and an axial length of 35.2 mm. These dimensions are roughly comparable to those of common small animal PET scanners.

A phantom was placed inside the scanner. Phantoms are objects designed to mimic the attenuation of real patients and hence model γ attenuation and scattering. In this case the phantom selected was the NEMA-NU4 (National Electric Manufacturers Association) [NEM08] preclinical mouse phantom. It is composed of a cylinder of tissue equivalent poly(methyl methacrylate)(PMMA) along with 5 capillaries (1-5 mm in diameter) each of which are filled with a combination of water and e^+ source. The phantom measured 20 mm in length and 33.5 mm in radius. A Geant4 rendering of the scanner and phantom geometry is shown in Fig. 5.1.

5.2 Data processing and Image reconstruction

PET events were recorded when both annihilation γ underwent two separate interactions within the detector. Since the source annihilates isotropically the scanner geometry only covers a small field of view, hence limiting the number of annihilation events which are recorded. In addition the 1 cm depth of the CZT crystals does not stop all photons, resulting in only a fraction of

these annihilations being detected. As a consequence, only 2.6% of positron annihilations result in both γ depositing energy within the scanner (a normal PET coincidence). Constraining this to double scattered events where the first and second energy deposits were not within the same pixel, this fraction reduces to 1.38%.

The hit positions of each interaction were recorded and smeared with a Gaussian distribution ($\sigma = 0.8/\sqrt{12}$mm) in order to mimic the position resolution of our CZT pixels. Lines of response (LOR) were then drawn between the interaction positions of the first hits for each event pair.

In order to reconstruct PET images from the simulated events the GAMOS (Geant4-based Architecture for Medicine-Oriented Simulations) [Arc14] software package was employed. Events were binned into sinograms using the "lm2pd" functionality. From these, images were reconstructed using the single-slice rebinning filtered back projection (SSRB-FBP2d) algorithm with a ramp filter applied. The pixel size was set to 0.6 x 0.6 mm and images were processed using the ImageJ NucMed plugin [SRE12]. Fig. 5.2(a) shows an image reconstructed from only true lines of response. The 5 bright circles in the center show the source capillaries. The only artefacts in the image are the streaks originating from the reconstruction algorithm and are a known effect for FBP imaging methodologies. Fig. 5.2(b) was reconstructed using all the detected lines of response, including the fraction of the yield where one or both of the photons scattered in the phantom before detection. These events can be seen to cause some blurring of the capillaries and form a background to the image. As expected for a small animal phantom the scatter contributions are small - but such a setup is a good test for any new development aiming to establish scatter contributions in PET.

5.3 Quantum entangled PET studies

In the following two sections we present initial studies to explore the $\Delta\phi$ dependence of reconstructed PET images, for the case of scatter (Section 5.3.1) and random (Section 5.3.2) backgrounds. Following this we present a new analysis scheme (Section 5.3.3) to process PET images using the quantum entanglement information contained in double Compton scattered events.

5.3.1 Influence of $\Delta\phi$ selection to the PET image with scatter backgrounds

In order to utilise the $\Delta\phi$ correlations, our data set was first optimised by applying a θ cut to retain only events with $67° \leq \theta \leq 97°$. This was done to select the region in which the

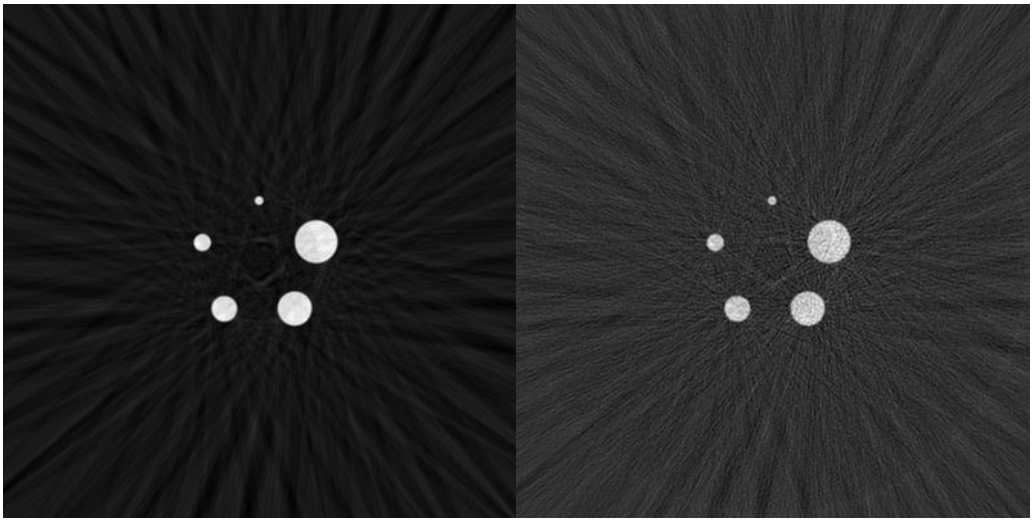

Figure 5.2: Images reconstructed from 114 million simulated LOR. (a) only true LOR are included. (b) True, scatter and random coincidences are included. The data set was artificially modified to create a random fraction of 90%.

enhancement due to entanglement is most prominent. The resulting $\Delta\phi$ distribution for the collected true and scattered events is shown in Fig. 5.3. As expected there is a clear $\cos(2\Delta\phi)$ evident in the simulated data. Due to the relatively small amount of material in the phantom these data correspond to a low scatter scenario for PET. Of the γ arriving at the detector only 21% had previously undergone at least one scatter inside the phantom. As discussed in Chapter 3, this fraction is significantly lower than the case of human PET, with scatter fractions of current systems around ∼44% [Hos17] and larger fractions expected in next generation whole body PET systems. For a larger or denser medium (e.g a human phantom) the increased scatter fractions would lead to greater suppression of the amplitude of the $\cos(2\Delta\phi)$. However, this small animal study allows new methods to be investigated where the scatter fraction is smaller and more challenging to study.

The remaining LOR were then binned into separate sinograms according to the $\Delta\phi$ angle of the event. This enabled separate images to be reconstructed for different $\Delta\phi$ bins. These reconstructions are shown for $\Delta\phi \sim 10°$ and $\Delta\phi \sim 90°$ in Fig. 5.4. Image quality is highly dependent on the number of LORs that are collected, improving as the number of LORs increases. To remove any bias these sinograms were all filled with the same number of LORs (1,200,000). Hence, any variation in image quality is solely a consequence of varying $\Delta\phi$.

True events (those with an LOR passing directly through the source) are statistically more likely to scatter with $\Delta\phi \sim 90°$. However, events that have undergone a scatter prior to

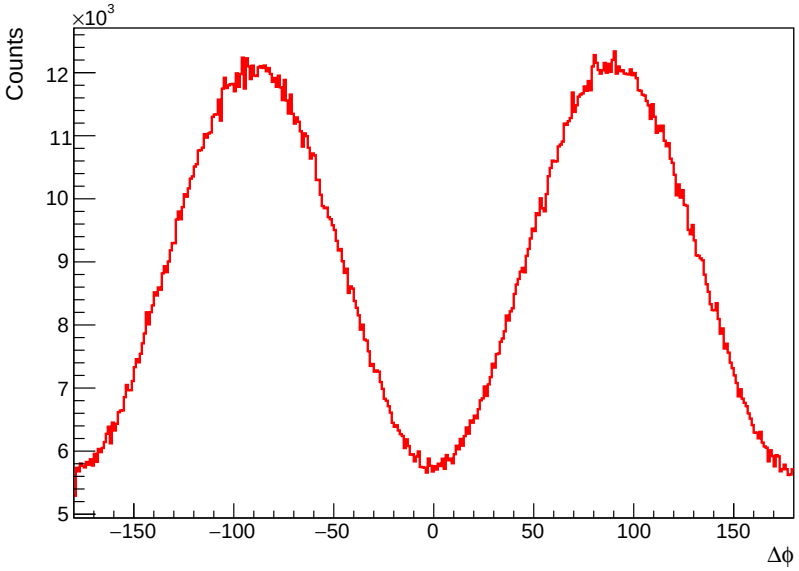

Figure 5.3: The $\Delta\phi$ distribution extracted from simulated PET LOR. A θ cut of $69° \leq \theta \leq 97°$ has been applied to select the region of greatest enhancement due to entanglement.

detection should show strongly diminished $\Delta\phi$ dependency in their scattering angle. These scattered events no longer have an LOR passing through the true annihilation point, and generally contribute noise to the image. As such, by limiting our reconstruction to only events with $\Delta\phi \sim 90°$ the fraction of trues included in the image should increase. Since these results arise from simulation, this can be confirmed by analysing the scatter fraction (SF) accepted into each sinogram. The SF for 9 images reconstructed from varying $\Delta\phi$ bins is shown in the top panel of Fig. 5.5(a). As the $\Delta\phi$ bin increases/decreases away from 90° a higher fraction of scattered LORs are included. Theoretically incorporating a higher fraction of scattered LORs should also correspond to an reduction in the image quality. However, in this case the overall scatter fraction is very low and there is little variation in SF between the images. Consequently there is no visual improvement between the two reconstructions in Fig. 5.4, or in the contrast-to-noise ratio (calculated for each image in the lower panel of Fig. 5.5(a)).

A second set of sinograms were produced from the same data set. This time the scatter fraction was artificially increased by only accepting a limited number of true LORs. This resulted in a data set with an overall scatter fraction of 49% (equivalent to many 3D chest scans [WNC96]). For each image reconstruction, the included SF and the CNR are plotted in Fig. 5.5(b). This time the CNR shows a clear trend, improving from 9.3, when reconstructed with LORs $0° \leq \Delta\phi \leq 20°$, up to 12.6 for LORs $80° \leq \Delta\phi \leq 100°$. This demonstrates that purely through applying θ and $\Delta\phi$ windows, LORs can be separated into those more and less

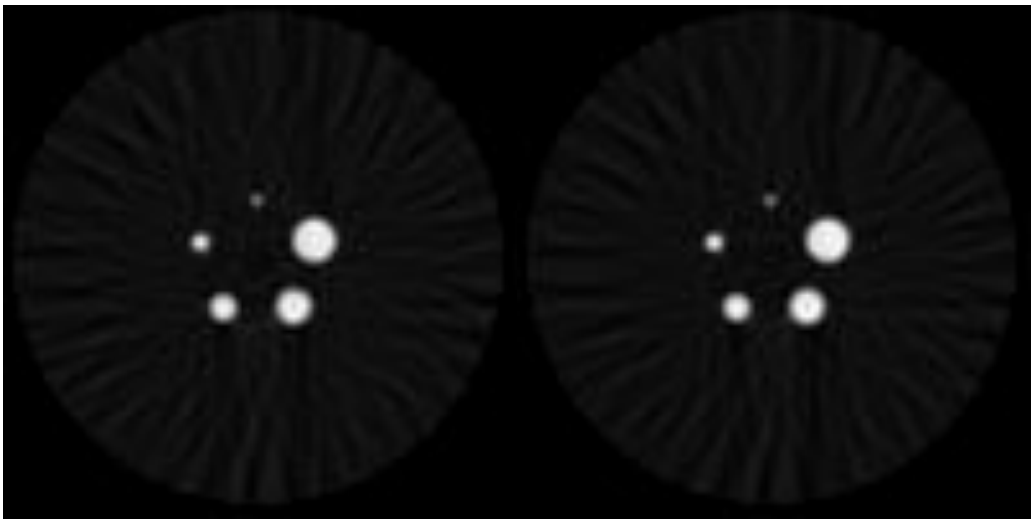

Figure 5.4: Cross-section images reconstructed using only true and scattered LORs with $0° \leq \Delta\phi \leq 20°$ (left) and using only LORs in range $80° \leq \Delta\phi \leq 100°$ (right).

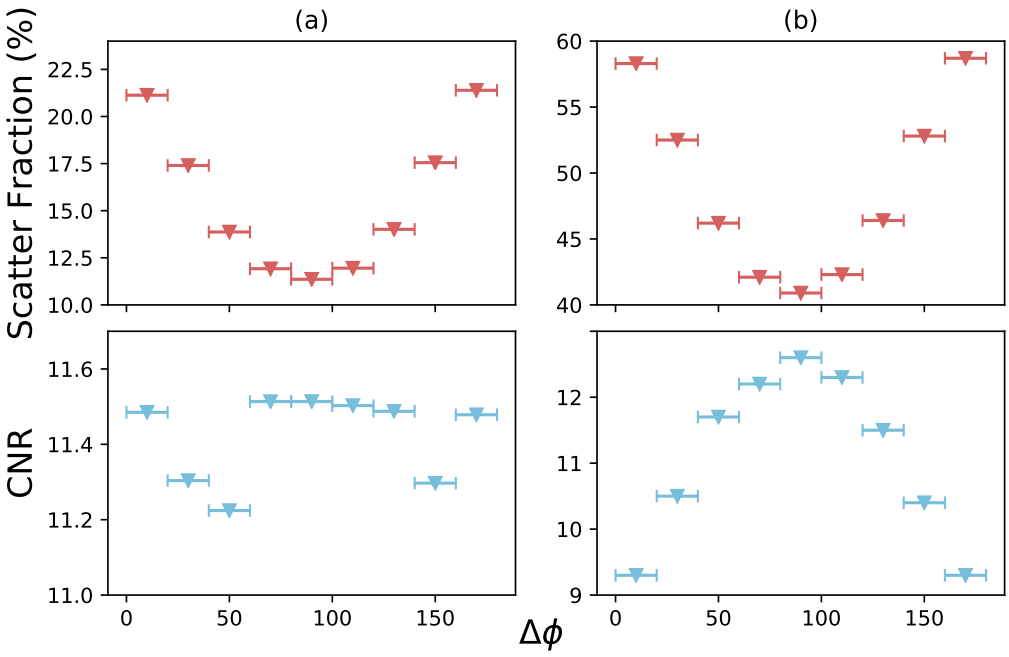

Figure 5.5: (a) The variation of random fraction (top) and contrast-to-noise ratio (bottom) with $\Delta\phi$ window, for a data set containing 21% scattered events. (b) The variation of RF and CNR with $\Delta\phi$ window obtained from a data set containing 49% scattered events.

likely to correspond to true events.

5.3.2 Influence of $\Delta\phi$ selection to the PET image with random backgrounds

A similar method was used to demonstrate the case of random coincidences. Scattered events were entirely removed from the simulation by selecting only event pairs corresponding to "true" PET events. Since the simulation itself did not contain random coincidences we then performed "event mixing", by randomly pairing interaction information from photons originating from different annihilations. This was done to create an artificial data set with a 95% random background. This is very high compared to clinical PET (in which scintillation detectors are employed which have a high time resolution), but is closer to that expected with the large coincidence timing windows required for semiconductor γ detectors such as CZT.

Once more a θ cut ($67° \leq \theta \leq 97°$) was applied and the event LORs binned into sinograms for different $\Delta\phi$. These sinograms were then reconstructed into cross-sectional images, two of which which are shown in Fig. 5.6. This time, due to the high random fraction, the improvement in image quality is immediately noticeable between the two. The background signal arising outside the source capillaries is significantly lower for the image reconstructed with LORs in the range $80° \leq \Delta\phi \leq 100°$. The smallest capillary is also much more clearly defined.

To quantify these improvements the random fraction and CNR for each $\Delta\phi$ bin were calculated and are shown in Fig. 5.7. The closer $\Delta\phi$ approaches to 90° the smaller the fraction of random LORs incorporated and the higher the CNR.

5.4 An image processing scheme for isolating scatter, random and true events in entangled PET

In the previous section we demonstrated the capability of $\Delta\phi$ information to separate events into more and less favourable LORs. This is an exciting result, but clearly not beneficial by itself. Of the original annihilation gamma pairs only 2.6% both hit the detector and registered as standard PET events. Of these 53% could be reliably identified as double scattering events (events containing both a Compton scatter and subsequent detection in both detectors). For this pilot study we select regions of $67° \leq \theta \leq 97°$ where the effects of quantum entanglement to the yield is enhanced. This cut restricts the size of the data sample by a factor of 4. Clearly,

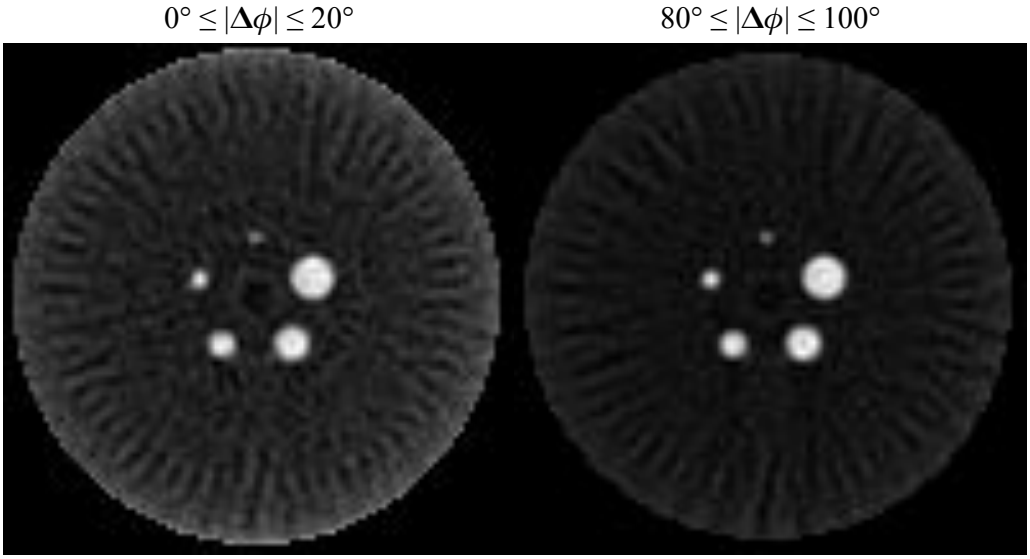

Figure 5.6: Cross-sectional images reconstructed using only true and random LORs with $0° \leq \Delta\phi \leq 20°$ (left) and using only LORs in range $95° \leq \Delta\phi \leq 100°$ (right). An artificial background of ∼80% random LORs was incorporated.

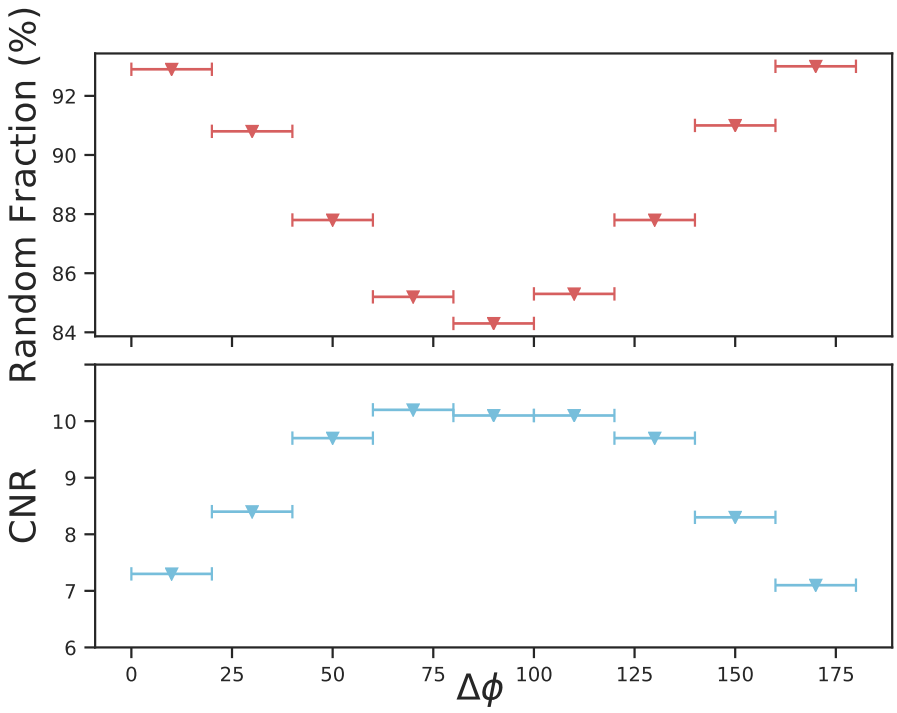

Figure 5.7: Variation of random fraction and contrast-to-noise ratio with $\Delta\phi$ window, for a data set containing purely true and random coincidences.

future work can optimise the balance between yield and enhancement in the data sample.

As an alternative approach, we instead try to isolate the background distributions using simple image subtractions. Rather than applying restrictive cuts to optimise the number of true LORs we instead attempt to model the impact the false LORs have to the reconstructed image. By extracting the contribution of both random and scatter events to a given image reconstruction we can subtract out their effect.

To demonstrate this, a data set was created consisting of 10^{12} annihilation events, which is representative of a typical clinical PET scan (using a source with an activity of several hundred MBq for an acquisition time of 30 min). The total $\Delta\phi$ distribution, P($\Delta\phi$), was considered as the sum of two separate $\Delta\phi$ distributions, arising from the true and the scattered coincidences, $P(\Delta\phi) = T(\Delta\phi) + S(\Delta\phi)$. These distributions were each modelled by a $\cos(2\Delta\phi)$ function centered around a mean value ($\bar{T}$ or $\bar{S}$) with an amplitude (t_{90} or s_{90}). This has been illustrated in Fig 5.8. For a particular range of $\Delta\phi$ we consider the total counts to be a linear sum of the mean of the scattered events, $\bar{S}$ and true events, $\bar{T}$ weighted by their relevant amplitudes. For example, the total counts at $\Delta\phi = 90°$ and $0°$ could be modelled as,

$$P_{90} = t_{90} \cdot \bar{T} + s_{90} \cdot \bar{S} \text{ and } P_0 = t_0 \cdot \bar{T} + s_0 \cdot \bar{S} \tag{5.1}$$

where $t_x = T(x)/\bar{T}$, and $s_x = S(x)/\bar{S}$. Consequently t_{90} represents the amplitude enhancement due to true, entangled events. The s_{90} component accounts for small (residual) $\Delta\phi$ dependencies arising from the remaining correlations of the polarisation planes of the two photons after a scatter. If we combine and rearrange these two equations then the mean scatter contribution can be expressed as,

$$\bar{S} = \frac{t_{90} \cdot P_0 - t_0 \cdot P_{90}}{t_{90} \cdot s_0 - s_{90} \cdot t_0}. \tag{5.2}$$

The values t_{90}, t_0, s_{90} and s_0 were extracted from simulated QE-Geant4 events collected from a different slice of the phantom. This was done by separating true and scattered events and applying fits to both the resulting $\Delta\phi$ distributions. The amplitudes of these fits corresponded to t_{90}, t_0, s_{90} and s_0.

Using the same methodology a similar formalism could be found for random backgrounds. The total $\Delta\phi$ distribution was instead modelled as the sum of a two independent distributions arising from true and random events, $P(\Delta\phi) = T(\Delta\phi)+R(\Delta\phi)$. The mean random contribution could then be expressed as,

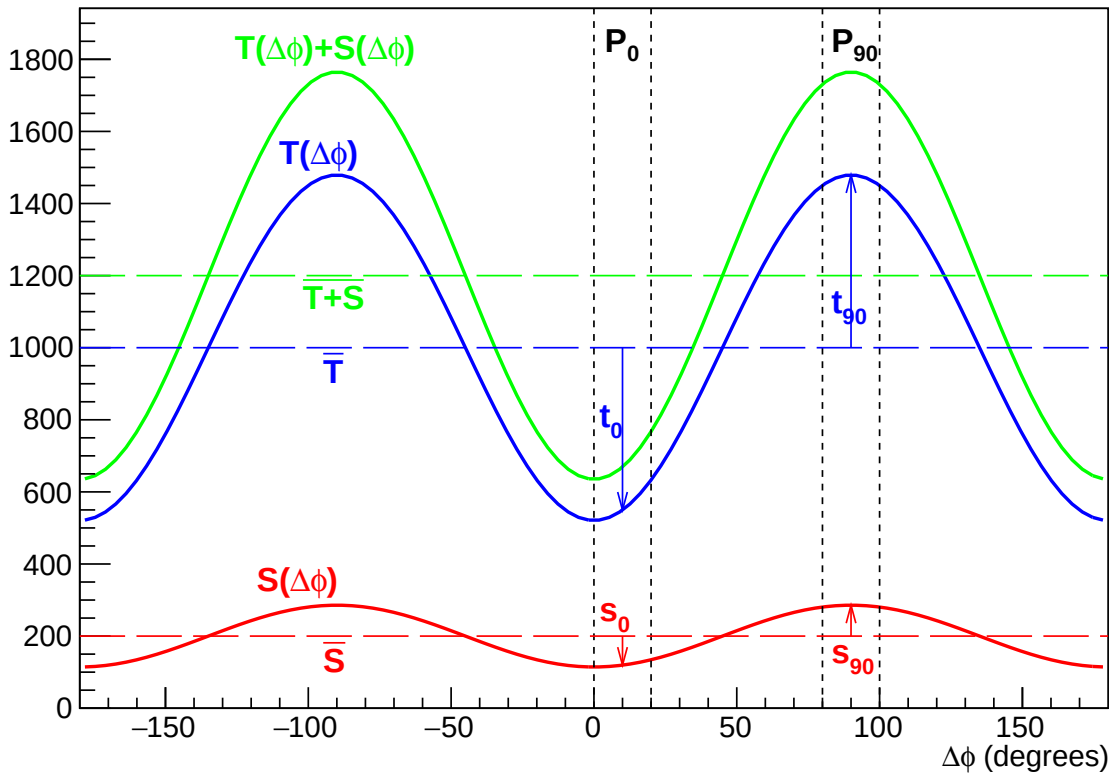

Figure 5.8: A schematic showing the relative contributions of different event types to the overall $\Delta\phi$ distribution. The total yield of all events is shown by the green curve. The blue curve represents the contribution from true coincidences, and the red curve represents the contribution from a hypothetical fraction of random coincidences. The relative fractions and amplitude of the $\cos(2\Delta\phi)$ distribution has been exaggerated for illustrative purposes. As such the y-axis is arbitrary.

$$\bar{R} = \frac{t_{90} \cdot P_0 - t_0 \cdot P_{90}}{t_{90} \cdot r_0 - r_{90} \cdot t_0}. \tag{5.3}$$

although in this case random coincidences display no $\Delta\phi$ correlations, therefore $r_0 = r_{90} = 1$.

To trial this approach, images were once more reconstructed using a standard filter back-projection algorithm (FBP). Images were constructed with purely scatter or random backgrounds and are shown in Fig. 5.9(a) and Fig. 5.10(a) respectively. The same θ cut was applied retaining only coincidences with both polar scattering angles in the range $67° \leq \theta \leq 97°$ to maintain a high enhancement ratio. These reconstructed images clearly show activity originating from the 5 hot capillaries, demonstrating the structure of the phantom.

Intensity profiles were extracted from a region of interest across the two lowest capillaries (shown by the yellow box in Fig. 5.9(a)). These profiles were extracted from two separate images, one created using only LORs with $80° \leq \Delta\phi \leq 100°$, and hence a high fraction of true events, and one with LORs in the range $0° \leq \Delta\phi \leq 20°$, containing a lower fraction of true events. These profiles are plotted in 5.9(b) and 5.10(b) for scatter and random backgrounds respectively.

For the case of a scatter background (Fig. 5.9) there is a clear discrepancy in the height of the peaks between the two profiles. This reflects the fact that true events, originating from the source region, show more favourable $\Delta\phi$. A subtraction of these two profiles is performed in accordance with Eq. 5.2, weighted by factors obtained from QE-Geant4 simulations. The resulting profile is shown in Fig. 5.9(c). This profile represents the contribution scattered events have made to the image segment. For comparisons sake, a second image was reconstructed from only known scattered events (extracted directly from Geant4). A scatter flag was added to the simulation such that scattered events could be identified and isolated. An identical profile through this "actual" scattered image is shown by the blue line in Fig. 5.9(c).

There is good agreement between the two, however the extracted scatter profile (red) exhibits large fluctuations. These are artefacts originating from the unsophisticated FBP reconstruction algorithm. A 4^{th} order polynomial has been added to allow the average trend to be compared to the "actual" scatter distribution. The two are clearly in excellent agreement, with the shape and magnitude of the "true" scatter background well modelled.

The same method was used to extract the contribution of true LORs to the extracted segment. A weighted subtraction of the two profiles in Fig. 5.9(b) was performed and the extracted "true" profile is shown in Fig.5.9(d). This is compared directly to a profile through an image reconstructed solely using true events (red line). There is clearly excellent agreement between the extracted true and the "real" true profile.

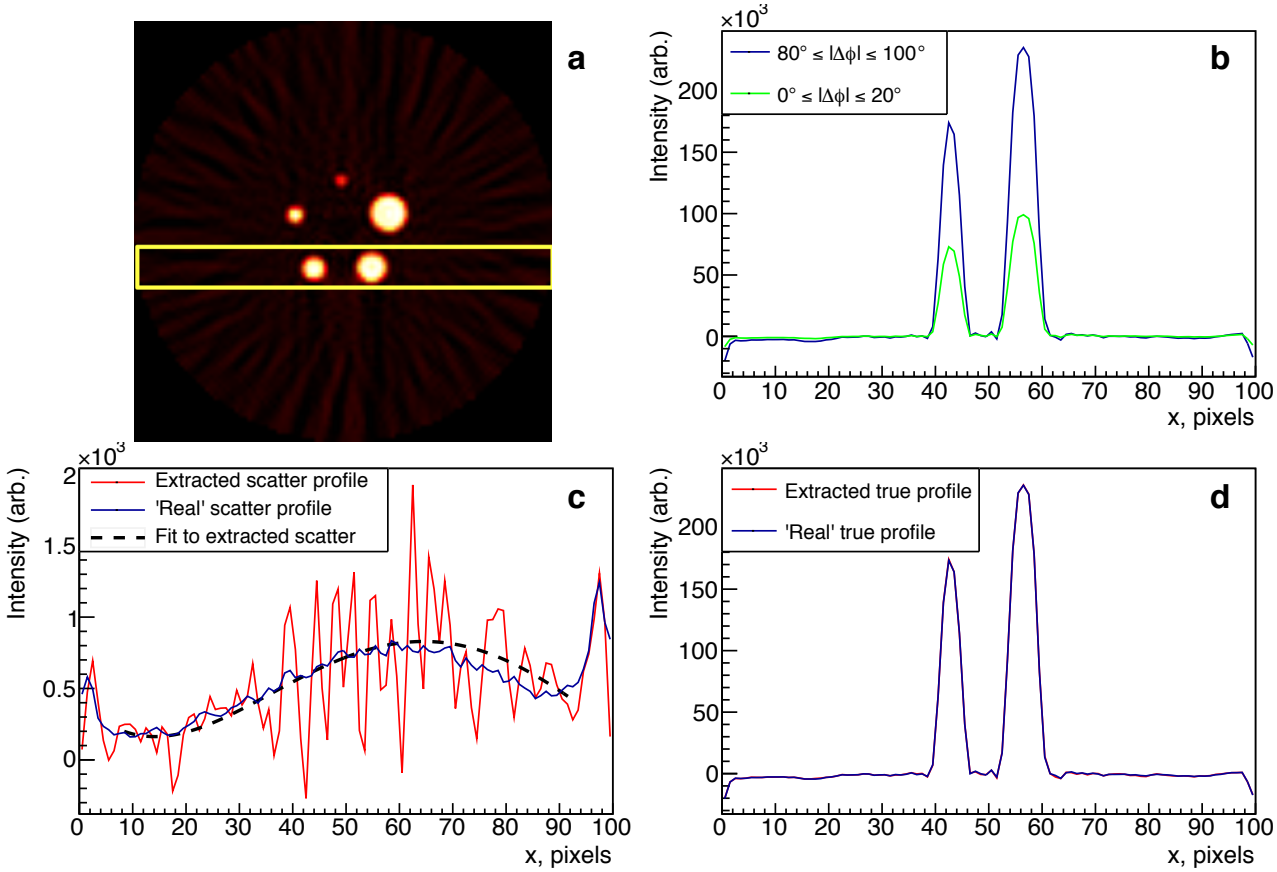

Figure 5.9: (a) A FBP 2-D PET image of the NEMA-NU4 phantom containing true and scattered events. (b) Cross-sections through the bottom two capillaries, taken from images reconstructed with different $\Delta\phi$ cuts. (c) A weighted subtraction of the two profiles in (b) according to Eq. 5.2(red line). The blue line shows the "actual" scatter profile, extracted from an image reconstructed using solely scattered events. The dashed line shows a 4th order polynomial fit to the weighted subtraction profile (red line). (d) The extracted true profile compared to the "actual" true profile obtained from Geant4.

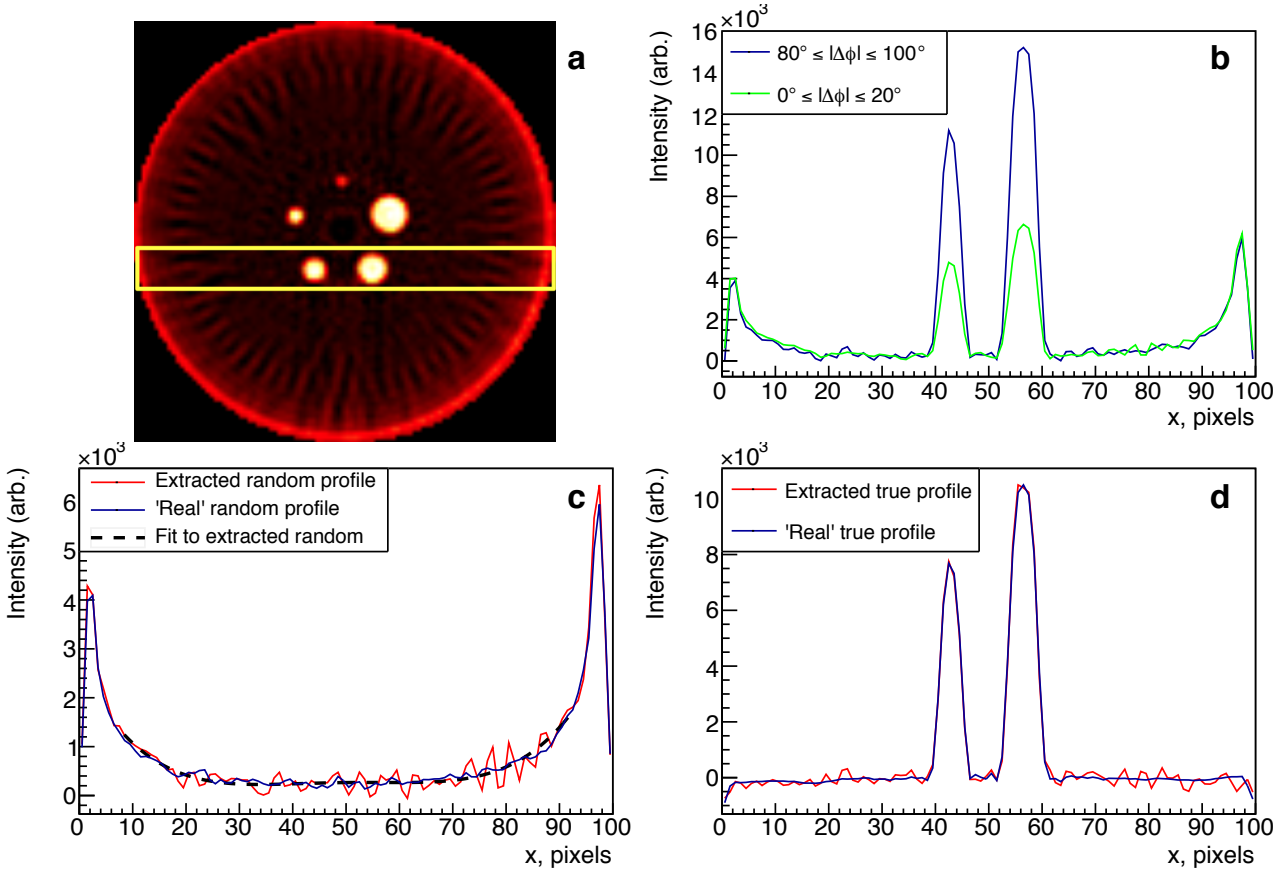

Figure 5.10: (a) A FBP 2-D PET image of the NEMA-NU4 phantom containing true and random events. (b) Cross-sections through the bottom two capillaries, taken from images reconstructed with different $\Delta\phi$ cuts. (c) A weighted subtraction of the two profiles in (b) according to Eq. 5.3(red line). The blue line shows the "actual" random profile, extracted from an image reconstructed using solely random events. The dashed line shows a 4th order polynomial fit to the weighted subtraction. (d) The extracted true profile compared to the "actual" true profile obtained from Geant4.

The above procedure was repeated for the case of a random background and the results are shown in Fig. 5.10(c) and (d).There is excellent agreement in both the shape and the magnitude between the extracted random profile and the "true" random profile. The reconstructed image increases in brightness towards the edge of the field of view. This is a common PET artefact that arises from the detector geometry, since there is a higher density of possible LORs around the edge of the scanner than through the center. To compensate for this, a normalisation correction is usually applied, whereby a second scan of the empty FOV is taken and the result subtracted from the original. In our experiment no normalisation corrections were applied, however through subtraction of $\Delta\phi$ windows we were still able to accurately model its impact.

Using this new method the contribution of random and scatter events to the image background can be extracted. Since the number of annihilations simulated was comparable to the cumulated activity in a clinical PET scan, these backgrounds are indicative of the quality that can be achieved from real PET data. This initial study employed just two $\Delta\phi$ windows and a restrictive θ cut, in future these cuts could be optimised to find a compromise between enhancement magnitude and event yield.

5.5 Future Perspectives

The work described above presents a new way to obtain information on the scatter and random contributions in PET. It should be remarked that, although it exploits only a fraction of the total yield, the information obtained can be utilised in analysis of the entire PET yield.

In this proof-of-principle analysis of entangled-PET the filtered-back-projection (FBP) algorithm was implemented to reconstruct images. However, this is fast becoming an outdated reconstruction technique, with most new-generation PET scanners implementing iterative reconstruction processes such as the MLEM algorithm (see Chap. 3). Many of these algorithms rely on a previous estimate of the scatter distribution, either through scatter simulation algorithms or monte-carlo simulations [TAK10; Bur02], both of which require anatomical information from a prior CT scan. Through the manipulation of $\Delta\phi$ information, these scatter backgrounds can be obtained from the PET data itself, potentially negating the need for combined CT scans for scatter correction. In this way the additional information contained in double Compton scattering angles can be utilised without compromise to the overall sensitivity.

Even in standard scatter correction methodologies the entangled PET information can be combined. For example, MLEM involves a significant number of iterations and does not converge well in certain imaging scenarios. The entangled PET information would give spatially resolved and quantitative starting points for the MLEM, with the possibility of faster and

potentially more accurate convergence.

Chapter 6

Applications in LYSO Detectors

In Chapter 4 it was shown that the $\Delta\phi$ correlations of entangled γ can easily be extracted from highly pixelated, high energy resolution detectors. In Chapter 5 we demonstrated that these correlations can be utilised to provide additional information on random and scatter image backgrounds in PET. The CZT detectors studied in previous chapters offer significant improvement in position resolution over the inorganic scintillator detectors currently used in PET and are therefore ideal benchmarking detectors for studies of entanglement. However, it is also important to study the clarity with which entanglement information can be extracted from conventional PET detector systems.

In this chapter the same measurements are reproduced using LYSO scintillator crystals. Lutetium-yttrium oxyorthosilicate (LYSO) and lutetium oxyorthosilicate (LSO) are the two most widely used scintillator materials in PET detectors today. They offer improved timing resolution compared to the prototype CZT system. However, they have a significantly poorer position and energy resolution, which makes the identification of double scattering events much more challenging. In this analysis, we utilise "event mixing" in order to model the angular acceptance of the detectors and consequently extract out the underlying $\Delta\phi$ correlation. This $\Delta\phi$ correlation is presented and shown to be in excellent agreement with QE-Geant4 simulation results of the same setup (Section 6.3).

A second measurement of the $\Delta\phi$ correlations between previously scattered γ is also performed. This measurement achieved higher statistics and was performed with the inclusion of an active scatterer. Preliminary results (Section 6.4.3) were shown to be in good agreement with the non-entangled simulation and consistent with a near total collapse of the entangled wavefunction following Compton scattering.

Lastly an experiment was performed to quantitatively compare the fractions of annihilation γ scattering through given solid angles. The $\Delta\phi$ distributions from both experiment and

simulation were normalised by the number of ^{22}Na decays and found to be in disagreement within error (Section 6.5). This was a first test of the double Compton scattering cross section of annihilation γ, although further experiments are now planned.

6.1 Feasibility studies in LYSO

Initial investigations were performed to gauge the ability of these LYSO array detectors to identify double Compton scattered events. A Geant4 simulation was created with a beam of 511 keV γ incident on a 100 mm^3 cube of LYSO. The probabilities of each possible interaction type are shown in Tab. 6.1.

Compared to the previous CZT studies, there is a noticeably lower cross section for Compton scatter. Just 67.3% of γ undergo a Compton scatter as their first interaction, compared to 81.7% in CZT. This has advantages for traditional PET as energy deposits are generally restricted to one pixel, with far less inter-crystal scattering. However, for the purposes of this experiment it reduces the fraction of useable double scattered events.

Of the γ that underwent a Compton scatter, 42.3% subsequently underwent a second Compton scatter, 54.8% interacted via the photoelectric effect and 2.9% exited the crystal with no further interactions.

Table 6.1: Interaction probabilities for a 511 keV annihilation photon in a 100 mm^3 block of LYSO.

Interaction Type	Probability (%)
First interaction Compton scatter	67.3
First interaction photoelectric absorption	32.6
Photon lost	0.1
Compton-Compton	28.5
Compton-photoelectric	36.8

A second detector head was then added to the simulation in order to incorporate the probabilities for coincident pairs. The detector dimensions were reduced to 24 x 24 x 50 mm to model the true size of our in-house detector arrays. Table 6.2 shows the relative probabilities of events of interest. Only the latter two (Compton-Compton and Compton-photoelectric events) contain the information required to reconstruct scatter angles, making up 34.6% of the total yield. It should be noted that the true fraction would be smaller, as the laboratory source emits radiation isotropically and the simulation contained only γ travelling along the z-axis.

Table 6.2: Relative contribution of different event sequences for a beam of back-to-back entangled γ incident on two 24 x 24 x 50 mm LYSO crystals.

Interaction Type	Probability (%)
Both γ Compton scatter	43.3
Both γ photoelectric	10.2
One photoelectric, one Compton scatter	42.0
At least 1 γ does not interact	4.5
Both γ Compton-Compton	6.3
Both γ Compton-photoelectric	11.1
One Compton-Compton, one Compton photoelectric	16.9

The ability to create LYSO crystals with significantly larger dimensions increases the sensitivity of these detectors. For this larger geometry the probability of detecting a useable event (even with the lower Compton scattering cross section) is 34.6% compared to just 1.3% in the previous CZT setup.

6.1.1 Intrinsic Radiation

One of the main drawbacks of LYSO as a radiation detector is that the material itself is radioactive. Naturally occurring Lutetium contains ~2.6% ^{176}Lu, which beta decays with a mean energy of 182 keV and maximum energy of 593 keV, to excited states of ^{176}Hf with a half life of 3.76×10^{10} years. This is followed by the emission of prompt gamma rays with energies of 307, 202 and 88 keV [Alv18]. Fig. 6.1 shows the total spectra measured by the detectors when a ^{137}Cs source is placed between the two. We can clearly see the 662 keV gamma produced as part of the decay chain of ^{137}Cs on the right. However, even more prominent are the two peaks corresponding to 202 and 307 keV prompt γ originating from the intrinsic LYSO decay.

This effect becomes event more noticeable when using low activities and could cause difficulties reconstructing events in lower energy ranges. However, they can largely be removed by requiring a hardware coincidence between the two detector heads. For context, a 511 keV gamma scattering at 82°(the angle at which enhancement is optimised) imparts 236.4 keV to the target electron and 274.6 keV to the scattered photon. These prompt gamma rays are precisely in the regime where they could cause issues with event reconstruction. As a consequence data was acquired with a hardware coincidence trigger in place and a strong source of 2.38 MBq in order to reduce the relative contribution of these unwanted events.

For our prototype system there is also a significant contribution from electronic noise below ~120 keV when operated in singles rather than coincidence mode (see section 6.5).

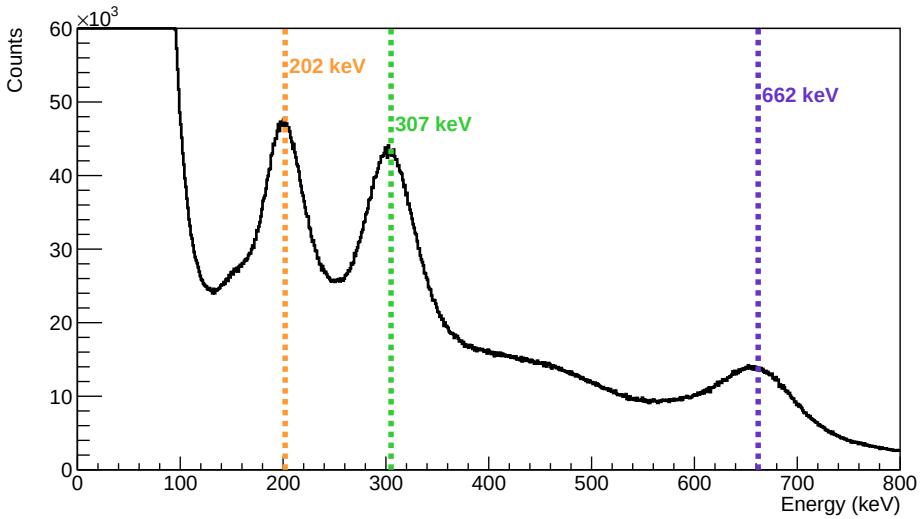

Figure 6.1: ^{137}Cs Energy spectra measured with a LYSO detector with no hardware trigger applied. The 662 keV photopeak is clearly visible along with two peaks at 202 and 307 keV corresponding to the intrinisc radiation from ^{176}Lu decay.

6.2 LYSO experimental setup

A new detector system was acquired in the laboratory. The detectors were composed of LYSO crystals arranged in an 8 x 8 grid. Each crystal had dimensions of 3 x 3 x 50 mm. These dimensions are comparable to those in many full body scanners, e.g the EXPLORER system (2.76 x 2.76 x 19.1 mm^3) [VMK20]. The pixels were surrounded by a BaSO4 reflector of thickness 0.36 mm, the purpose of which was to retain scintillation photons inside the pixel in which they were formed, reducing "charge sharing" effects. The crystals were read out by an array of Hamamatsu SiPMs which were in turn connected to a PETsys Time-of-Flight ASIC data acquisition kit. Additional grounding cables were connected between the SiPM and ASIC board to reduce noise in the readout. A photograph of the experimental setup is shown in Fig. 6.2.

Each channel was individually calibrated using energy spectra from ^{22}Na (511 keV), ^{137}Cs (662 keV) and two of the intrinsic self activity peaks found in LYSO (202 and 307 keV). The energy resolution of the detectors was found to be 14% FWHM at 511 keV. However, since in this analysis we use the summed energy deposited over two separate interactions, this effectively increases the statistical uncertainty on the total recorded energy. The summed energy spectra of two separate interactions was found to be 17.5% FWHM.

A coincidence window of 20 ns was applied to the data. Fig. 6.3 shows how the total recorded event energy, from an incident 511 keV γ, varies with the coincidence window applied.

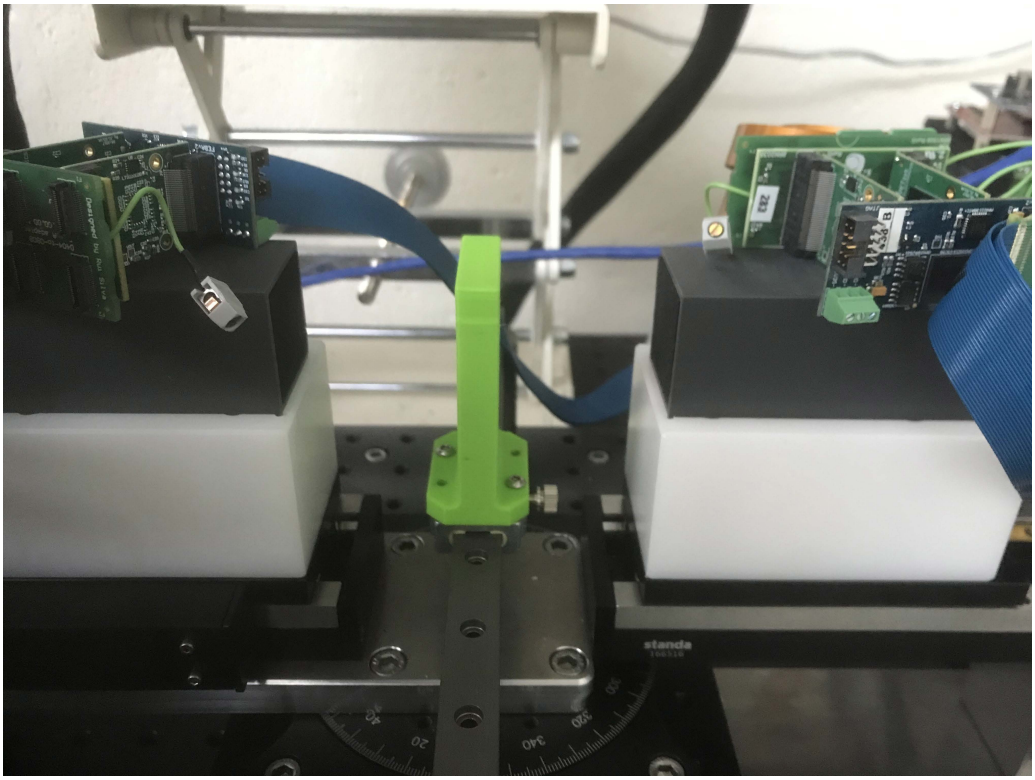

Figure 6.2: A photograph of the LYSO experimental setup. The LYSO crystals themselves are wrapped in light-tight tape and encased in a 3D printed sleeve, seen as the gray boxes mounted on either side. The detectors were mounted on a ThorLabs rotation stage. A custom mount was built for the ^{22}Na source which could slide along a rail between the two detectors to allow for alignment.

If too short a coincidence window is applied the full event energy may not be registered. In Fig. 6.3 this is seen as a reduction in the height of the photopeak for data acquired with a 1 ns coincidence window. However, as the coincidence window increases the fraction of accepted random coincidences will also increase. In the setup described here using a coincidence window of 20 ns the fraction of random events was calculated to be 0.4%.

6.3 LYSO simulation and Data Analysis

Once more the system was modelled using our modified QE-Geant4 simulation. A rendering of the setup is shown in Fig. 6.4. For each annihilation event the simulation recorded the total energy deposited in each crystal. These energies were then smeared by a Gaussian to match the energy resolution of the laboratory detectors, with 17.5% FWHM at 511 keV. The resulting simulation data set was then passed through exactly the same analysis code as the experimental data.

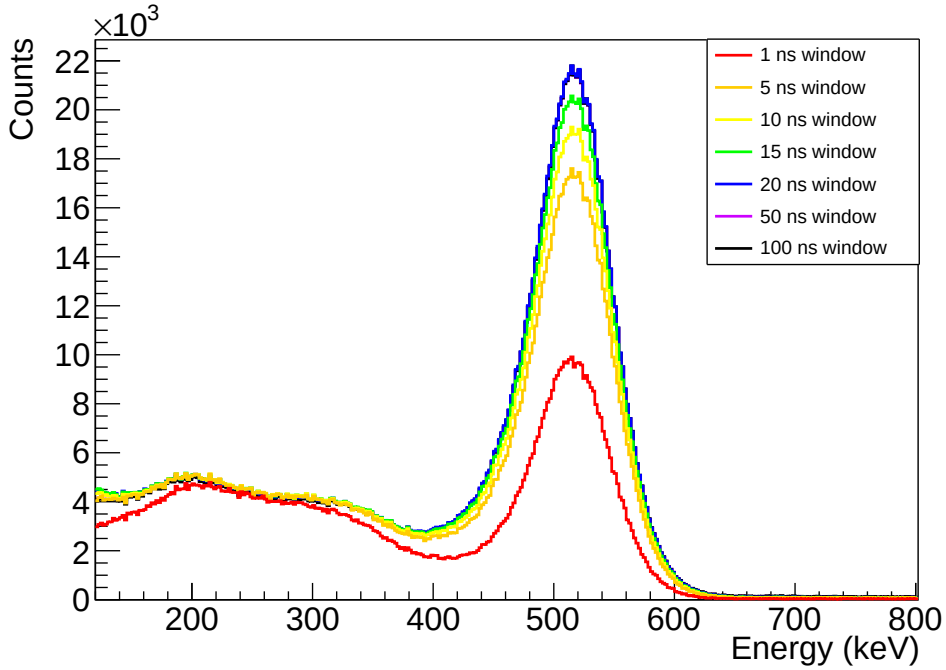

Figure 6.3: The summed energy distribution from a ^{22}Na source with coincidence time windows of 1, 5, 10, 15, 20, 50 and 100 ns.

In the previous CZT experiment (described in Chap 4) the large contribution of charge sharing events forced the use of clustering algorithms. Adjacent triggered pixels could not be accurately identified as two separate Compton scatters rather than the result of charge sharing. Consequently, events were only considered for analysis if two separate clusters of pixels were detected. In LYSO however, the large pixel dimensions and the reflector casing between pixels means that charge sharing is much less of an effect. The electron path length inside LYSO is 0.03 mm meaning that the majority of energy deposits from annihilation photons are contained within one pixel. As such, events containing multiple triggered pixels are far more likely to correspond to inter-crystal scatter, rather than charge sharing from a single energy deposit.

A simulation was run to measure the average path length in the x-y plane of the scattered γ inside the LYSO detector. The results are shown in Table 6.3. It was found that 42.0% of Compton scatters would be re-detected in the same crystal, and 34.9% detected in an adjacent pixel. Consequently, triggers between neighbouring pixels now represent the dominant event type. As such our previous analysis was modified to remove pixel clustering corrections. Instead events were only considered if exactly two pixels triggered in each detector head (independent of their separation). An energy cut was also applied to remove scatter coincidences and low energy noise. The total deposited energy in each head was required to be in the range 470 - 550 keV.

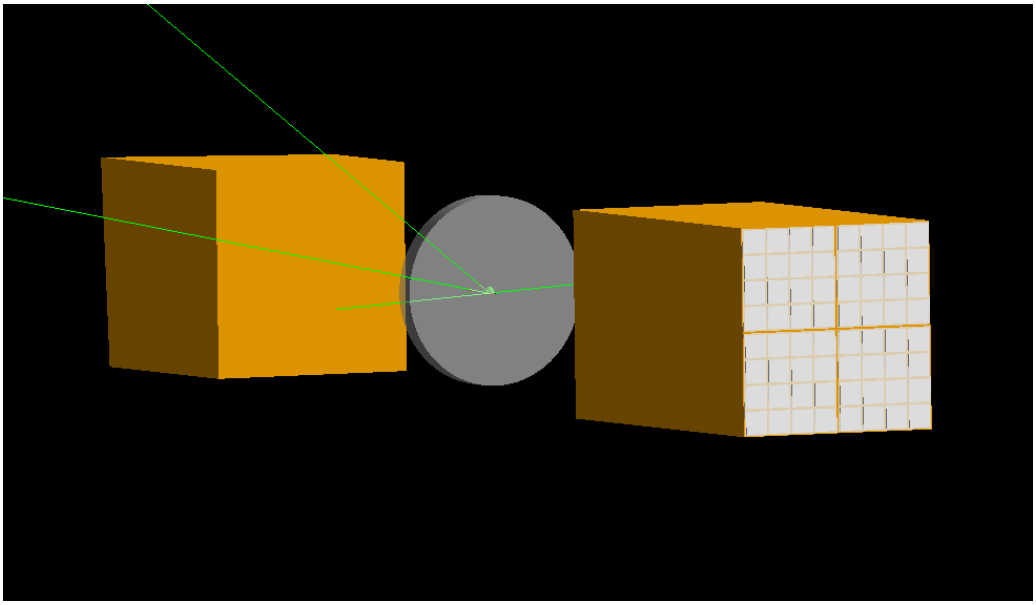

Figure 6.4: A Geant4 rendering of the LYSO experimental setup. The LYSO pixels are arranged in 8x8 arrays. Each crystal face is covered by a $BaSO_4$ reflector of thickness 0.36 mm, except the back face which connects directly to the SiPMs. A 2.2 MBq ^{22}Na source was placed equidistant between the two detector faces. It is composed of a 0.5 mm radius active bead surrounded by a plastic disk of thickness 3 mm and radius 12.5 mm. The source to detector separation was 53.5 mm.

Table 6.3: The average distance travelled by the scattered photon before re-detection, measured in pixels.

Scattering distance x	Probability (%)
$x < 1$ pixel	42.0
$1 < x < 2$	34.9
$2 < x < 3$	13.8
$3 < x < 4$	5.8
$4 < x < 5$	2.3
$5 < x < 6$	0.9
$7 < x < 8$	0.3

As done previously, θ scattering angles were extracted from the energy deposited in the first interaction using Eq. 1.1. The first interaction was assumed to correspond to the highest energy deposit, an assumption that is correct in $\sim 60\%$ of cases. The effect of the lower energy resolution of LYSO results in a somewhat reduced θ resolution. In order to select events from the region of maximum enhancement (Fig. 1.4) a θ window of $54^\circ \leq \theta \leq 110^\circ$ was applied. This is intentionally wide in order to account for the more limited resolution of the LYSO detectors.

ϕ scattering angles were calculated from the position coordinates of each energy deposit.

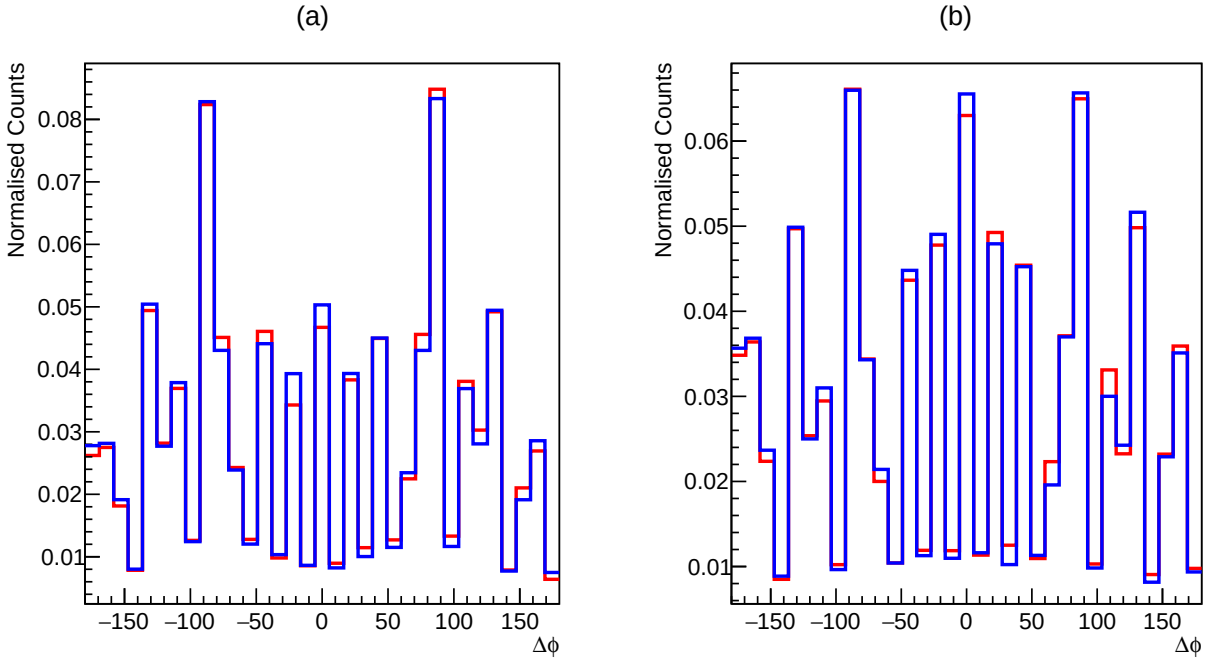

Figure 6.5: $\Delta\phi$ distribution normalised by total counts. (a) **Red** show laboratory data, **blue** simulation data. (b)**Blue** data shows the $\Delta\phi$ distribution obtained from a simulation of unpolarised, independent photons. **Red** shows the obtained $\Delta\phi$ distribution when event mixing is performed.

The reduced ϕ resolution imposed by the large crystal size of LYSO (x 3.75 larger than that of CZT) becomes immediately apparent from inspection of the overall $\Delta\phi$ distribution between the two detectors. This is shown for both simulation and experimental data in Fig. 6.5(a). The measured phi is discretised corresponding to the geometry of the detectors. It is noticeable that that the peaks at $\pm 90°$ are significantly higher than those at $0°$, however there is no evident $\cos(2\Delta\phi)$ distribution. This has been drowned out by the intrinsic acceptance, and therefore varying event rates, of the detectors themselves. ϕ angles corresponding to nearest neighbour pixels ($0°$,$45°$,$90°$,$135°$ etc) dominate the distribution, with intermediate angles (corresponding to crystals with larger distance between them) showing lower event rates.

Fortunately, this effect is accurately modelled by our QE-Geant4 LYSO simulation (plotted in blue). The excellent agreement between simulated and experimental results allows the use of our QE-Geant4 simulation to model and correct for the contribution of these acceptance effects. If we consider the case of back-to-back unpolarised photons, the resulting distribution should be entirely independent of $\Delta\phi$. Therefore any structure observed must originate from the limited detector geometry. The simulation was modified to model back-to-back unpolarised

γ and the resulting $\Delta\phi$ distribution is shown by the blue line in Fig. 6.5(b). The overall structure is similar to that of the entangled events, however the peaks at 0° and ±90° are now of equivalent magnitude.

This unpolarised distribution cannot be physically reproduced in the lab with coincident data, as all annihilation γ display polarisation correlations. However, we can model independent γ by employing event mixing. This method is used widely in particle and nuclear physics analyses using detectors with complicated acceptance [Due19; Ach20]. ϕ angles from events detected in different time windows were randomly paired in order to create an artificial "unpolarised" data set. This data set contains the intrinsic acceptance of the detectors, however any polarisation correlations between the two γ are randomised. The $\Delta\phi$ distribution from our randomly paired experimental data is shown by the red line in Fig. 6.5(b). It demonstrates excellent agreement with the simulated unpolarised data.

The underlying $\Delta\phi$ distribution can then be extracted by dividing the $\Delta\phi$ from the experimental data by this artificial unpolarised data set. The resulting distribution is shown by the black data points in Fig. 6.6. Simulation results from both QE-Geant4 and standard (polarised) Geant4 are plotted for comparison. All data sets have been scaled so that their troughs are positioned at unity to allow easy comparison of the $\cos(2\Delta\phi)$ amplitude. There is clearly excellent agreement between the experimental data and our QE-Geant4 results. Once more the standard polarised Geant4 simulation fails to reproduce the full amplitude. Residuals between the simulation data and the experimental result are shown in Fig. 6.7. For the entangled simulation, residuals are evenly distributed around zero, with a reduced chi-squared of $\chi^2/\nu = 1.37$. By comparison there is a strong structure to the residuals from the polarised simulation, with a much larger reduced chi-squared of $\chi^2/\nu = 90.91$.

The same laboratory data is also presented in Fig. 6.8 with a significantly finer binning employed. Even at this much finer scale the underlying $\Delta\phi$ distribution is clearly visible. However this does demonstrate the variation in angular sensitivity enforced by the detector pixelation. Angles corresponding to nearest neighbour pixels (e.g 0°, 90°, 180°, 270°) have very small error bars due to the high probability of measuring such events. They also display a reduced enhancement. This is because there is no sub-pixel resolution, when a γ scatters into an adjacent pixel a wide range of true scatter angles (±45°) are all classified as the same angle. Conversely, there are a very limited number of hit distributions that correspond to angles very close to (but not exactly) 0°. As such these data points have very large error bars.

This result gives further confidence in our entangled description and simulation. Furthermore, it also demonstrates that information from the scattering correlations of annihilation γ can be readily extracted from the standard clinical PET machines already in use today. This

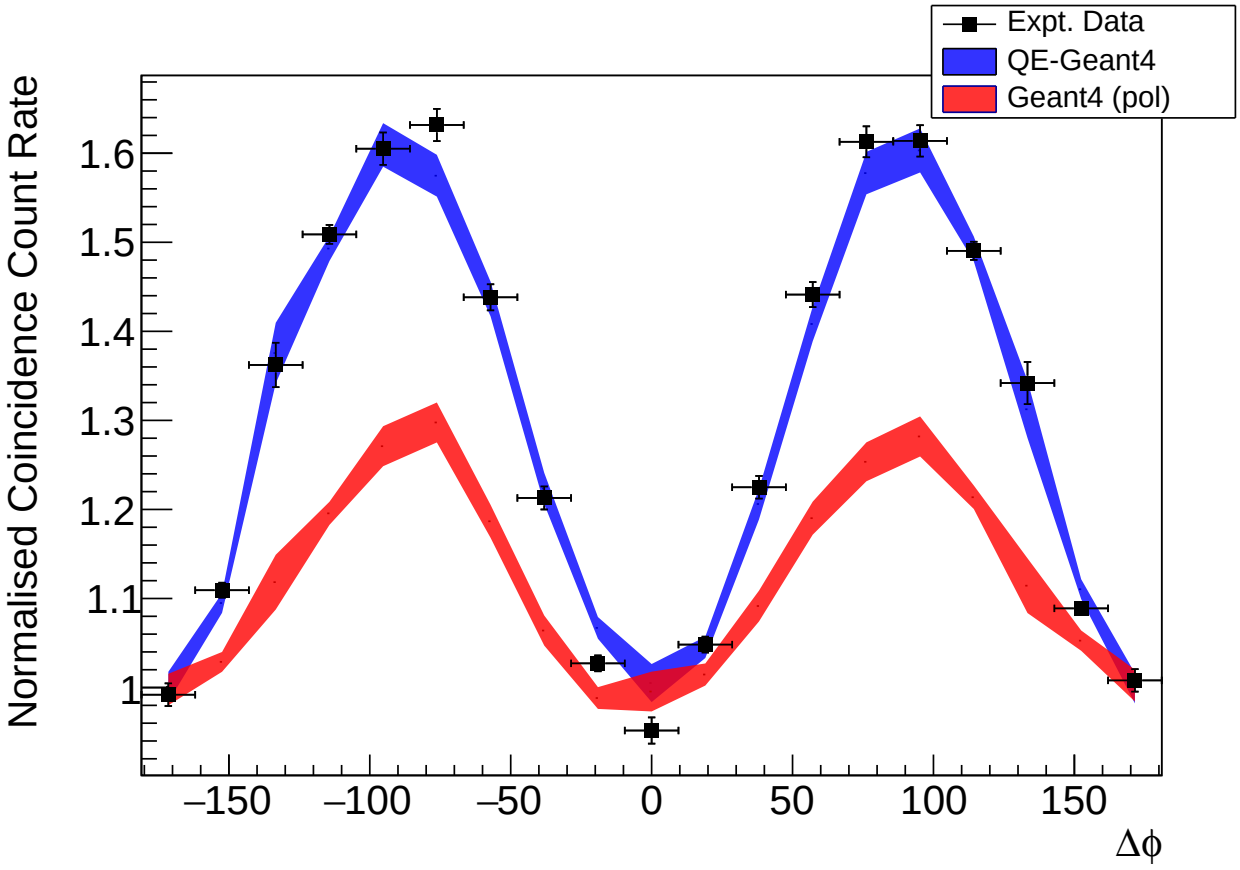

Figure 6.6: The black data points show the experimentally measured coincidence count rate as a function of $\Delta\phi$. The results of the QE-Geant4 simulation are shown by the blue line and a standard polarised Geant4 simulation is shown by the red. The results have been normalised by dividing by an "unpolarised" data set, created by randomly pairing ϕ angles from different events. The width of the simulated bands represent the statistical uncertainty in the measurement.

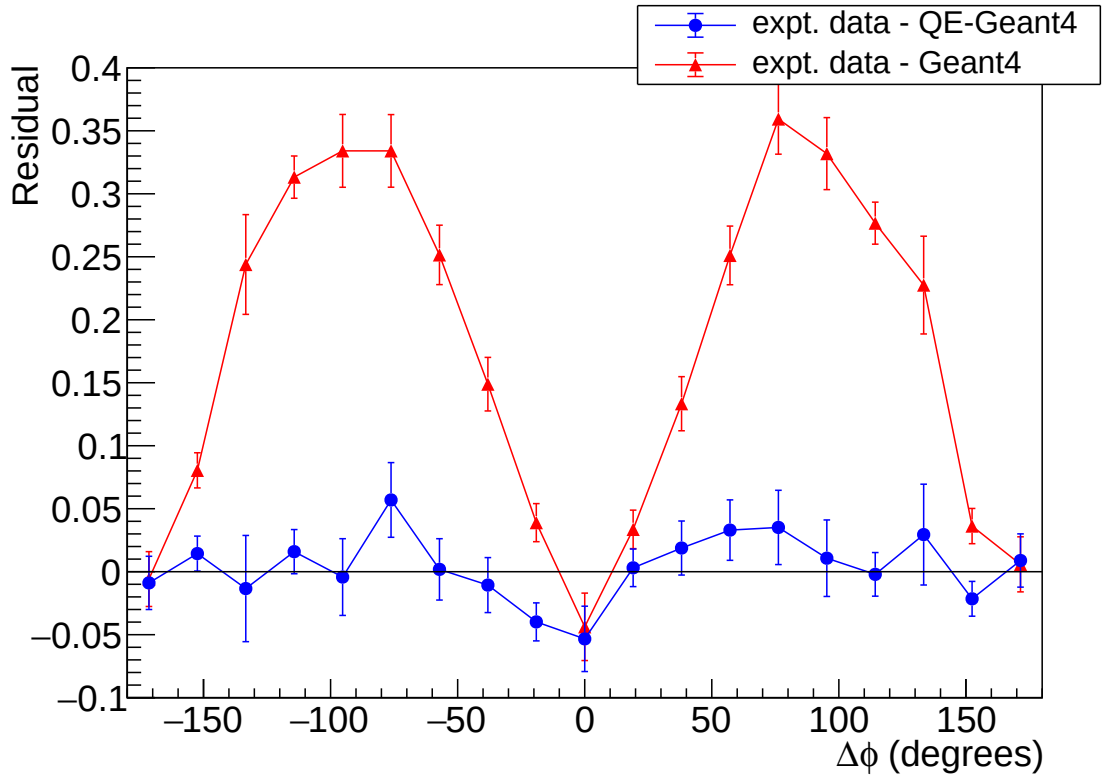

Figure 6.7: Bin-by-bin residuals are shown for experimental data with both QE-Geant4 prediction (blue) and orthogonally polarised prediction (red). Error bars represent the RMS of the statistical error of the experimental data and simulation.

suggests that the image reconstruction techniques demonstrated in Chapter 5 could potentially be applied to list-mode data from such machines, without the requirement for state-of-the-art PET detectors with higher position and energy resolution.

6.4 Scattering correlations between previously scattered photons

Chapter 4 described an experiment which was conducted to measure the residual $\Delta\phi$ correlations between annihilation γ in the case where one γ had previously undergone a decohering scattering process. A reduction in the $\Delta\phi$ enhancement was seen, however, the conclusion of the experiment was limited by very poor statistics. The detector configuration resulted in a low angular acceptance and the issue of pile-up in CZT necessitated a very weak source. The significantly faster timing resolution of LYSO enables us to repeat this experiment with higher statistics.

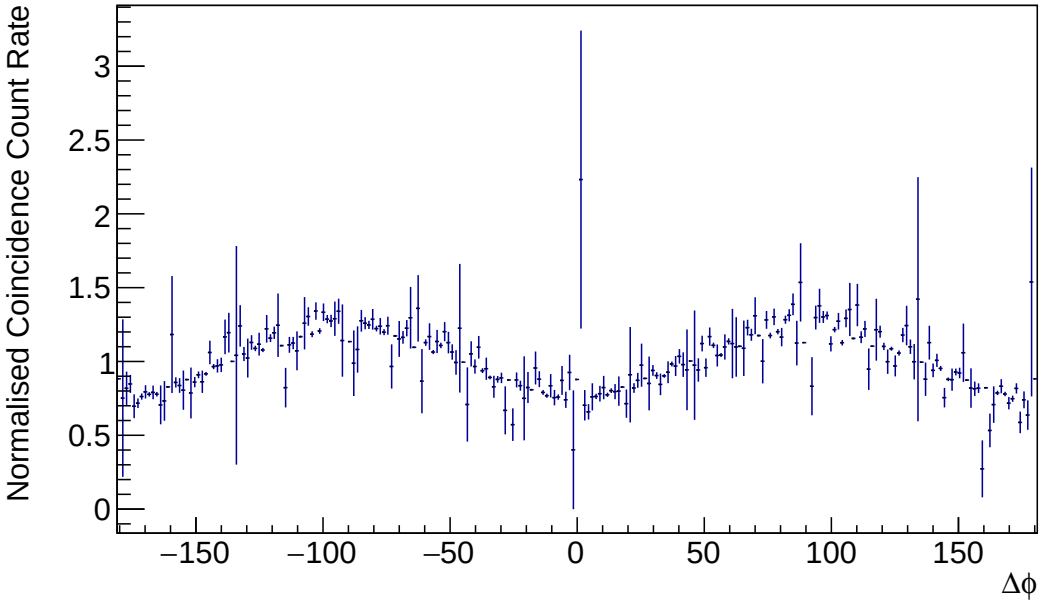

Figure 6.8: The experimental coincident count rate as function of $\Delta\phi$. A fine binning has been used with bin widths of 1.5°. Events were normalised by dividing with an artificial "unpolarised" data set and are distributed around 1.

A similar geometry was constructed, with one detector in the back-to-back position and the other detector head rotated through 45°. This ensured there was no line-of-sight between the two detector heads which passed through the source. The block of nylon from the previous experiment was replaced by a third LYSO crystal, which was attached directly to the source holder to act as a scatterer. This crystal allowed the measurement of energy deposits inside the scatterer itself. By requiring a coincidence between all 3 detectors we could more accurately identify true scattered events and significantly reduce the contribution of random coincidences.

The two complete LYSO detectors were both placed at a separation of 53.5 mm from the ^{22}Na source. The active scatterer had dimensions 12 x 12 x 50 mm and was positioned 3 mm from the source. A rendering of the complete setup is shown in Fig. 6.9.

Events were recorded when two pixels fired in both detector heads within the same time coincidence window (5 ns), along with one pixel in the active scatterer. This gave much greater certainty that the γ in question previously interacted in the scatterer, compared to the data with an inactive scattering medium (Fig. 4.20).

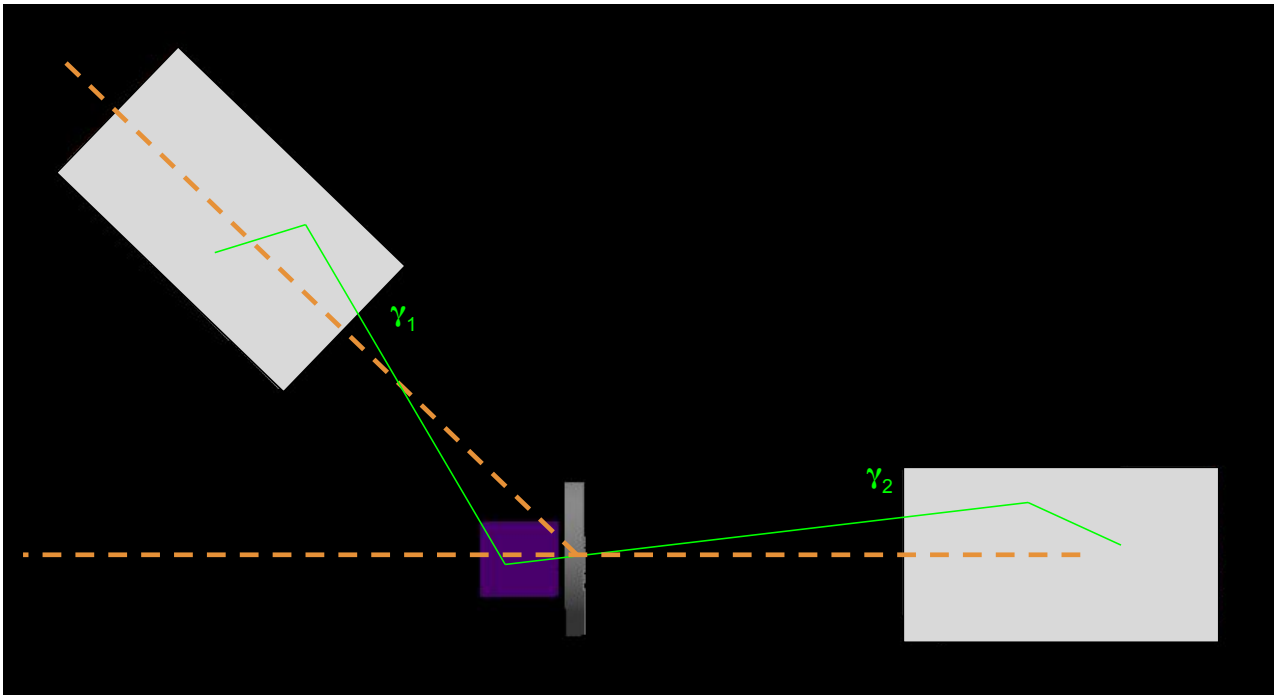

Figure 6.9: A Geant4 rendering of the experimental scattering setup. The two original LYSO detectors are shown as white blocks. Both are placed at a source to detector separation of 53.3 mm, with one detector rotated through an angle of 45° about the source. A third LYSO detector, shown in purple, acts as an active scatterer. The event topology for a typical Compton scattered event is shown by the green lines. The two annihilation γ are emitted from the source in back-to-back directions. One γ undergoes a prior Compton scatter depositing energy in the active scatterer. Both γ subsequently Compton scatter within the LYSO detectors, seen as kinks in the γ trajectories. It is from these final scatters that the $\Delta\phi$ correlation is obtained.

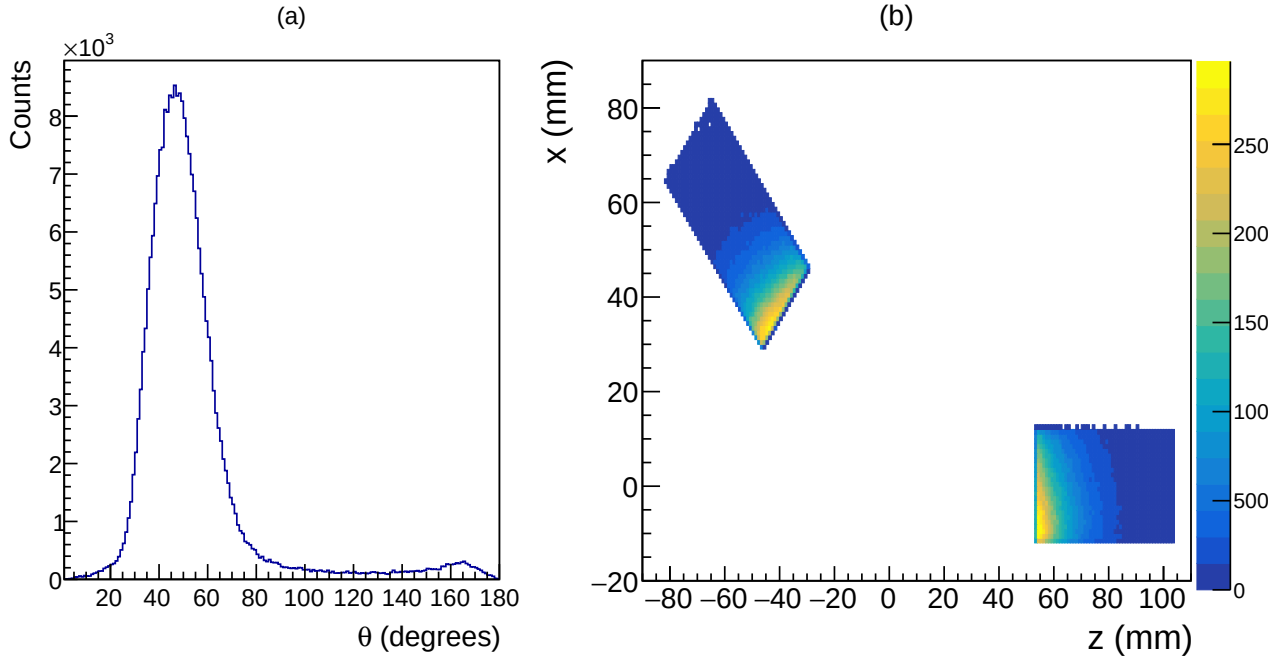

Figure 6.10: Simulation results from a QE-Geant4 reconstruction of the scatter setup. (a) The exact scattering angles within the active scatterer that result in hits in both detector heads. These have been extracted from photon trajectories with no position or energy smearing applied. (b) Distribution of hit coordinates in the two detector heads. Note that the source is positioned at (0,0) and the active scatterer is not shown.

6.4.1 Investigation of the scatter angle acceptance

Studies were carried out in order to calculate the average scattering angle in the active scatterer that could result in energy deposits in both detector heads. From purely geometrical considerations we would expect this to peak at around $\sim 48°$. This is assuming that the average 511 keV γ interacts within the first few mm of the scatterer and is detected near the center of the rotated heads face. However, results from a simulation of the setup show the distribution peaking $\sim 46°$. This is shown in Fig. 6.10(a) where a wide range of angles is detected from 25° to 75°. This bias towards lower angles originates from a higher cross section for lower θ scattering angles in Compton scattering. This bias is reflected in the distribution of hits across the detector face, which can be seen in Fig. 6.10(b), where the exact coordinates of each γ interaction have been plotted. The result is a pronounced bias towards one edge, with more events detected in the lower half of each detector. This effect is important to note as events detected along detector edges can create unwanted angular acceptance effects which impact the overall $\Delta\phi$ distribution, as discussed in Chapter 4.

6.4.2 Data acquisition and analysis

Data were acquired from a 2.30 MBq ^{22}Na source for 50 hrs, corresponding to 414 billion annihilation events. A coincidence window of 5 ns was applied and coincidence was required between all three LYSO detectors. Events were discarded if more than one energy deposit was recorded in the active scatterer during the coincidence window. This was done to remove events which had undergone more than one interaction prior to detection in the main detector head.

The setup was reconstructed in Geant4 using a ^{22}Na source. In total 520 billion annihilation events were simulated. Events were retained when at least two pixels triggered in each detector head and one deposit was identified within the active scatterer. The energy deposits were then smeared to match the energy resolution in each detector, 17.5% FWHM in the two main detectors and 25% FWHM in the active scatterer. Two simulations were run, one in which ^{22}Na annihilation created polarised γ and one with unpolarised photons. The polarised simulation was run in order to model the scenario in which all entanglement is lost during the first interaction. Good experimental agreement with this simulation would represent complete collapse of the wavefunction. The purpose of the unpolarised simulation was to validate the detector acceptance correction, as described in Section 6.3. The feasibility studies suggest a strong bias towards interactions within the outermost pixels. As was shown in Chapter 4, this can have a large impact on the resulting $\Delta\phi$ distribution. If our correction technique using randomly paired events is sufficiently successful, the unpolarised data would be expected to show a flat distribution.

The experimental laboratory data and simulation data were then passed through identical analysis code.

Energy cuts were applied to both detector heads to further isolate true events. In the unrotated head, the total energy deposited between two triggered pixels was required to be in the range 440-560 keV. This is a larger range than the one used in the back-to-back experiment. This was done to compensate for reduced statistics. Similarly, it was required that the sum of the energy deposited in the active scatterer and the energy deposited in the rotated head was in the range 440-560 keV. In this way the total energy of both annihilation γ was accounted for. Low energy cuts of 50 keV were applied to all detectors to remove any contribution from low energy noise.

The top two panels in Fig. 6.11 show the energy correlations between the active scatterer and the rotated detector head for experimental data (a) and simulation data (b). Yellow bands have been added to the figure to represent the energy cuts applied. There is a strong diagonal trend corresponding to events where the total energy deposited between the two sums to 511

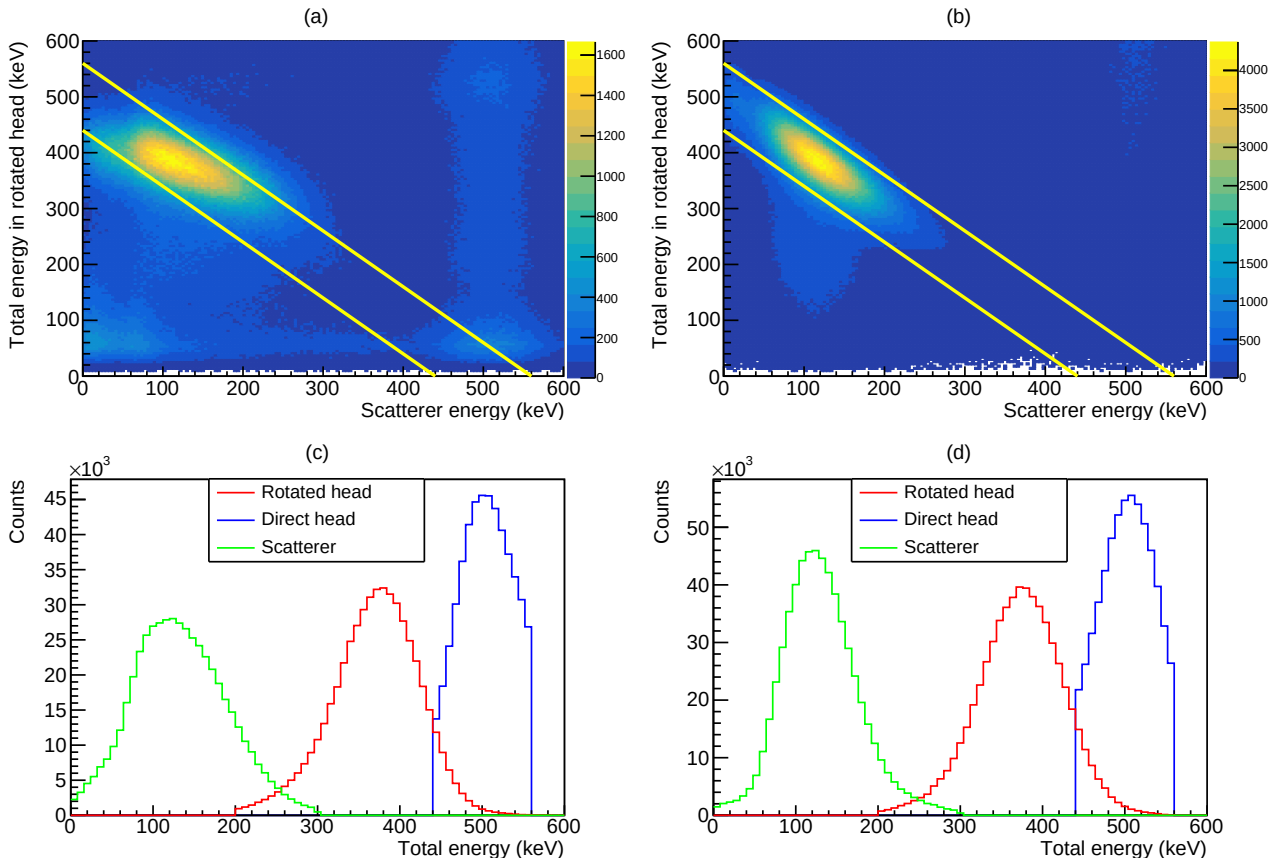

Figure 6.11: The top panels show the energy correlation between the active scatterer and the rotated head for laboratory data (a) and simulation data (b). Yellow bands have been added to represent the energy cuts applied. The bottom two panels show the energies recorded in each of the three detectors for events within the above energy cuts. In (c) we show laboratory data and in (d) we shows simulated results.

keV. There is also a vertical line of coincidences at 511 keV in the active scatterer, which is much more apparent in the laboratory data than the simulation. These events are recorded for a continuous distribution of energies in the rotated head. They correspond to incidences where the two back to back 511 keV γ were detected in the scatterer and the un-rotated head. The 3rd coincidence is either a random coincidence or caused by the prompt γ Compton scattering inside the second head. These events are removed by the application of a third energy window requiring that the energy deposited in the scatterer be less than 400 keV.

The energy deposits in each detector are plotted in the lower panels of Fig. 6.11. As expected, the un-rotated detector shows a peak at 511 keV where the entire γ energy is deposited. In the rotated head, this peak is shifted down to $\sim$395 keV. From the Compton scattering formula (Eq. 1.1) this corresponds to a polar scatter angle of $\sim 46^{\circ}$, in agreement with our preliminary simulation. The energy distribution of the active scatterer peaks correspondingly at $\sim$116 keV, where the remainder of the annihilation γs energy is deposited.

At this stage, true events have been isolated using information from all three detectors. θ and ϕ scattering angles were then calculated purely using the photon interactions occurring within the main detector heads.

Firstly, a θ cut was applied to the events in the LYSO arrays in order to select the region of maximum enhancement. For the case of the un-rotated head, this was calculated from interaction energy exactly as before. Eq. 1.1 was employed assuming that the incoming γ energy was 511 keV and the highest energy deposit corresponded to the first interaction. Interactions in the rotated head were a little more complex. The incoming γ had previously undergone a Compton scatter and hence possessed a lower initial energy. As such θ was calculated from Eq. 6.1 with the initial photon energy taken as 511 keV minus the energy recorded in the active scatterer for that event. This can be written as,

$$\theta = \cos^{-1}\left(1 - \frac{E_1}{(511\text{ keV} - E_{scatt}) - E_1}\right), \tag{6.1}$$

where E_1 represents the highest energy deposit in the detector (assumed to be the first hit) and E_{scatt} represents the energy recorded in the active scatterer.

Using the methodology above, a cut of $50^{\circ} \leq \theta \leq 130^{\circ}$ was applied in order select a region of greater enhancement. This is a wider range than the cut applied to the back-to-back measurements in order to compensate for the lower statistics. From these data, ϕ scattering angles were calculated for each detector head using the position coordinates of the triggered pixels. The overall $\Delta\phi$ distribution between the two heads was then calculated.

The $\Delta\phi$ was corrected for acceptance effects by dividing with an "unpolarised data set",

formed by randomly pairing ϕ angles from events detected in different time windows. This technique was discussed in more detail in Section 6.3.

6.4.3 LYSO active scatterer results

Corrected $\Delta\phi$ distributions are shown in Fig. 6.12(a) and (b). Data in (a) has been normalised such that the trough of each distribution sits at unity to allow for better comparison of the overall amplitude. Data in (b) has been normalised over the entire $\Delta\phi$ range. The first normalisation is highly sensitive to the data contained within a limited number of bins. Given the very low statistics in this experiment both normalisation have been presented to prevent any visual bias.

The black data points show experimental data from the scatterer setup. These are compared to the results from two Geant4 simulations, the polarised simulation is shown by the red band and the unpolarised simulation by the green.

The experimental data and polarised simulation both demonstrate a residual $\cos(2\Delta\phi)$ distribution after a prior scatter. The amplitudes of the two also appear to be in good agreement within statistical uncertainty. Since the polarised simulation incorporates no entanglement information, this indicates that the annihilation γ undergo total loss of entanglement during the first interaction and that the subsequent interactions occur as for independent photons.

The unpolarised data (green band) is largely flat with some small structure visible about $\Delta\phi = 0$. We would anticipate this distribution to be uniform. The slight structure indicates some imperfection in the geometrical acceptance correction. However, any enhancement visible is clearly reduced compared to the polarised simulation and experimental data, giving confidence in our result.

For further comparison, the results of the previous back-to-back setup for both experiment and simulation have been added to the figure. An identical energy cut and θ range were applied to both data sets. The enhancement present in these data represents the full quantum entangled cross section. Even with a wider θ bin applied it is still significantly larger than that of the scattered data, reinforcing the idea that entanglement information is largely lost during the scatter.

Residuals were calculated between the experimental data and the unpolarised, polarised, and experimental back-to-back data, all of which can be seen in Fig. 6.13. The experimental scattered data clearly has diminished amplitude compared to the experimental back-to-back data. The residuals show a strong $\cos(2\Delta\phi)$ dependency and the disagreement results in a reduced chi-squared between the two of $\chi^2_\nu = 3.46$. Residuals between the scattered experi-

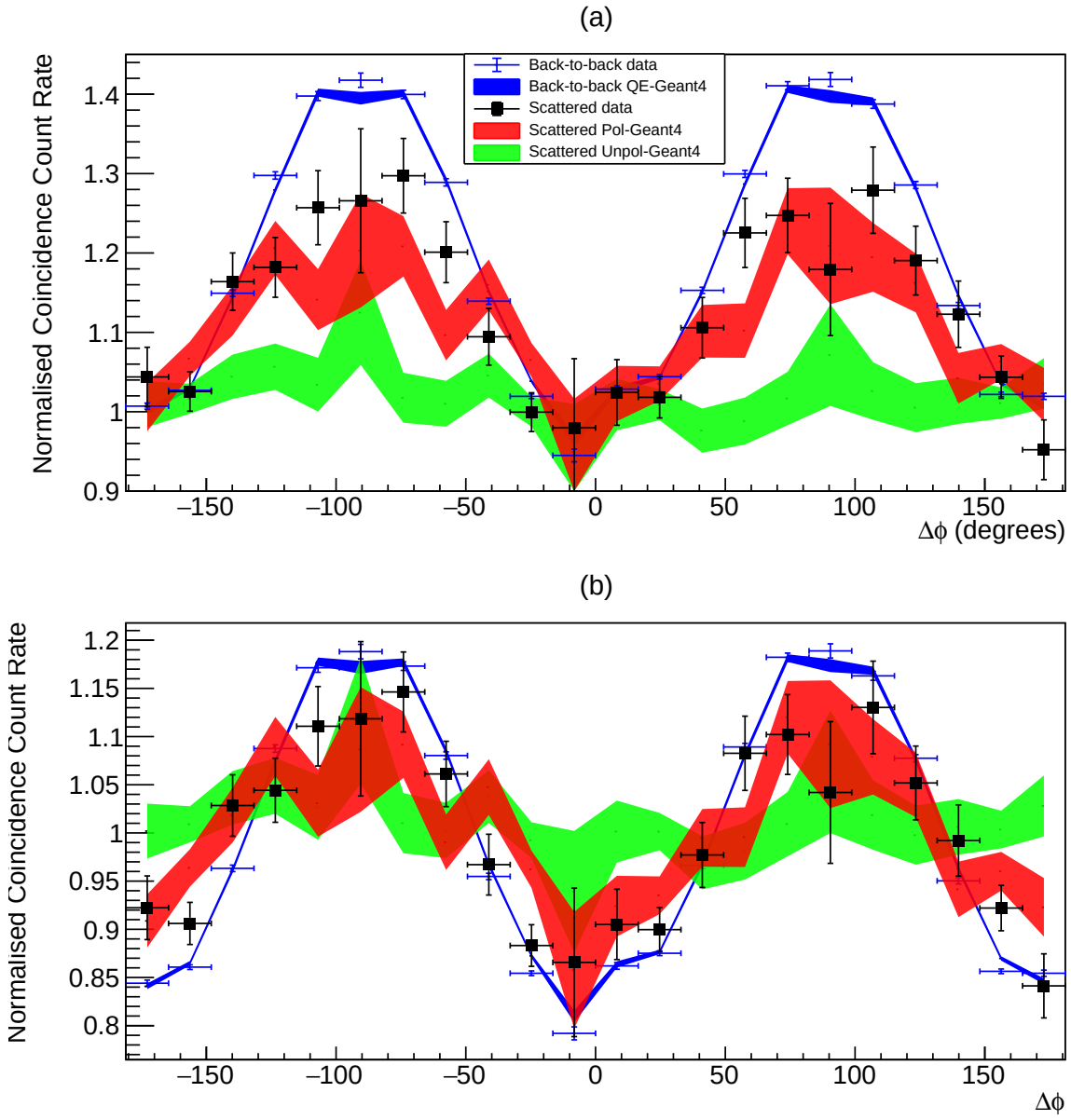

Figure 6.12: The experimental $\Delta\phi$ distribution for γ that have undergone a prior Compton scatter through a polar angle $\sim 45°$ is shown by the black data points. The vertical error bars show the statistical error, calculated from the number of events in each bin and the horizontal error bars show the bin width. The experiment was simulated using both polarised Geant4 (red line) and unpolarised Geant4 (green line). The uncertainties in simulated data are indicated by the line widths. For further comparison the results from the back-to-back experiment and simulation have been added. These are shown by the blue data points and the blue line respectively. A wide θ range of $50° \leq \theta \leq 130°$ has been applied to all data sets. In (a) data was normalised to align the trough of the distribution with 1. In (b) events were normalised over the entire data set.

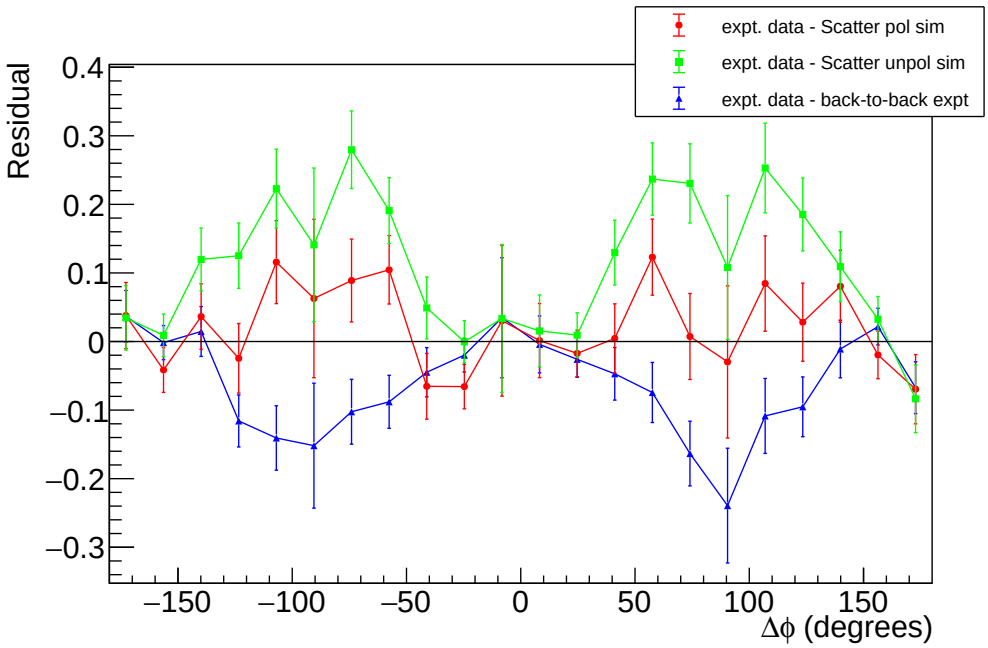

Figure 6.13: A residual plot comparing experimental scattered data with simulation. Bin-by-bin residuals are shown between experimental data from the active scatter setup with polarised Geant4 prediction (red), unpolarised prediction (green), and QE-Geant4 for the back-to-back case (blue). Error bars represent the RMS of the statistical error of the experimental data and simulation.

mental data and the unpolarised simulation show a strong negative $\cos(2\Delta\phi)$ dependency and a reduced chi-squared of $\chi^2_\nu = 7.28$. Best agreement is seen with the polarised simulation, with a reduced $\chi^2_\nu = 1.48$. However, there still exists some structure to the residuals between experimental data and the polarised simulation.

Overall, the residual $\cos(2\Delta\phi)$ distribution is much better defined than in our earlier CZT experiment (Section 4.4.1) due to the significantly increased statistics. The polarised and experimental data appear to be in reasonable agreement, providing experimental justification for our assumption in Chapter 5 of total loss of entanglement. From inspection of the data in Fig. 6.6(a) it appears possible that the experimental data may display a slightly greater enhancement than the polarised simulation. This would imply that some residual entanglement information remains. However the error bars on both data sets are large, and this normalisation technique is highly dependent on information from just a few $\Delta\phi$ bins. Consequently significantly greater statistics would be required before drawing such a conclusion.

6.5 Experimental tests of the double Compton scattering cross section

The double Compton cross section of annihilation γ (Eq. 1.7) was first predicted 75 years ago [PW47; SPH48], however as yet it has escaped experimental confirmation [Car19]. The QE-Geant4 simulation utilised in this thesis opens up new opportunities. It is the first simulation of its kind to incorporate both the entangled correlations of annihilation photons and also accurately model non-Compton processes, backgrounds, detector acceptance effects and detector resolution. In this section a first attempt at confirming this cross section is performed by directly comparing the quantitative yield from a positron annihilation experiment to the yield from an identical QE-Geant4 simulation of the setup. Statistical agreement between the two would provide experimental verification of this theoretical prediction. In this first study agreement was not seen within the estimated systematic error, however it has paved the way for future studies with tighter constraints and better understanding of the systematics involved.

The experimental data was acquired using the same setup as described in section 6.2, with 13 hrs of data recorded. A ^{22}Na source was placed equidistant between the two detector heads, with a source to detector separation of 53.5 mm. The activity of the source on the day of the experiment was taken as (2.27 ± 0.07) kBq, with the uncertainty of 3% provided by the manufacturer. This corresponds to a total of (106.2 ± 0.3) billion decays over the course of the measurement.

The QE-Geant4 simulation used the "G4RadioactiveDecayPhysics" class to model the decay of ^{22}Na. Each simulation event corresponded to a single decay of a ^{22}Na nucleus, which predominantly disintegrates into the 1275 keV level of ^{22}Ne. In 90.3% of events this is via β^+ decay producing usable positrons. In 9.64% this process occurs via electron capture. A very small fraction, 0.056%, disintegrate directly to the ground state of ^{22}Ne. As such, matching the number of events simulated to the activity of the source multiplied by the time of measurement should result in the same number of β^+ emissions and subsequent annihilation events present in the experimental and simulated data.

The simulation data was smeared with a Gaussian of FWHM 17.5% in order to model the energy resolution of the detectors and subsequently passed through identical analysis code to the experimental data. This code was described in further detail in Section 6.2. Events were retained in which only two pixels in each detector recorded an energy deposit. Due to the large contribution from low energy noise in the detectors an additional low energy cut of 160 keV was applied to all data, such that two energy deposits both exceeding 160 keV must be detected in

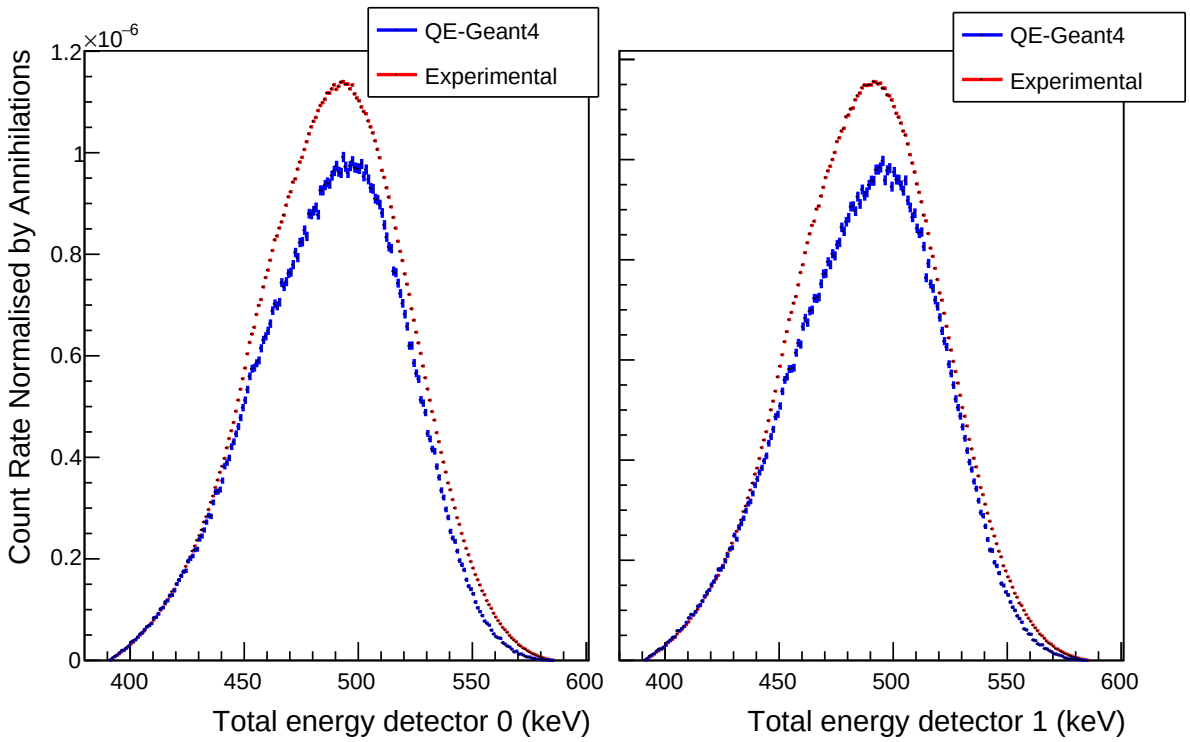

Figure 6.14: The energy spectra measured in detectors 0 (a) and 1 (b) scaled by the number of Na^{22} decays. A θ cut of $70° \leq \theta \leq 110°$ has been applied to all data.

each head to constitute a good event. This cutoff was well below the minimum energy deposit expected for Compton scattering of 511 keV quanta.

Both the experimental and simulated data sets were then normalised by the number of ^{22}Na decays corresponding to each data set. For the simulation data this was simply the number of events simulated, 19.92 billion, and in the laboratory this was taken as the activity of the source multiplied by the duration of the experiment, resulting in ∼106 billion decays.

Fig. 6.14 shows (on an absolute scale normalised to the source strength) the energy spectra measured in both the simulation and laboratory experiment for each of the detector heads. Both show smooth photopeaks however more events meeting the required cuts are detected in the laboratory data than the simulation. This corresponds to a slightly higher fraction of annihilation γ from the laboratory source undergoing a Compton scatter and subsequent re-detection in both detector heads. The shape of the photopeak for the event sample is similar in the experimental and simulated data. The slight asymmetry in the shape is caused by the θ cut, where events with energies recorded in the higher energy part of the Gaussian are more likely to be reconstructed in the theta range (Eq. 1.1).

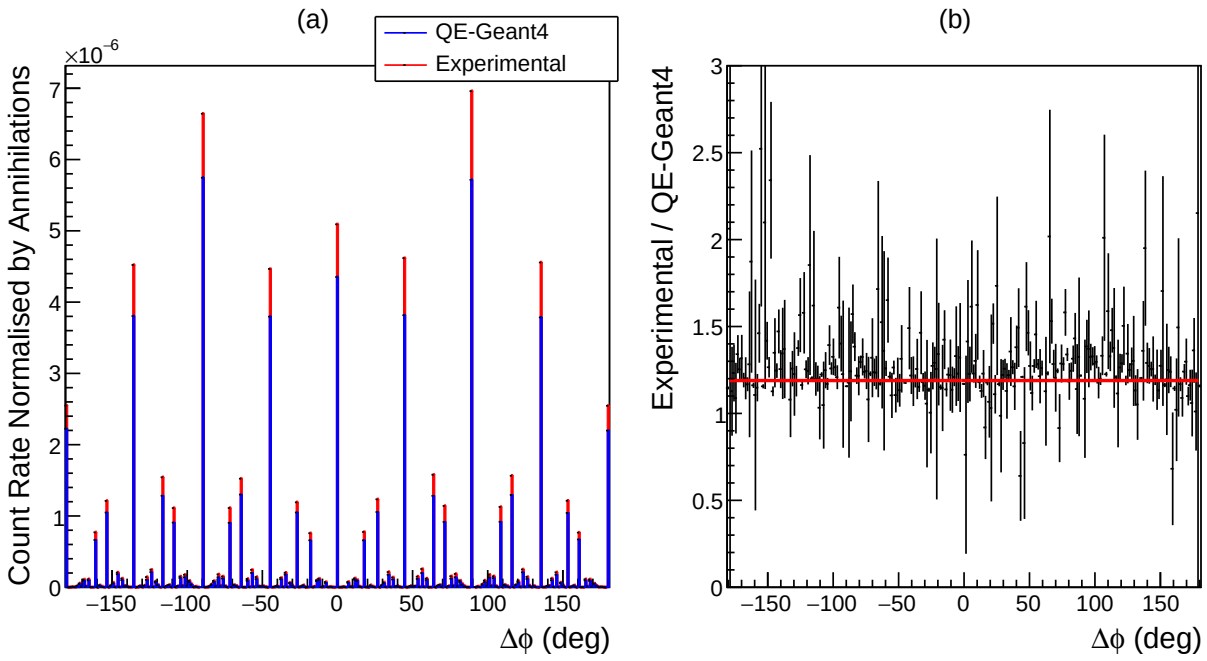

Figure 6.15: (a) The $\Delta\phi$ distribution detected in laboratory and simulation normalised by ^{22}Na decays. (b) Ratio between the $\Delta\phi$ distributions detected in laboratory and simulation. The dotted red line represents a constant fit to the data.

The cross section is obtained with a restriction of the polar angle of the Compton scattered photons (θ) of $70° \leq \theta \leq 110°$. This ensures the cross section comparison is made in regions where the enhancement from the entanglement (Fig. 1.4) is large. The resulting $\Delta\phi$ distributions are shown in Fig. 6.15(a), once again scaled by the number of ^{22}Na decays to set them both on an absolute scale. A very fine binning has been employed with bin width 1.5° so that double Compton scatter events with different topologies in the crystal array occur in separate bins. General agreement in shape between the experimental data and simulation is shown on a bin-by-bin basis. However, a consistently higher fraction of events are recorded in all simulation bins. This is evidenced further in Fig. 6.15 (b), which shows the ratio between the experimental $\Delta\phi$ distribution and that measured in simulation on a bin-by-bin basis. A zeroth order polynomial fit to the data provided a value of 1.175 ± 0.002. We remark that this fit is dominated by the data points with higher statistics resulting from scatter into neighbouring crystals.

6.5.1 Quantifying systematic error in the cross section determination

The acceptance of this LYSO system is highly sensitive to small variations in the geometry of the setup. As such, further simulations were performed in order to quantify the systematic error in the QE-Geant4 reconstruction. A small displacement of one detector away from the source reduces the solid angle covered by the detector face. This leads to a drop in sensitivity proportional to $1/r^2$. As a result the overall acceptance is highly sensitive to detector positioning in the z-plane. In this prototype system the detectors were shielded from external light sources by the use of compressible foam in front of the detector face. As such the exact location of the detector inside its casing could only be measured to a limited precision. Simulations were also performed with both detectors positioned 2 mm closer and 2 mm further away from the ^{22}Na source. This led to a 8% increase and 4% decrease in statistics respectively.

Another highly sensitive parameter is the positioning of the source in the X-Y plane. Since the annihilation γ are emitted back-to-back an offset in the source position will have a two-fold reduction in event yield. γ pairs hitting the extreme edge of each detector will not intercept the equivalent edge of the other detector. Simulations of the setup with a 1.5 mm source displacement parallel to the detector face resulted in a 6% decrease in events. This offset of the source was also found to cause a slight $\Delta\phi$ asymmetry in the overall cosine distribution. Indeed from Fig. 6.15 we can see that at negative $\Delta\phi$ angles the experimental data tends to be slightly lower than the simulation, whereas at positive $\Delta\phi$ angles the reverse is true. By analysis of the event distribution in the experimental data it was estimated that the source may have been offset by ~ 0.5 mm in the X direction.

The crystals were arranged in 4 blocks of 4x4, each encased in a canister and covered with light tight tape. Since this tape is slightly compressible variations in tape thickness and hence crystal separation were simulated. A 0.25 mm increase resulted in a 4% change to the overall yield.

In order to model the finite energy resolution of the laboratory detectors the QE-Geant4 energy deposits were smeared with a FWHM (at 511 keV) of 17.5%. However, this detector displayed significant temperature drift causing the photopeak to move over the course of the measurement. Each individual hour of data was recalibrated, but nonetheless it was not possible to fully account for these effects and they may have caused a deformation to the photopeak. Therefore, to account for possible variations in the energy resolution, the simulation was smeared with a 2% higher and lower FWHM, which resulted in $\pm$4% change to the yield.

Systematics in the absolute yield could also arise due to the contribution of random events

to the sample. The fraction of randoms in the experimental setup (i.e. the contribution from γ events not originating from the same annihilation event) was calculated by acquiring a second data set with one head rotated out of alignment. The fraction of random 511 keV coincidences was found to be 0.4% compared to the back-to-back setup.

Lastly, the activity of the ^{22}Na source was quoted by the manufacturer to an accuracy of 3%. By summing these uncertainties in quadrature the overall uncertainty in absolute yield derived from the simulated data was estimated to be of the order of 12%. Consequently, experimental data were not in agreement with the simulated model within the systematics described here.

The QE-Geant4 simulation employed in this experiment uses the predicted cross section of Pryce and Ward [PW47] to model the scattering distribution of annihilation γ. In this first study the fraction of events scattering through a given θ and ϕ angle were found to differ between the simulation and experimental data by 17.5%, suggesting a higher cross section than the current theoretical predictions.

However, the experiment was hindered due to noise issues experienced with this prototype setup. A new detector array is being commissioned with redesigned electronics to reduce low energy noise. Additional modifications will be made in order to provide tighter constraints on systematic errors. The detectors shall be encased in a temperature controlled unit to prevent temperature drift and hopefully allow for higher resolution measurements. This will also provide sufficient light insulation, without the need for compressible foam shielding, so that the detector separation may be measured to a higher accuracy. Additionally, the QE-Geant4 simulation may be modified to incorporate the surrounding detector electronics and support system to account for any contribution from backscattered events. The analysis of this new system will be based on the methodologies developed here.

Chapter 7

Conclusions and future perspectives

This thesis presents advances in both the simulation and detection of entangled gamma quanta from positron annihilation.

A modified simulation of gamma interactions in matter, based on the Geant4 simulation framework, has been developed and tested. This provides a first modelling of the role of quantum entanglement in the way that gamma photons interact in matter, accounting for the predicted cross sections for double Compton scattering of entangled quanta. The simulation results were benchmarked to the underlying theoretical predictions of Bohm and Aharanov [BA57]. This development provides a sound simulation basis for a programme of precision tests of the fundamental nature of entanglement at the MeV scale, and the exploration of its application in pure science and applied physics. The development has recently been released and made available to the international community in the latest release of Geant4 and provides an important improvement in the modelling of entangled gamma propagation in matter.

Two segmented detector array systems were used to obtain experimental data on double Compton scattering of annihilation photons.

The first system comprised two 8.8 x 8.8 x 10 mm CZT crystals discretised into 121 0.8 x 0.8 mm pixels through a pixellated anode. The information on the Compton scatter processes (polar (θ) and azimuthal (ϕ) angles) in each crystal were extracted from the deposited energies and hit positions. The resulting correlations between the azimuthal scatter planes of the Compton scattered photons ($\phi_1 - \phi_2$) exhibited a $\cos(2\Delta\phi)$ dependence. The measured amplitude of the $\cos(2\Delta\phi)$ modulation (1.95 ± 0.07) was well described by the new entangled Geant4 simulation, giving important evidence to the validity of the underlying entanglement theory. The measured amplitude is well above the maximum predicted for non-entangled (independent) Compton scatters of polarised photons (1.63). The result confirms the need for entanglement effects to be considered in order to accurately model the scattering of annihilation photons.

Measurements with a LYSO demonstrator comprising 64 crystals of 3 x 3 x 50 mm, and well matched to the detectors in next-generation PET systems, showed that the azimuthal correlations can also be quantified in such segmented detector arrays. A measured amplitude of 1.580 ± 0.007 was observed compared to the independent photon limit for the same geometry of 1.30 ± 0.01. The acceptance of such systems is complex due to the different event topologies but it was shown that QE-Geant4 can account well for these effects. Event mixing methodologies also showed success in removing the acceptance and would appear to be valuable in future analysis of such systems.

A first investigation of entanglement loss for photons in this energy scale was also obtained, through analysis of the $\Delta\phi$ correlations where one of the photons underwent a Compton scatter prior to entering the detector arrays. The best quality data was obtained from the LYSO arrays and the measured $\Delta\phi$ correlations were consistent with Geant4 predictions for independent photons. This suggests a near complete loss of entanglement with a Compton scatter process, although further data with higher statistics and covering more scatter angles is needed to fully establish this.

A first measurement of the cross section for the double Compton scatter of entangled positron annihilation gamma was also obtained. The obtained value for the ratio between experimental data and entangled Geant4 was $1.175 \pm 0.002 \pm 0.12$ (systematic). The measurement is slightly outside the combined statistical and estimated systematic errors. Although this could indicate an underestimate of the actual cross section by the theory, as discussed in the text, it is clear that a new apparatus with more controlled and smaller systematic errors would be necessary to confirm or refute this. However, the proof of principle is established with the work presented here.

The benchmarked entangled QE-Geant4 was used to obtain a first simulated study of entangled PET. A new way to process the PET data was developed, accounting for the differing $\Delta\phi$ correlations of true PET events, scattered PET events and random PET events. It was shown that the quantum entanglement information alone allows for separation of the different contributions to the image. This offers exciting prospects for next generation PET systems. It also has the potential to mitigate some of the issues in the adoption of CZT in PET, due to its comparatively poor coincidence time resolution. Further developments of this new technique, including the adoption of more modern PET imaging algorithms, is a clear next step.

Appendix A

Preliminary LYSO System

An initial experiment was performed at the University of Edinburgh just prior to Professor Watts's relocation to York. In 2018 I took over the analysis and interpretation of this data during the first year of my PhD. The detectors employed had smaller arrays and lower angular and energy resolution than the PETsys system discussed in Chap 6. However, these initial results are presented here for comparison. The data set was abandoned a year into my PhD as we obtained the improved system and this archive data showed inconsistencies.

The Edinburgh system was comprised of two detectors, each made of 9 LYSO crystals in a 3 x 3 arrangement. The detectors were positioned 6 cm apart, approximately 10x less than usual distances in a PET scanner which are around 80-90 cm. Each LYSO crystal had dimensions of 4 mm x 4 mm x 22 mm and was coupled to a HAMAMTSU Silicon Photomultiplier. A ^{22}Na source of 55 kBq was placed equidistant between the two crystals, with a source to crystal separation of 3 cm. A diagram of the setup can be seen in Fig.A.1.

The data acquisition fed the output signals from the SiPMs to a CAEN Analogue to Digital converter (ADC) and via a delay cable to a time to digital converter (TDC). The ADC returned the integral of the pulse from the SiPMs, giving information proportional to the energy deposited in each crystal. The TDC returned the relative timing of the crystal hits with respect to the experimental trigger. The acquisition utilised a coincidence detection system triggered in logical 'AND' mode, such that an event would only be recorded if both the central crystals were triggered within a 10 ns coincidence window. The logic output signal from the module was used as the start time for the TDC modules, which are stopped by the delayed SiPM signals from each LYSO crystal.

The data set therefore comprised a series of events (satisfying the above trigger condition) in which the energy and timing of all crystal hits in the array were recorded. Existing preliminary calibrations to produce energies from the recorded signals in the LYSO were employed (but

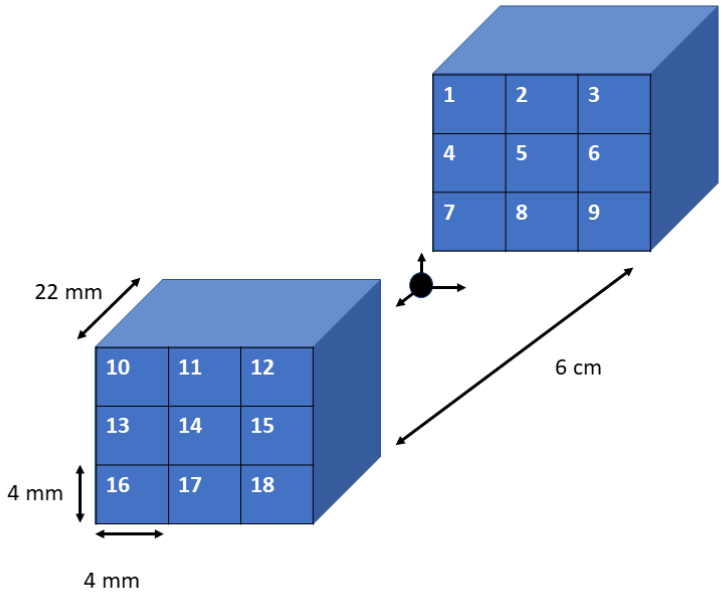

Figure A.1: A diagram of the mini-PET system. Two blocks of LYSO crystals separated by 6 cm. Each block contains 9 crystals.

subsequently checked in the analysis).

The analysis developed focused on the inter-crystal scatter in the detector arrays (i.e. > 1 crystal hit in both arrays). Key to the aims of the project are to extract the scatter angles of the photons in both detector arrays and to isolate the events of interest from any backgrounds.

The analysis procedure is outlined below:

1. Initial energy cuts were applied to all events. Events were only retained if the total energy deposited in each head was in the range 450-550 keV. It was also required that the central crystal of each array received an energy deposit greater than 60 keV.

2. It was assumed that all photons hit the central crystal first, and then Compton scattered into one of the outer crystals. Hence, the energy deposit in the central crystal should correspond to the electron recoil energy from the first Compton scattering process.

3. Assuming the energy in the central crystal arises from the Compton scattered electron. The angle, θ, at which the incoming photon must have scattered to deposit this energy can be calculated from Equation 1.1. This was done on an event-by-event basis.

4. The energy deposit in each of the surrounding crystals was assumed to arise from the scattered photon. These energies were then analysed using Eq. 1.1 to reconstruct the scattering angle which that photon undertook.

5. When the θ prediction from an outer crystal matched the θ prediction from the central crystal (within 15° error) the two were deemed to originate from the same Compton event.

The assumption that the central crystal was hit first may not always be the case in the data[1]. There will be some events in the yield where the photon hit an outer crystal first and then scattered inwards to the central detector. However as the experimental data and the simulation are analysed in the same way then a direct comparison (including miss-identifications from this assumption) can still be made.

A.1 LYSO array Geant4 Simulation

The experimental system described above was reconstructed in Geant4. The detectors were represented by pixelated blocks of LYSO separated by 6 cm. Stationary positrons were generated in the centre of the world volume, allowed to annihilate and then the trajectories of the resulting photons were tracked. All energy deposits detected in any given pixel were summed, this ensured that the position resolution of our simulation mimicked the geometry of the laboratory detector. The Geant4 energy deposits were also smeared with a Gaussian distribution ($\sigma = 21.33$ keV) in order to model the limited energy resolution of the detectors.

The simulation was designed to recreate only true events in the detector arrays. It did not incorporate random coincidences and backgrounds, but from analysis of our timing coincidence event rates in the data it is clear that such events give minimal contribution to the yield in the experimental data. Each simulation was initialised with a positron of zero energy dropped at the origin of the world. The positron quickly annihilates to produce two back-to-back photons. In nature these photons are perpendicularly polarised, quantum entangled, and emitted with an isotropic momentum vector. To examine the effects of these properties our simulation was run multiple times with various features omitted to explore the influence on the measured quantities. The simulation was run with the proper quantum entangled treatment, with the entanglement effects removed (equivalent to independent oppositely polarised photons), and with the polarisation of the PET photons randomised (unpolarised).

[1]Unfortunately the timing resolution of the detectors is too low to be able to correctly determine the interaction order, hence this assumption was made. We shall discuss the possible consequences of this in more detail later

To achieve these variations in simulation parameters three different physics process lists in Geant4 were used to vary the photon properties:

1. G4EmLivermorePhysics - photons obey the unpolarised Klein-Nishina scattering equation. These are referred to as unpolarised photons.

2. G4EmLivermorePolarizedPhysics - annihilation photons obey the polarised Klein-Nishina scattering equation. These are referred to as polarised photons.

3. Entangled G4EmLivermorePolarizedPhysics - our own modified version of this class creates perpendicularly polarised photons that, when subsequently Compton scatter, have relative phi scatter planes chosen according to the quantum entangled double scattering Klein-Nishina formula. These shall be referred to as quantum entangled photons.

A.2 LYSO Results

This section presents the results obtained by comparing the experimental data to the new QE-Geant4 simulation. Comparisons are made in bins of θ scatter angle reconstructed using the methodology described above and bins of $\Delta\phi$. In this first analysis only events in the central and 4 nearest crystals were analysed in each array. The corner crystal information was excluded, as the event rate was lower and the geometry leads to a different average phi resolution. This limits our angular resolution to bins centred on $\Delta\phi$ = 0, 90, 180 and 270°. This resolution is too poor to show the underlying $\cos(2\Delta\phi)$ distribution with any precision. However, we can measure how the asymmetry ratio, N(90°)/N(0°), varies with the θ scatter angles of the photons.

The laboratory data was separated into theta bins, of width 15°. Within each bin the ratio of events scattered at $\Delta\phi = 90°$ to those at 0° (the enhancement ratio) has been extracted from the data.

The resulting enhancement ratios are shown in blue in Fig. A.2 as a function of θ. Note that the θ value corresponds to both photons scattering in this θ range. The band represents the associated error, calculated using Poisson counting statistics.

To put this result into context we passed the simulated data (smeared with the energy resolution of the detectors) through the same analysis code. The results have been added to Fig.A.2, with the unpolarised simulation shown in purple, polarised in red and entangled in yellow.

The Geant4 predictions are particularly informative. Since the scattering distribution of unpolarised photons would be independent of ϕ then, neglecting geometrical effects, we would

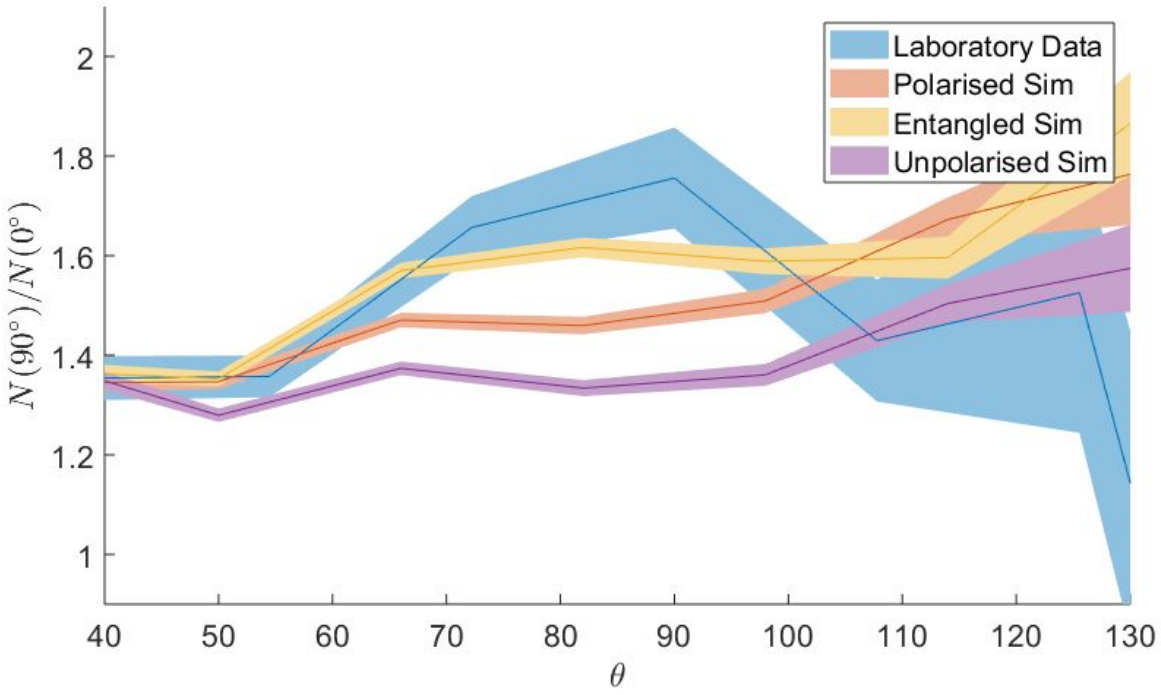

Figure A.2: Variation of enhancement with scattering angle θ. Laboratory data is shown in blue, unpolarised simulation in purple, polarised in red and entangled in yellow. The error bars were calculated from the number of events, assuming a Poisson distribution.

expect the enhancement for the unpolarsed simulation to be unity for all theta. Examining Fig.A.2 we can see that although the enhancement distribution is flat (independent of theta), there is a clear "false" asymmetry of around 1.3. The geometrical cause of this offset was identified and shall be discussed in more depth later.

The polarised prediction shows a slight enhancement, peaking to a value of 1.5 ($\sim$0.2 above the baseline from unpolarised), peaking around $\theta \approx 80°$. The entangled data follows the same trend but displays significantly larger enhancement, peaking to an enhancement ratio of 1.6 (0.3 above the baseline from unpolarised). Both of these results follow the distribution predicted by the unentangled and entangled Klein-Nishna formulas respectively. The entanglement is therefore predicted to increase the enhancement by around 50 percent, for the specific geometry and angular, energy resolution of the array. It should be noted that the full enhancement at $\theta \approx 82°$ will be diminished by the smearing effect of the large theta bins and relatively poor phi resolution achievable. However, there are clear differences evident in the predictions [2].

[2] At larger angles the errors in the statistical accuracy of the simulation become too large to draw conclusions. This is due to the rapidly decreasing cross section for scattering at these large theta ranges. Since event detection

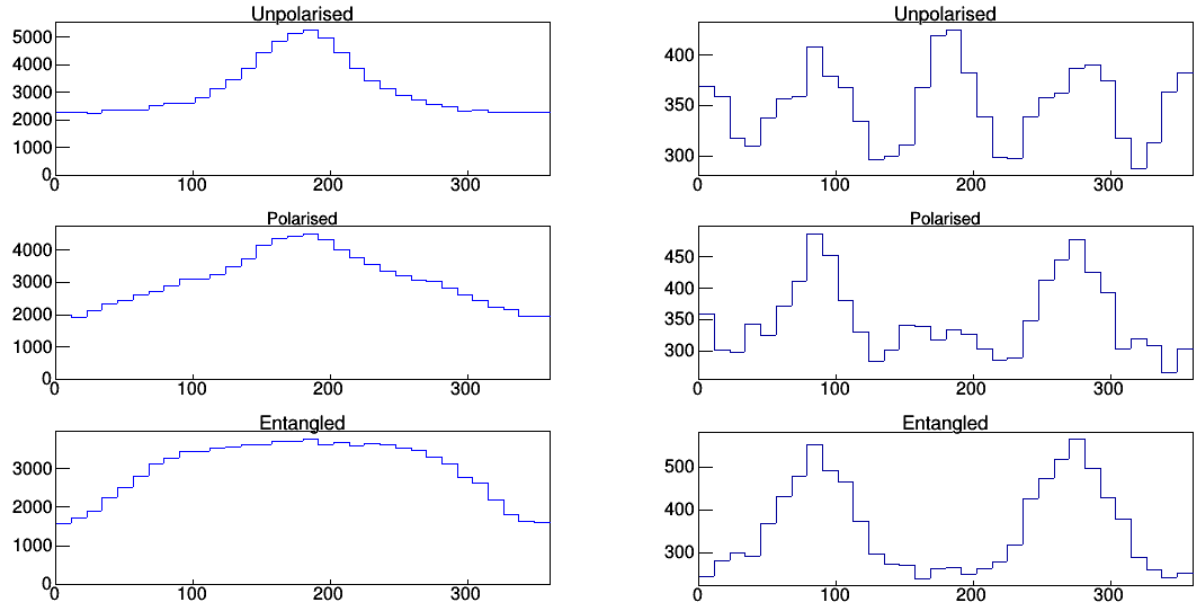

Figure A.3: Geant4 $\Delta\phi$ histograms for the theta range $75 - 90°$. Left: Analysing all events. Right: Only those events which hit the central crystal first.

The experimental lab data is also plotted in blue in Fig.A.2 for comparison with the Geant4 predictions. The data shows a maximum enhancement for the θ bin around 80-90°. It is clear that the non-entangled predictions lie well below the laboratory data for θ in the range 65-95 °. The data is far better reproduced by the entangled simulation.

A.2.1 Geometric Asymmetry and the cause of the false asymmetry

As discussed earlier, the fact that the unpolarised enhancement is not equal to 1 within error indicates that there are other effects at play. The delight of Geant4 is that we can not only extract the results the detector would register, but also the exact "Monte-Carlo truth" from the simulation. For instance, values for the exact theta and phi angles through which the photon scattered, and the coordinates of the interaction can be retrieved. This allows us to examine in depth any effects resulting from the detector geometry.

To investigate this asymmetry in unpolarised photons all events were split into theta ranges of 15°. For each range a histogram was plotted of the exact $\Delta\phi$ recorded by Geant4. Fig. A.3.(a) shows the delta phi distribution for each of the unpolarised, polarised and entangled simulations in the theta range 75-90°. This range was selected as it represents the region of

follows a Poisson distribution the error in the asymmetry given by the Poisson counting statistics is $1/\sqrt{N}$, where N is the number of events. Therefore the large error bars at high theta are representative of the low statistics

maximum enhancement.

For the polarised plot we expect a flat distribution independent of ϕ, instead there is a clear peak at 180°. This can only be a result of the detector geometry. The simplest explanation is that it corresponds to an edge effect resulting from the assumption that the central crystal was hit first. Should both photons interact at the edge of their respective detectors and scatter with the same ϕ then both photons will be lost. However should they scatter with $\Delta\phi = 180°$ 50% of the time both photons are lost and 50% both photons are detected. This theory was confirmed by analysing only those photons which hit the central crystal first (using exact position information extracted from Geant4). These events have been plotted in Fig.A.3 b), where it is clear to see that the dominating peak is removed. The remaining unpolarised distribution appears much more random, with slight peaks at 0, 90, 180 and 270°. This should be expected given the choice to exclude corner pixels, angles of 45, 135, 225 and 315° are much less likely to be detected. The same procedure was repeated for entangled and polarised photons. The underlying $\cos(2\phi)$ distribution is now revealed for both simulations, with a larger amplitude for the entangled data.

We now re-plot the asymmetry excluding all simulated events which did not hit the central crystal first Fig.A.4. This removes this geometric effect. Sure enough the polarised asymmetry is now 1 for all θ, consistent with our expectations. Some of the false asymmetry for polarised and entangled has also been removed, and the differences between them become more distinct.

Unfortunately applying this condition removes 89% of the recorded data. This emphasises the need for a larger detector or higher position resolution so that measurements are less sensitive to the detector geometry.

The maximum enhancement predicted for quantum entangled photons in 2.8. In these results the enhancement has been suppressed due to the blurring as a result of poor angular resolution.

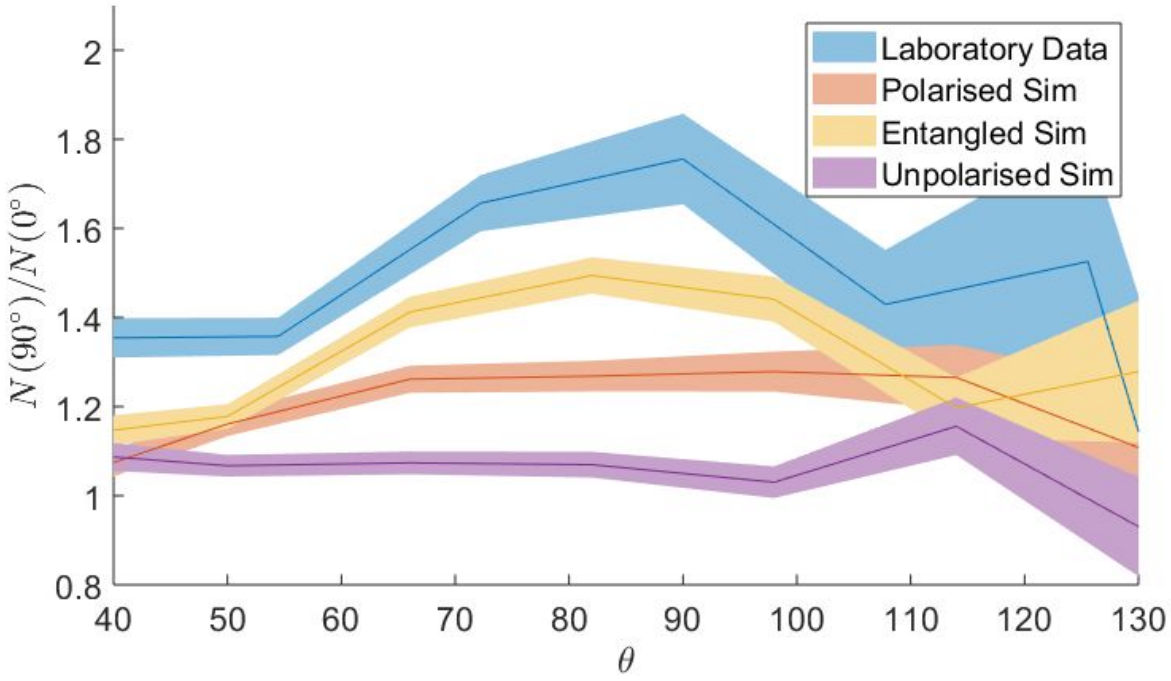

Figure A.4: Graph of asymmetry with theta. Only those simulated events which hit the central crystal first have been plotted. Entangled in yellow, polarised in red and unpolarised photons in purple. The experimental data is plotted in blue.

Bibliography

[Ach20] S. Acharya et al. "Unveiling the strong interaction among hadrons at the LHC". en. In: *Nature* 588.7837 (Dec. 2020). Bandiera_abtest: a Cc_license_type: cc_by Cg_type: Nature Research Journals Number: 7837 Primary_atype: Research Publisher: Nature Publishing Group Subject_term: Experimental nuclear physics;Experimental particle physics Subject_term_id: experimental-nuclear-physics;experimental-particle-physics, pp. 232–238.

[Ago03] S. Agostinelli et al. "Geant4—a simulation toolkit". en. In: *Nuclear Instruments and Methods in Physics Research Section A: Accelerators, Spectrometers, Detectors and Associated Equipment* 506.3 (July 2003), pp. 250–303.

[Aky21] T. Akyurek. "A new dead-time determination method for gamma-ray detectors using attenuation law". en. In: *Nuclear Engineering and Technology* 53.12 (Dec. 2021), pp. 4093–4097.

[All16] J. Allison et al. "Recent developments in Geant4". In: *Nuclear Instruments and Methods in Physics Research Section A: Accelerators, Spectrometers, Detectors and Associated Equipment* 835 (Nov. 2016), pp. 186–225.

[Alv18] H. Alva-Sánchez et al. "Understanding the intrinsic radioactivity energy spectrum from 176 Lu in LYSO/LSO scintillation crystals". en. In: *Scientific Reports* 8.1 (Nov. 2018). Number: 1 Publisher: Nature Publishing Group, p. 17310.

[And18] Pedro Andreo. "Monte Carlo simulations in radiotherapy dosimetry". In: *Radiation Oncology* 13.1 (June 2018), p. 121.

[Arc14] Pedro Arce et al. "Gamos: A framework to do Geant4 simulations in different physics fields with an user-friendly interface". en. In: *Nuclear Instruments and Methods in Physics Research Section A: Accelerators, Spectrometers, Detectors and Associated Equipment* 735 (Jan. 2014), pp. 304–313.

[BA57] D. Bohm and Y. Aharonov. "Discussion of Experimental Proof for the Paradox of Einstein, Rosen, and Podolsky". In: *Physical Review* 108.4 (Nov. 1957). Publisher: American Physical Society, pp. 1070–1076.

[BB48] E. Bleuler and H. L. Bradt. "Correlation between the States of Polarization of the Two Quanta of Annihilation Radiation". In: *Physical Review* 73.11 (June 1948). Publisher: American Physical Society, pp. 1398–1398.

[BDM77] M. Bruno, M. D'Agostino, and C. Maroni. "Measurement of linear polarization of positron annihilation photons". en. In: *Il Nuovo Cimento B (1971-1996)* 40.1 (July 1977), pp. 143–152.

[BDS81] G. Bertolini, E. Diana, and A. Scotti. "Correlation of annihilation gamma-ray polarization". en. In: *Il Nuovo Cimento B (1971-1996)* 63.2 (June 1981), pp. 651–665.

[Bey00] T. Beyer et al. "A combined PET/CT scanner for clinical oncology". eng. In: *Journal of Nuclear Medicine: Official Publication, Society of Nuclear Medicine* 41.8 (Aug. 2000), pp. 1369–1379.

[Bic92] Alden N. Bice. "Monte Carlo PET simulations: effect of photon polarization on scatter estimates". en. In: *Physics in Medicine and Biology* 37.5 (May 1992). Publisher: IOP Publishing, pp. 1185–1188.

[Bog03] S. E. Boggs. "Polarization constraints on gamma-ray event circles in compton scatter instruments". In: *Nuclear Instruments and Methods in Physics Research Section A: Accelerators, Spectrometers, Detectors and Associated Equipment* 503.3 (May 2003), pp. 562–566.

[Bra05] David Brasse et al. "Correction Methods for Random Coincidences in Fully 3D Whole-Body PET: Impact on Data and Image Quality". en. In: *Journal of Nuclear Medicine* 46.5 (May 2005). Publisher: Society of Nuclear Medicine Section: Basic Science Investigations, pp. 859–867.

[Bur02] C. Burger et al. "PET attenuation coefficients from CT images: experimental evaluation of the transformation of CT into PET 511-keV attenuation coefficients". eng. In: *European Journal of Nuclear Medicine and Molecular Imaging* 29.7 (July 2002), pp. 922–927.

[Car19] Peter Caradonna et al. "Probing entanglement in Compton interactions". en. In: *Journal of Physics Communications* 3.10 (Oct. 2019). Publisher: IOP Publishing, p. 105005.

[Che17] Simon R. Cherry et al. "Total-body imaging: Transforming the role of positron emission tomography". In: *Science Translational Medicine* 9.381 (2017). Publisher: American Association for the Advancement of Science _eprint: https://stm.sciencemag.org/cont

[CS78] J. F. Clauser and A. Shimony. "Bell's theorem: experimental tests and implications". en. In: *Reports on Progress in Physics* 41.12 (1978), pp. 1881–1927.

[CSP12] Simon Cherry, James Sorenson, and Michael Phelps. *Physics in Nuclear Medicine*. 4th. Saunders, Apr. 2012.

[Due19] M. Duer et al. "Measurement of nuclear transparency ratios for protons and neutrons". en. In: *Physics Letters B* 797 (Oct. 2019), p. 134792.

[Ehm17] Eric C. Ehman et al. "PET/MRI: Where Might It Replace PET/CT?" In: *Journal of magnetic resonance imaging : JMRI* 46.5 (Nov. 2017), pp. 1247–1262.

[EPR35] A. Einstein, B. Podolsky, and N. Rosen. "Can Quantum-Mechanical Description of Physical Reality Be Considered Complete?" In: *Physical Review* 47.10 (May 1935). Publisher: American Physical Society, pp. 777–780.

[Fah02] Frederic H. Fahey. "Data Acquisition in PET Imaging". en. In: *Journal of Nuclear Medicine Technology* 30.2 (June 2002), pp. 39–49.

[FK06] James W Fletcher and Joel S Karp. "PET COE Board Meets with Industry Advisory Group to Map Out Goals". en. In: (2006), p. 10.

[Gar53] R. L. Garwin. "Thermalization of Positrons in Metals". In: *Physical Review* 91.6 (Sept. 1953). Publisher: American Physical Society, pp. 1571–1572.

[Gat87] Emilio Gatti et al. "Dynamics of electrons in drift detectors". en. In: *Nuclear Instruments and Methods in Physics Research Section A: Accelerators, Spectrometers, Detectors and Associated Equipment* 253.3 (Jan. 1987), pp. 393–399.

[GBL04] John Gillam, T.E. Beveridge, and R.A. Lewis. "Positron emission imaging using acquired cone-surfaces from opposing compton cameras". In: vol. 5. Nov. 2004, pp. 2810–2814. ISBN: 978-0-7803-8700-3.

[GH20] Stefan Gundacker and Arjan Heering. "The silicon photomultiplier: fundamentals and applications of a modern solid-state photon detector". en. In: *Physics in Medicine & Biology* 65.17 (Aug. 2020). Publisher: IOP Publishing, 17TR01.

[Gu11] Y. Gu et al. "Study of a high-resolution, 3D positioning cadmium zinc telluride detector for PET". eng. In: *Physics in Medicine and Biology* 56.6 (Mar. 2011), pp. 1563–1584.

[Han48] R. C. Hanna. "Polarization of Annihilation Radiation". en. In: *Nature* 162.4113 (Aug. 1948). Bandiera_abtest: a Cg_type: Nature Research Journals Number: 4113 Primary_atype: Research Publisher: Nature Publishing Group, pp. 332–332.

[Har04] Michael D. Harpen. "Positronium: Review of symmetry, conserved quantities and decay for the radiological physicist". en. In: *Medical Physics* 31.1 (2004). _eprint: https://aapm.onlinelibrary.wiley.com/doi/pdf/10.1118/1.1630494, pp. 57–61.

[Hei54] Walter Heitler. *The quantum theory of radiation*. Vol. 86. Courier Corporation, 1954.

[HM19] Beatrix C. Hiesmayr and Pawel Moskal. "Witnessing Entanglement In Compton Scattering Processes Via Mutually Unbiased Bases". en. In: *Scientific Reports* 9.1 (June 2019). Bandiera_abtest: a Cc_license_type: cc_by Cg_type: Nature Research Journals Number: 1 Primary_atype: Research Publisher: Nature Publishing Group Subject_term: Quantum information;Single photons and quantum effects Subject_term_id: quantum-information;single-photons-and-quantum-effects, p. 8166.

[Hos17] Shota Hosokawa et al. "A simulation study for estimating scatter fraction in whole-body 18F-FDG PET/CT". eng. In: *Radiological Physics and Technology* 10.2 (June 2017), pp. 204–212.

[Hua18] Ya-Yao Huang. *An Overview of PET Radiopharmaceuticals in Clinical Use: Regulatory, Quality and Pharmacopeia Monographs of the United States and Europe*. en. Publication Title: Nuclear Medicine Physics. IntechOpen, Nov. 2018.

[Ini14] K Iniewski. "CZT detector technology for medical imaging". In: *Journal of Instrumentation* 9 (Nov. 2014), p. C11001.

[Jan11] S. Jan et al. "GATE V6: a major enhancement of the GATE simulation platform enabling modelling of CT and radiotherapy". eng. In: *Physics in Medicine and Biology* 56.4 (Feb. 2011), pp. 881–901.

[Jas17] B. Jasińska et al. "Human Tissues Investigation Using PALS Technique". In: *Acta Physica Polonica B* 48.10 (2017). arXiv: 1711.04512, p. 1737.

[JCD19] Wei Jiang, Yamn Chalich, and M. Jamal Deen. "Sensors for Positron Emission Tomography Applications". In: *Sensors (Basel, Switzerland)* 19.22 (Nov. 2019), p. 5019.

[Jo16] Woojin Jo et al. "Preliminary Research of CZT Based PET System Development in KAERI". In: *Journal of Radiation Protection and Research* 41 (June 2016), pp. 81–86.

[JT17] Terry Jones and David W. Townsend. "History and future technical innovation in positron emission tomography". In: *Journal of Medical Imaging* 4.1 (Mar. 2017). Publisher: SPIE, p. 011013.

[Kap14] Łukasz Kapłon et al. "Plastic scintillators for positron emission tomography obtained by the bulk polymerization method". In: *Bio-Algorithms and Med-Systems* 10 (Jan. 2014).

[KDC04] PAUL E. Kinahan, MICHEL Defrise, and ROLF Clackdoyle. "CHAPTER 20 - Analytic Image Reconstruction Methods". en. In: *Emission Tomography*. Ed. by Miles N. Wernick and John N. Aarsvold. San Diego: Academic Press, Jan. 2004, pp. 421–442.

[KHC90] M. Kakimoto, T. Hyodo, and T. B. Chang. "Conversion of ortho-positronium in low-density oxygen gas". en. In: *Journal of Physics B: Atomic, Molecular and Optical Physics* 23.3 (Feb. 1990). Publisher: IOP Publishing, pp. 589–597.

[Kim11] Jae Cheon Kim et al. "Charge sharing in common-grid pixelated CdZnTe detectors". en. In: *Nuclear Instruments and Methods in Physics Research Section A: Accelerators, Spectrometers, Detectors and Associated Equipment* 654.1 (Oct. 2011), pp. 233–243.

[KN29] O. Klein and Y. Nishina. "Über die Streuung von Strahlung durch freie Elektronen nach der neuen relativistischen Quantendynamik von Dirac". de. In: *Zeitschrift für Physik* 52.11 (Nov. 1929), pp. 853–868.

[Kno10] Glenn F. Knoll. *Radiation detection and measurement*. en. 2010.

[KS05] Krzysztof Kacperski and Nicholas M. Spyrou. "Performance of three-photon PET imaging: Monte Carlo simulations". eng. In: *Physics in Medicine and Biology* 50.23 (Dec. 2005), pp. 5679–5695.

[Kun05] C. Kuntner et al. "Advances in the scintillation performance of LuYAP:Ce single crystals". In: *Nuclear Instruments and Methods in Physics Research A* 537.1-2 (2005), pp. 295–301.

[Kun11] Z. Kuncic et al. "Polarization enhanced X-ray imaging for biomedicine". en. In: *Nuclear Instruments and Methods in Physics Research Section A: Accelerators, Spectrometers, Detectors and Associated Equipment*. NIMA_4th International Conference on Imaging techniques in Subatomic Physics, Astrophysics, Medicine, Biology and Industry 648 (Aug. 2011), S208–S210.

[Lam01] Adriaan A. Lammertsma. "PET/SPECT: functional imaging beyond flow". en. In: *Vision Research* 41.10 (May 2001), pp. 1277–1281.

[LDH97] F. Lei, A. J. Dean, and G. L. Hills. "Compton Polarimetry in Gamma-Ray Astronomy". en. In: *Space Science Reviews* 82.3 (Nov. 1997), pp. 309–388.

[Le 11] Ludovic Le Meunier et al. "Motion frozen 18F-FDG cardiac PET". en. In: *Journal of Nuclear Cardiology* 18.2 (Apr. 2011), pp. 259–266.

[Leo94] William R. Leo. *Techniques for Nuclear and Particle Physics Experiments: A How-to Approach*. en. 2nd ed. Berlin Heidelberg: Springer-Verlag, 1994.

[Lev08] C. S. Levin. "New Imaging Technologies to Enhance the Molecular Sensitivity of Positron Emission Tomography". In: *Proceedings of the IEEE* 96.3 (Mar. 2008), pp. 439–467.

[Lew08] Tom K Lewellen. "Recent developments in PET detector technology". In: *Phys Med Biol* 53.17 (Aug. 2008).

[LM03] R.M. Lewitt and S. Matej. "Overview of methods for image reconstruction from projections in emission computed tomography". In: *Proceedings of the IEEE* 91.10 (Oct. 2003). Conference Name: Proceedings of the IEEE, pp. 1588–1611.

[Lod06] Martin A. Lodge et al. "Comparison of 2-dimensional and 3-dimensional acquisition for 18F-FDG PET oncology studies performed on an LSO-based scanner". eng. In: *Journal of Nuclear Medicine: Official Publication, Society of Nuclear Medicine* 47.1 (Jan. 2006), pp. 23–31.

[Mak20] Mihael Makek et al. "Single-layer Compton detectors for measurement of polarization correlations of annihilation quanta". en. In: *Nuclear Instruments and Methods in Physics Research Section A: Accelerators, Spectrometers, Detectors and Associated Equipment*. Proceedings of the Vienna Conference on Instrumentation 2019 958 (Apr. 2020), p. 162835.

[McA17] L. H. McAreavey et al. "Characterisation of a CZT detector for dosimetry of molecular radiotherapy". en. In: *Journal of Instrumentation* 12.03 (Mar. 2017). Publisher: IOP Publishing, P03001–P03001.

[McN14] A. L. McNamara et al. "Towards optimal imaging with PET: an in silico feasibility study". eng. In: *Physics in Medicine and Biology* 59.24 (Dec. 2014), pp. 7587–7600.

[Mel] Charles L. Melcher. "Scintillation Crystals for PET". In: *J Nucl Med.* (), pp. 1051–1055.

[Mos18] P. Moskal et al. "Feasibility studies of the polarization of photons beyond the optical wavelength regime with the J-PET detector". eng. In: *The European Physical Journal. C, Particles and Fields* 78.11 (2018), p. 970.

[Mos19] P. Moskal et al. "Feasibility study of the positronium imaging with the J-PET tomograph". en. In: *Physics in Medicine & Biology* 64.5 (Mar. 2019). Publisher: IOP Publishing, p. 055017.

[Mye56] R. Thomas Myers. "Dead time of a Geiger-Mueller tube by the double-source method". en. In: *Journal of Chemical Education* 33.8 (Aug. 1956), p. 395.

[NEM08] National Electrical Manufacturers Association (NEMA). *NEMA NU4-2008: performance measurements of small animal positron emission tomographs*. 2008.

[Pap12] Panagiotis Papadimitroulas et al. "A dose point kernel database using GATE Monte Carlo simulation toolkit for nuclear medicine applications: comparison with other Monte Carlo codes". eng. In: *Medical Physics* 39.8 (Aug. 2012), pp. 5238–5247.

[PW47] M. H. L. Pryce and J. C. Ward. "Angular Correlation Effects with Annihilation Radiation". en. In: *Nature* 160.4065 (Sept. 1947). Number: 4065 Publisher: Nature Publishing Group, pp. 435–435.

[Rea19] Sara Reardon. "Whole-body PET scanner produces 3D images in seconds". EN. In: *Nature* 570 (June 2019), p. 285.

[Ren06] D. Renker. "Geiger-mode avalanche photodiodes, history, properties and problems". en. In: *Nuclear Instruments and Methods in Physics Research Section A: Accelerators, Spectrometers, Detectors and Associated Equipment*. Proceedings of the 4th International Conference on New Developments in Photodetection 567.1 (Nov. 2006), pp. 48–56.

[Rie20] Benjamin Rienäcker et al. "Absolute fraction of emitted Ps determined by GEANT4 supported analysis of gamma spectra". In: *Physical Review A* 102.6 (Dec. 2020). arXiv: 2010.01854, p. 062212.

[Ruc18] Antoni Rucinski et al. "Plastic scintillator based PET detector technique for proton therapy range monitoring: A Monte Carlo study". In: *2018 IEEE Nuclear Science Symposium and Medical Imaging Conference Proceedings (NSS/MIC)*. ISSN: 2577-0829. Nov. 2018, pp. 1–4.

[RZ07] Andrew J. Reader and Habib Zaidi. "Advances in PET Image Reconstruction". en. In: *PET Clinics*. PET Instrumentation and Quantification 2.2 (Apr. 2007), pp. 173–190.

[Sah10] Gopal B. Saha. *Basics of PET Imaging: Physics, Chemistry, and Regulations*. en. 2nd ed. New York: Springer-Verlag, 2010.

[SPH48] Hartland S. Snyder, Simon Pasternack, and J. Hornbostel. "Angular Correlation of Scattered Annihilation Radiation". In: *Physical Review* 73.5 (Mar. 1948), pp. 440–448.

[SRE12] Caroline A. Schneider, Wayne S. Rasband, and Kevin W. Eliceiri. "NIH Image to ImageJ: 25 years of image analysis". en. In: *Nature Methods* 9.7 (July 2012). Bandiera_abtest: a Cg_type: Nature Research Journals Number: 7 Primary_atype: Comments & Opinion Publisher: Nature Publishing Group Subject_term: Imaging;Software Subject_term_id: imaging;software, pp. 671–675.

[Sur06] Suleman Surti et al. "Imaging performance of an LYSO-based TOF PET scanner". en. In: *Journal of Nuclear Medicine* 47.suppl 1 (May 2006). Publisher: Society of Nuclear Medicine Section: Oral Presentations - Physicians/Scientists/Pharmacists, 54P–54P.

[TAK10] Shan Tong, Adam M Alessio, and Paul E Kinahan. "Image reconstruction for PET/CT scanners: past achievements and future challenges". In: *Imaging in medicine* 2.5 (Oct. 2010), pp. 529–545.

[Tak10] Shin'ichiro Takeda et al. "Polarimetric performance of Si/CdTe semiconductor Compton camera". en. In: *Nuclear Instruments and Methods in Physics Research Section A: Accelerators, Spectrometers, Detectors and Associated Equipment* 622.3 (Oct. 2010), pp. 619–627.

[Tog16] M. Toghyani et al. "Polarisation-based coincidence event discrimination: an in silico study towards a feasible scheme for Compton-PET". eng. In: *Physics in Medicine and Biology* 61.15 (Aug. 2016), pp. 5803–5817.

[Tow08] David W. Townsend. "Combined PET/CT: the historical perspective". In: *Seminars in ultrasound, CT, and MR* 29.4 (Aug. 2008), pp. 232–235.

[TZG03] Gabriele Tarantola, Felicia Zito, and Paolo Gerundini. "PET instrumentation and reconstruction algorithms in whole-body applications". eng. In: *Journal of Nuclear Medicine: Official Publication, Society of Nuclear Medicine* 44.5 (May 2003), pp. 756–769.

[UW49] University of Oxford and J. C. Ward. "Some properties of the elementary particles". eng. PhD thesis. Thesis DPhil–University of Oxford, 1949.

[Van16] S. Vandenberghe et al. "Recent developments in time-of-flight PET". In: *EJNMMI Physics* 3 (Feb. 2016).

[VK15] Juan José Vaquero and Paul Kinahan. "Positron Emission Tomography: Current Challenges and Opportunities for Technological Advances in Clinical and Preclinical Imaging Systems". eng. In: *Annual Review of Biomedical Engineering* 17 (2015), pp. 385–414.

[VMK20] Stefaan Vandenberghe, Pawel Moskal, and Joel S. Karp. "State of the art in total body PET". In: *EJNMMI Physics* 7 (May 2020), p. 35.

[Wag14] A. A. Wagadarikar et al. "Sensitivity Improvement of Time-of-Flight (ToF) PET Detector Through Recovery of Compton Scattered Annihilation Photons". In: *IEEE Transactions on Nuclear Science* 61.1 (Feb. 2014), pp. 121–125.

[Wat21] D. P. Watts et al. "Photon quantum entanglement in the MeV regime and its application in PET imaging". en. In: *Nature Communications* 12.1 (May 2021), p. 2646.

[WCP12] C. Wanarak, W. Chewpraditkul, and A. Phunpueok. "Light yield non-proportionality and energy resolution of Lu1.95Y0.05SiO5:Ce and Lu2SiO5:Ce scintillation crystals". en. In: *Procedia Engineering*. ISEEC 32 (Jan. 2012), pp. 765–771.

[Web02] Marvin J Weber. "Inorganic scintillators: today and tomorrow". en. In: *Journal of Luminescence* 100.1 (Dec. 2002), pp. 35–45.

[WLB76] A. R. Wilson, J. Lowe, and D. K. Butt. "Measurement of the relative planes of polarization of annihilation quanta as a function of separation distance". en. In: *Journal of Physics G: Nuclear Physics* 2.9 (Sept. 1976). Publisher: IOP Publishing, pp. 613–624.

[WNC96] C. C. Watson, D. Newport, and M. E. Casey. "A Single Scatter Simulation Technique for Scatter Correction in 3D PET". en. In: *Three-Dimensional Image Reconstruction in Radiology and Nuclear Medicine*. Ed. by Pierre Grangeat and Jean-Louis Amans. Computational Imaging and Vision. Dordrecht: Springer Netherlands, 1996, pp. 255–268.

[WS50] C. S. Wu and I. Shaknov. "The Angular Correlation of Scattered Annihilation Radiation". In: *Physical Review* 77.1 (Jan. 1950). Publisher: American Physical Society, pp. 136–136.

[Yos20] Eiji Yoshida et al. "Whole gamma imaging: a new concept of PET combined with Compton imaging". en. In: *Physics in Medicine & Biology* 65.12 (June 2020). Publisher: IOP Publishing, p. 125013.

[ZE07] H. Zaidi and William D. Erwin. "Quantitative Analysis in Nuclear Medicine Imaging". en. In: *Journal of Nuclear Medicine* 48.8 (Aug. 2007), pp. 1401–1401.